LLNL-SR-2001721

Lawrence Livermore National Laboratory

Final report from the ACT Project "Determining Exact RANS Operators with the Macroscopic Forcing Method"

D. Lavacot, J. Liu, B. Morgan, A. Mani

December 2024

Final report from the ACT Project
"Determining Exact RANS Operators with the Macroscopic Forcing Method"

Dana L. O.-L. Lavacot[a], Jessie Liu[a], Brandon E. Morgan[b], Ali Mani[a]

[a] *Department of Mechanical Engineering, Stanford University, Stanford, CA 94305, USA*

[b] *Lawrence Livermore National Laboratory, Livermore, CA 94550, USA*

Abstract

This report contains a compilation of key results and findings from the ACT project "Determining Exact RANS Operators with the Macroscopic Forcing Method." The Macroscopic Forcing Method (MFM), a numerical tool for determining closure operators, is used to measure eddy diffusivity moments in Rayleigh-Taylor (RT) instability. It is first applied to low-Atwood 2D RT instability; that work is then extended to 3D RT at different finite Atwood numbers. It is found that nonlocality is important for modeling the mean scalar transport closure operator in RT mixing. Additionally, work is done to improve the statistical convergence of MFM for chaotic problems like RT mixing.

Nonlocality of Mean Scalar Transport in Two-Dimensional Rayleigh-Taylor Instability Using the Macroscopic Forcing Method

D. L. O.-L. Lavacot[1, 2] †, J. Liu[1], H. Williams[1, 2], B. E. Morgan[2], and A. Mani[1]

[1]Department of Mechanical Engineering, Stanford University, Stanford, CA

[2]Lawrence Livermore National Laboratory, Livermore, CA

(Received xx; revised xx; accepted xx)

The importance of nonlocality of mean scalar transport in 2D Rayleigh-Taylor Instability (RTI) is investigated. The Macroscopic Forcing Method (MFM) is utilized to measure spatio-temporal moments of the eddy diffusivity kernel representing passive scalar transport in the ensemble averaged fields. Presented in this work are several studies assessing the importance of the higher-order moments of the eddy diffusivity, which contain information about nonlocality, in models for RTI. First, it is demonstrated through a comparison of leading-order models that a purely local eddy diffusivity is insufficient in capturing the mean field evolution of the mass fraction in RTI. Therefore, higher-order moments of the eddy diffusivity operator are not negligible. Models are then constructed by utilizing the measured higher-order moments. It is demonstrated that an explicit operator based on the Kramers-Moyal expansion of the eddy diffusivity kernel is insufficient. An implicit operator construction that matches the measured moments is shown to offer improvements relative to the local model in a converging fashion.

Key words: Authors should not enter keywords on the manuscript, as these must be chosen by the author during the online submission process and will then be added during the typesetting process (see http://journals.cambridge.org/data/relatedlink/jfm-keywords.pdf for the full list)

1. Introduction

Rayleigh-Taylor Instability (RTI) is a phenomenon that occurs when a heavy fluid is accelerated into a light fluid. Specifically, RTI occurs when the following are present: 1) a density gradient, 2) an acceleration (associated with the body force) in the direction opposite that of the density gradient, and 3) a perturbation at the interface of the two fluids. RTI is present in many scientific and engineering applications such as supernovae (Gull 1975) and inertial confinement fusion (ICF) (Zhou 2017; Lindl 1995). In the case of ICF, RTI occurs when a perturbation forms between the outer heavy ablator and the inner light deuterium gas, which causes premature mixing in the target, thereby greatly reducing the efficiency of the process. Thus, RTI is of great interest to scientists and engineers, especially in the context of ICF.

During a typical ICF experiment design process, a Reynolds-Averaged Navier-Stokes (RANS) approach is often utilized to model the role of hydrodynamic instabilities such as RTI. This is despite the fact that RTI can be more accurately predicted using high-fidelity methods like direct numerical simulations (DNS) (Youngs 1994; Cook & Dimotakis 2001; Cook & Zhou 2002; Cabot & Cook 2006; Mueschke & Schilling 2009) and large eddy simulations (LES)

† Email address for correspondence: dlol@stanford.edu

(Darlington *et al.* 2002; Cook *et al.* 2004; Cabot 2006). Motivation for development of RANS models for various engineering applications like ICF can be understood by considering the computational cost of each method. DNS requires resolution of the smallest turbulent scales, and LES the energy-containing scales, which are still much smaller than the macroscopic physics (i.e., averaged fields) of engineering interest. On the other hand, by design, RANS must only resolve macroscopic scales, thereby requiring much lower computational cost. Thus, RANS models are commonly used in engineering practice, especially in design optimization, where hundreds of thousands of simulations are often performed. Such is especially the case in designing targets for ICF experiments (Casey *et al.* 2014; Khan *et al.* 2016). Due to the utility of RANS in such applications, the need for predictive RANS models remains salient.

Models of varying complexities have been applied to the RTI problem. Among the most commonly-used types are two-equation models. One such model is the ubiquitously-used k-ε model (Launder & Spalding 1974). Particularly, Gauthier & Bonnet (1990) introduced algebraic relations for some closures to satisfy realizability constraints for the model to be valid under the strong gradients of RTI. Another popular two-equation model is the k-L model; a version was introduced by Dimonte & Tipton (2006) for RTI. One appeal of the k-L model is its inclusion of a transport equation for turbulence lengthscale L (in place of the transport equation for ε in k-ε) that can be related to the initial interface perturbation. The self-similarity of turbulent RTI is leveraged to set the model coefficients.

These two-equation models rely on the gradient diffusion approximation for the turbulent mass flux closure. The gradient diffusion approximation rests on the assumption that turbulence transports quantities in a manner similar to Fickian diffusion. Importantly, this approximation implies purely local dependence of the mean turbulent flux on the mean gradient, ignoring history effects and gradients at nearby points in space. However, this approximation may not be valid for mean scalar transport. Specifically, the turbulent mass flux contains features that the gradient diffusion approximation cannot capture (Morgan & Greenough 2015; Denissen *et al.* 2014), so a local coefficient may not be enough to scale the mean gradient to model turbulent mass flux.

Nonlocality in RTI has been studied in experiments and simulations. Clark *et al.* (1997) analyzed data from turbulent RTI experiments and compared the pressure-strain correlation and pressure production due to turbulent mass flux, suggesting spatial nonlocality of pressure effects. DNS studies by Ristorcelli & Clark (2004) and experiments by Mueschke *et al.* (2006) have also examined nonlocality of RTI in the context of two-point correlations. Thus, the nonlocal nature of RTI is well-known, and work has been done to capture this nonlocality in models. For example, two-point closures to account for nonlocality in RTI have been developed by several authors for RANS (Clark & Spitz 1995; Steinkamp *et al.* 1999*b*,*a*; Pal *et al.* 2018; Kurien & Pal 2022) and LES (Parish & Duraisamy 2017). While these works attempt to address the effects of nonlocality in RTI, they do so without directly studying the form of the nonlocal operator.

Several authors have studied ways to directly measure the nonlocal eddy diffusivity in other canonical flows. One such approach involves application of the Green's function. The Green's function approach starts from analytical derivations of relations between turbulent fluxes and mean gradients, which was done by Kraichnan (1987). Hamba (1995) then introduced a reformulation of these relations appropriate for numerical computation of nonlocal eddy diffusivities, which has been applied to study channel flow (Hamba 2004) and, most recently, homogeneous isotropic turbulence (HIT) (Hamba 2022).

A different approach to determining nonlocal eddy diffusivities is the Macroscopic Forcing Method (MFM) by Mani & Park (2021). In contrast to the Green's function approach, MFM is derived by considering arbitrary forcing added directly to the transport equations with its formulation rooted in linear algebra. Additionally, MFM offers extensions to the Green's function approach by utilization of forcing functions that are not of the form of a Dirac delta.

Harmonic forcing has been utilized to derive analytical fits to nonlocal operators in Fourier space (Shirian & Mani 2022). Additionally, forcing polynomial mean fields using inverse MFM offers a computationally economical path for determination of spatio-temporal moments of the eddy diffusivity operator in conjunction with the Kramers-Moyal expansion as opposed to computation of the moments from a full MFM analysis through post-processing (Mani & Park 2021). Previous works using MFM have revealed turbulence operators for a variety of flows. Shirian & Mani (2022) and Shirian (2022) measured nonlocal operators in space and time in HIT. Though the spatial nonlocal operator was measured in HIT, it was applied to a turbulent round jet and was shown to match experiments more closely than the purely local Prandtl mixing-length model. MFM has also been applied to turbulent wall-bounded flows, including channel flow (Park & Mani 2023*b*) and separated boundary layers (Park *et al.* 2022; Park & Mani 2023*a*), to measure the anisotropic but local eddy diffusivity. In those flows, incorporation of the MFM-measured anisotropic eddy diffusivity improved RANS model predictions significantly, and remaining model errors were attributed to missing nonlocal effects.

It is with a motivation towards RANS model improvement that the present work seeks to understand nonlocality of closure operators governing turbulent scalar flux transport in RTI using MFM. Note that it is not intended for MFM to supplant current RANS models. Instead, MFM is an analysis tool that can be used to assess models and discover the necessary characteristics for accurate models. Here, MFM allows for direct measurement of nonlocal closure operators, which has not yet been done in RTI. This new knowledge of nonlocality of the mean scalar transport closure operator in RTI will aid in the development of improved RANS models used for studying ICF.

It is important to note that this work presents MFM measurements for a simplified RTI problem: the flow is two-dimensional, incompressible, and low-Atwood number, and only passive scalar mixing is considered. Since the eddy diffusivity is not universal, the MFM measurements of its moments presented here cannot be directly extended to more complex RTI. However, valuable insight into trends in the eddy diffusivity for mean scalar transport in RTI can be gained in this work. This follows the common process for developing turbulence models, where models are first designed for simpler flows then tested on and adjusted for more complex flows. In this work, MFM is performed on a simplified RTI problem to give a preliminary look into the eddy diffusivity of Rayleigh-Taylor-type flows, but future work will involve extensions to more complex flow characteristics that are closer to the practical flow observed in ICF capsules. The intent of this work is to present MFM as a tool for determining characteristics of the eddy diffusivity of a flow (i.e., its nonlocality and the importance of its higher order moments) that a model should satisfy in order to accurately predict mean scalar transport. The current work will inform future studies with additional complexities, including three-dimensionality, finite Atwood number, compressibility, and coupling with momentum.

This work is organized as follows. First, an overview of RTI is covered briefly in §2. Next, §3 gives an overview of the mathematical methods used in this work, including: 1) the generalized eddy diffusivity and its approximation via a Karmers-Moyal expansion; 2) MFM and its application for finding the eddy diffusivity moments; 3) self-similarity analysis. Simulation details, including the governing equations and the computational approach, are given in §4. Finally, results of several studies on the importance of higher-order eddy diffusivity moments as well as assessments of suggested operator forms incorporating nonlocality of the eddy diffusivity for mean scalar transport in RTI are presented in §5. The results show that nonlocality of the eddy diffusivity is important in mean scalar transport of the RTI problem studied here, and RANS models incorporating this nonlocality result in more accurate predictions than leading-order models.

2. Brief overview of RTI

RTI is characterized by spikes (heavy fluid moving into light fluid) and bubbles (light fluid into heavy fluid). The mixing widths of these spikes and bubbles are denoted as h_s and h_b, respectively, and the mixing half-width is defined as $h = \frac{1}{2}(h_s + h_b)$. The behaviors of these quantities in RTI are dependent on the Atwood number, defined as

$$A = \frac{\rho_H - \rho_L}{\rho_H + \rho_L}. \tag{2.1}$$

Here, ρ_H and ρ_L are the densities of the heavy and light fluids, respectively. In the limit of low-Atwood number and late time, the mixing layer width is expected to reach a self-similar state of growth that scales quadratically with time:

$$h \approx \alpha A g t^2, \tag{2.2}$$

where α is the mixing width growth rate. The mixing width growth rate can also be viewed as the net mass flux through the midplane (Cook *et al.* 2004). In this case, α can also be written as

$$\alpha = \frac{\dot{h}^2}{4Agh}, \tag{2.3}$$

where $\dot{h}$ is the time derivative of h. In the limit of self-similarity, these two definitions of α are expected to converge to the same value.

In a simulation, h can be measured as

$$h \equiv 4 \int \langle Y_H \, (1 - Y_H) \rangle dy, \tag{2.4}$$

where Y_H is the mass fraction of the heavy fluid (therefore, $Y_L = 1 - Y_H$ is the mass fraction of the light fluid), and $\langle * \rangle$ denotes averaging over realizations and homogeneous direction x. An alternative definition used in works such as Cabot & Cook (2006) and Morgan *et al.* (2017) is

$$h_{\text{hom}} \equiv 4 \int \langle Y_H \rangle \, (1 - \langle Y_H \rangle) \, dy. \tag{2.5}$$

This definition is particularly useful, since it allows h to be determined solely based on the RANS field. That is, there is no closure problem in determining h with this definition. Thus, this is the h reported in this work.

From these two definitions, a mixedness parameter ϕ can be defined, which can be interpreted as the ratio of mixed to entrained fluid (Youngs 1994; Morgan *et al.* 2017):

$$\phi \equiv \frac{h}{h_{\text{hom}}} = 1 - 4\frac{\int \langle Y_H' Y_H' \rangle dy}{h_{\text{hom}}}. \tag{2.6}$$

In the limit of self-similarity, ϕ is expected to approach a steady-state value.

A metric for turbulent transition is the Taylor Reynolds number:

$$Re_T = \frac{k^{1/2} \lambda}{\nu}, \tag{2.7}$$

where $k = \frac{1}{2}\langle u_i' u_i' \rangle$ is the turbulence kinetic energy, and λ is the effective Taylor microscale, approximated by

$$\lambda = \sqrt{\frac{10 \nu L}{k^{1/2}}}. \tag{2.8}$$

Here, the turbulent lengthscale L can be approximated as $\frac{1}{5}$ the mixing layer width (Morgan *et al.*

2017). The large-scale Reynolds number can also be examined (Cabot & Cook 2006):

$$Re_L = \frac{h_{99}\dot{h}_{99}}{\nu}, \tag{2.9}$$

where h_{99} is the mixing width based on 1%-99% mass fraction. Dimotakis (2000) determined that the criterion for turbulent transition is when $Re_T > 100$ or $Re_L > 10,000$.

3. Mathematical methods

3.1. *Model problem*

In this work, a two-dimensional (2D), nonreacting flow with two species—a heavy fluid over a light fluid—is considered, with gravity pointing in the negative y-direction. It must be noted that the behavior of 2D RTI is significantly different from three-dimensional (3D) RTI, the latter of which is more relevant to problems of engineering interest. It is well known that while 2D RTI is unsteady and chaotic, it is not strictly turbulent, since turbulence is a characteristic of 3D flows. In addition, 2D RTI has a faster late-time growth rate, develops larger structures, and is ultimately less well-mixed. These differences have been studied in RTI by Cabot (2006) and Young *et al.* (2001) and in Richtmeyer-Meshkov instability by Olson & Greenough (2014).

For this study, 2D RTI is chosen as the model problem instead of 3D RTI, since it is a good simplified setting for understanding nonlocality in RTI through the lens of MFM. Specifically, 2D RTI simulations are much less computationally expensive than those of 3D RTI, and MFM requires many simulations to attain statistical convergence. Thus, 2D RTI remains the focus of this work, with the hope that the understanding of nonlocality in this flow could be extended to nonlocality in 3D RTI.

In this 2D problem, x is the homogenous direction. In addition, there is no surface tension, the Atwood and Mach (Ma) numbers are finite but small, and the Peclet (Pe) number is finite but large.

3.2. *Generalized eddy diffusivity and higher-order moments*

In this work, the effect of nonlocality on mean scalar transport is of interest, so analysis begins with the scalar transport equation under the assumption of incompressibility:

$$\frac{\partial Y_H}{\partial t} + \nabla \cdot (\mathbf{u} Y_H) = D_H \nabla^2 Y_H, \tag{3.1}$$

where $\mathbf{u}$ is the velocity vector and D_H is the molecular diffusivity of the heavy fluid.

After Reynolds decomposition and averaging, this becomes

$$\frac{\partial \langle Y_H \rangle}{\partial t} + \nabla \cdot (\langle \mathbf{u} \rangle \langle Y_H \rangle) = -\frac{\partial \langle v' Y_H' \rangle}{\partial y} + D_H \nabla^2 \langle Y_H \rangle. \tag{3.2}$$

In this work, large Pe (the ratio of advective transport rate to diffusive transport rate) and small A are assumed. The former assumption means molecular diffusion is negligible, and the latter yields $\langle u_i \rangle = 0$, allowing the advective term to drop. Equation 3.2 becomes

$$\frac{\partial \langle Y_H \rangle}{\partial t} = -\frac{\partial \langle v' Y_H' \rangle}{\partial y}. \tag{3.3}$$

The term $\langle v' Y_H' \rangle$ is the turbulent scalar flux, and this is the unclosed term that needs to be modeled.

As mentioned previously, one reason the gradient diffusion approximation used to model this term is inaccurate is that it assumes locality of the eddy diffusivity. This assumption can be removed by instead considering a generalized eddy diffusivity that is nonlocal in space and time,

as demonstrated by Romanof (1985) and Kraichnan (1987). For 2D RTI, such a model reduces to

$$-\langle v'Y'_H\rangle(y,t) = \int\int D(y,y',t,t')\left.\frac{\partial\langle Y_H\rangle}{\partial y}\right|_{y',t'} dy'dt'. \tag{3.4}$$

Here, y is the spatial coordinate in averaged space and t is the time at which the turbulent scalar flux is measured, y' is all points in averaged space, and t' is all points in time. This definition is exact for passive scalar transport, including in the case studied in this work.

This nonlocal eddy diffusivity can also be viewed as a two-point correlation. This was first described by Taylor (1922) in homogeneous turbulence. Through Lagrangian statistical analysis, Taylor derived the following relation between diffusivity and velocity correlations:

$$D_{ij} = \int_0^\infty \left\langle v_i(t)v_j(t+t')\right\rangle dt'. \tag{3.5}$$

Work by Shende *et al.* (2023) has shown that MFM recovers this Lagrangian formulation for eddy diffusivity in homogeneous flows. It should be noted that the above definition is not valid for inhomogeneous RTI (again, the exact definition of eddy diffusivity for the studied flow is the one in equation 3.4), but the intent here is to provide another interpretation of MFM more aligned with the well-understood two-point correlations.

The eddy diffusivity kernel can be approximated by Taylor-series-expanding the scalar gradient locally about y and t, which results in the following Kramers-Moyal-like expansion for the turbulent scalar flux as done by Kraichnan (1987), Hamba (1995), and Hamba (2004):

$$-\langle v'Y'_H\rangle(y,t) = D^{00}(y,t)\frac{\partial\langle Y_H\rangle}{\partial y} + D^{10}(y,t)\frac{\partial^2\langle Y_H\rangle}{\partial y^2} + D^{01}(y,t)\frac{\partial^2\langle Y_H\rangle}{\partial t\partial y} + D^{20}(y,t)\frac{\partial^3\langle Y_H\rangle}{\partial y^3}\ldots \tag{3.6}$$

$$D^{00}(y,t) = \int\int D(y,y',t,t')dy'dt', \tag{3.7}$$

$$D^{10}(y,t) = \int\int (y'-y)D(y,y',t,t')dy'dt', \tag{3.8}$$

$$D^{01}(y,t) = \int\int (t'-t)D(y,y',t,t')dy'dt', \tag{3.9}$$

$$D^{20}(y,t) = \int\int \frac{(y'-y)^2}{2}D(y,y',t,t')dy'dt'. \tag{3.10}$$

Here, D^{mn} are the eddy diffusivity moments; the first index, m, denotes order in space, while the second, n, denotes order in time. This is the form presented in Mani & Park (2021) and Liu *et al.* (2023).

When the eddy diffusivity kernel is purely local,

$$D(y,y',t,t') = D^{00}\delta(y-y')\delta(t-t'). \tag{3.11}$$

In this case, D^{00} is the only surviving moment, while all higher-order moments in space and time are zero. Any non-zero higher-order moment therefore characterizes the nonlocality of the eddy diffusivity kernel. Thus, this expansion implies explicitly a model form for the turbulent scalar flux that incorporates nonlocality of the eddy diffusivity. Truncating the expansion provides an approximation of $\langle v'Y'_H\rangle$ but with the caveat that the expansion may not converge. This will be discussed in more detail later in §5.3.1.

Each D^{mn} provides more information about the eddy diffusivity kernel with increasing order. For example, D^{00} represents the volume of the kernel in space-time. The coefficient corresponding to one higher-order in space, D^{10}, provides information about the centroid of the kernel in space.

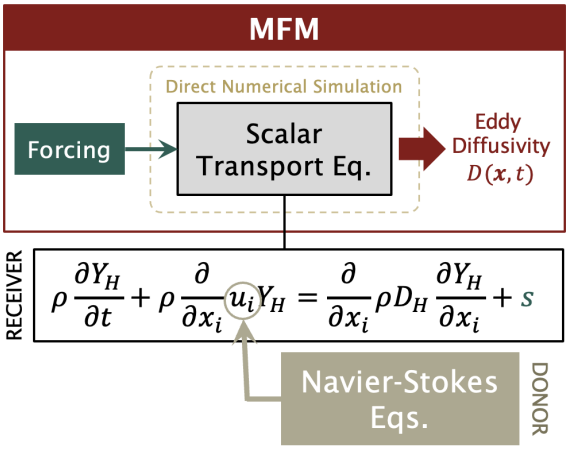

Figure 1: Diagram of MFM pipeline.

D^{20} contains information about the moment of inertia of the kernel in space, D^{01} contains information about the centroid of the kernel in time, and so on.

3.3. *The Macroscopic Forcing Method*

MFM is a method for numerically determining closure operators in turbulent flows (Mani & Park 2021). Much like a rheometer measures the molecular viscosity of a fluid by imposing a shear force on the flow, MFM forces the transport equation in a turbulent flow and extracts the closure operator from its response. Unlike the molecular viscosity, which is a material property, the turbulent closure operator is a property of the flow, so MFM measurements of one flow cannot be generalized for all flows; the MFM-measured closure for one flow cannot be applied exactly as it is to a different flow. However, MFM measurements of one flow can reveal characteristics of the turbulent closure that are expected be true for a family of similar flows.

Specifically, MFM can be used to determine the RANS closure operator, as shown in the pipeline diagram in figure 1. In MFM, two simulations are run at once: the donor and the receiver simulation. In this work, the donor simulation numerically solves the multicomponent Navier-Stokes equations in equations 4.1 - 4.4. The receiver simulation "receives" u_i from the donor simulation and uses it to solve the scalar transport equation with a forcing s:

$$\rho\frac{\partial Y_H}{\partial t}+\rho\frac{\partial}{\partial x_i}\left(u_iY_H\right)=\frac{\partial}{\partial x_i}\left(\rho D_H\frac{\partial}{\partial x_i}Y_H\right)+s. \tag{3.12}$$

Ultimately, forcings on the receiver simulation effect a response from the flow, and measuring this response allows for determination of the eddy diffusivity. In particular, these forcings are *macroscopic*. Here, macroscopic quantities are defined as fields that are unchanged by Reynolds-averaging. Mathematically, the macroscopic forcing is such that $s=\overline{s}$. This macroscopic nature is crucial to the method, since it does not disturb the underlying mixing process, which allows for measurement of the closure operator without changing it. For details, see Mani & Park (2021).

In actuality, the Inverse Macroscopic Forcing Method (IMFM) is used to determine eddy diffusivity moments. That is, instead of the forcings being chosen, certain mean mass fraction fields are chosen. Numerically, mean mass fractions are enforced in each realization, so the averages (denoted by $\overline{*}$) described here are in x, the homogeneous direction in space. The forcing needed to maintain the chosen $\overline{Y_H}$ is determined implicitly along the process and is not directly used in the analysis.

As an illustration, the measurement of D^{00} can be considered. According to equation 3.6, choosing $\overline{Y_H}=y$ (for y between $-1/2$ and $1/2$) results in $\frac{\partial\overline{Y_H}}{\partial y}=1$, and all other higher-order

derivatives are zero. Thus, choosing this $\overline{Y_H}$ in each realization results in the realization- and spatially-averaged measurement $-\langle v'Y'_H\rangle = D^{00}$.

Measurement of higher-order moments involves similar choices of $\overline{Y_H}$ but requires information from lower order moments. For example, measuring D^{10} involves choosing $\overline{Y_H} = y^2$, which results in $-\langle v'Y'_H\rangle = yD^{00} + D^{10}$. Here, D^{00} comes from the simulation using $\overline{Y_H} = y$. Thus, D^{10} is computed by subtracting yD^{00} from the $\langle v'Y'_H\rangle$ measurement from the simulation using $\overline{Y_H} = y^2$.

Specifically, the following desired mean mass fractions are used for each moment for y between $-1/2$ and $1/2$:

$$\overline{Y_H} = y \Rightarrow D^{00}, \tag{3.13}$$

$$\overline{Y_H} = \frac{1}{2}y^2 \Rightarrow D^{10}, \tag{3.14}$$

$$\overline{Y_H} = yt \Rightarrow D^{01}, \tag{3.15}$$

$$\overline{Y_H} = \frac{1}{6}y^3 + \frac{1}{48} \Rightarrow D^{20}. \tag{3.16}$$

From these $\overline{Y_H}$, the needed forcing in each timestep is numerically determined:

$$s^k = \frac{\overline{Y_{H\,\text{desired}}}^{k} - \overline{Y_H}^{k-1}}{\Delta t} \tag{3.17}$$

where the superscript k denotes the timestep number, $\overline{Y_{H\,\text{desired}}}$ is the mean mass fraction desired as outlined in equations 3.13 - 3.16, and Δt is the timestep size.

This MFM forcing bears some resemblance to other forcings used in the literature, such as interaction by exchange with the mean (IEM) (Sawford 2004; Pope 2001). One main difference between forcings in such methods and MFM is that the purpose of the latter is to drive the flow to a specified mean gradient, which allows for measurement–not enforcement –of the eddy diffusivity moments. In other words, in MFM for scalar transport, the input is a mean scalar gradient, and the output is the eddy diffusivity moment; in IEM and similar methods, the input is a desired moment (e.g., in IEM, the input moment is $\langle c^2\rangle$) and the output is a mixing model. In addition, methods such as IEM use microscopic forcings, while MFM uses macroscopic forcings, which is a distinguishing characteristic of the latter method.

To determine D^{00}, D^{10}, D^{01}, and D^{20}, four separate simulations are needed. For each of these simulations, the moments can be calculated using measurements of the turbulent scalar flux as follows:

$$D^{00} = F^{00}, \tag{3.18}$$

$$D^{10} = F^{10} - yD^{00}, \tag{3.19}$$

$$D^{01} = F^{01} - tD^{00}, \tag{3.20}$$

$$D^{20} = F^{20} - yD^{10} - \frac{1}{2}y^2D^{00}. \tag{3.21}$$

where F^{mn} denotes the $-\langle v'Y'_H\rangle$ measured from the receiver simulation using the forcing corresponding the moment D^{mn}.

3.4. *Self-similarity analysis*

We perform our analysis in the self-similar regime. First, we define a self-similar coordinate:

$$\eta = \frac{y}{h(t)}, \tag{3.22}$$

so that $\langle Y_H \rangle$ is only a function of η. Note that η requires a definition of $h(t)$. From the previous discussion on the self-similarity of RTI, an appropriate definition is $h(t) = \alpha A g t^2$.

Through self-similar analysis of equation 3.6, the eddy diffusivity moments and turbulent scalar flux can be normalized. Details of this process can be found in the Appendix.

3.5. *Algebraic fit to mixing width*

Recall that $h(t) = \alpha A g t^2$ is used in the self-similarity analysis. This is valid only for late time, so the subsequent analyses in this work are all done in this self-similar timeframe. Usually, α can be determined from $\frac{h(t)}{Agt^2}$, where $h(t)$ is computed from the simulation via equation 2.5. However, due to the convergence and statistical errors as well as the existence of a virtual time origin, $\alpha A g t^2$ is not a good representation of $h(t)$ measured in the DNS. Instead, a fitting coefficient α^* and virtual time origin t^* are determined to make a shifted quadratic fit to $h(t)$ from the simulation:

$$h_{\text{fit}}(t) = \alpha^* A g (t - t^*)^2. \tag{3.23}$$

With this fit, the normalizations of the turbulent scalar flux and moments become

$$\widehat{\langle v' Y_H' \rangle} = \frac{\langle v' Y_H' \rangle}{\alpha^* A g (t - t^*)}, \tag{3.24}$$

$$\widehat{D^{00}} = \frac{D^{00}}{\alpha^{*2} A^2 g^2 (t - t^*)^3}, \tag{3.25}$$

$$\widehat{D^{10}} = \frac{D^{10}}{\alpha^{*3} A^3 g^3 (t - t^*)^5}, \tag{3.26}$$

$$\widehat{D^{01}} = \frac{D^{01}}{\alpha^{*2} A^2 g^2 (t - t^*)^4}, \tag{3.27}$$

$$\widehat{D^{20}} = \frac{D^{20}}{\alpha^{*4} A^4 g^4 (t - t^*)^7}. \tag{3.28}$$

For exact self-similarity, plots of the measured $\widehat{D^{mn}}$ against η must be independent of time. This expectation sets a criterion to assess the extent to which ideal self-similarity is achieved. Plots and assessment of the self-similar collapse of the measurements presented in this work are in the Appendix.

4. Simulation details

4.1. *Governing equations*

The governing equations solved in this work are the compressible multicomponent Navier-Stokes equations, which involve equations for continuity, diffusion of mass fraction Y_α of species α (characterized by its binary molecular diffusivity D_α), momentum transport, and transport of specific internal energy e:

$$\frac{D\rho}{Dt} = -\rho \frac{\partial u_i}{\partial x_i}, \tag{4.1}$$

$$\rho \frac{DY_\alpha}{Dt} = \frac{\partial}{\partial x_i} \left(\rho D_\alpha \frac{\partial Y_\alpha}{\partial x_i} \right), \tag{4.2}$$

$$\rho \frac{Du_j}{Dt} = -\frac{\partial}{\partial x_i} \left(p\delta_{ij} + \sigma_{ij} \right) + \rho g_j, \tag{4.3}$$

$$\rho \frac{De}{Dt} = -p \frac{\partial u_i}{\partial x_i} + \frac{\partial}{\partial x_i} \left(u_i \sigma_{ij} - q_j \right). \tag{4.4}$$

Here, $\frac{D}{Dt}$ is the material derivative $\frac{\partial}{\partial t} + u_i \frac{\partial}{\partial x_i}$, ρ is density, u is velocity, p is pressure, and g is gravitational acceleration, active in the $-y$ direction. The viscous stress tensor σ_{ij} and heat flux vector q_j are respectively defined as

$$\sigma_{ij} = \mu \left(\frac{\partial u_i}{\partial x_j} + \frac{\partial u_j}{\partial x_i} \right) - \mu \frac{2}{3} \frac{\partial u_k}{\partial x_k} \delta_{ij}, \tag{4.5}$$

$$q_j = -\kappa \frac{\partial T}{\partial x_j} - \sum_{\alpha=1}^{N} h_\alpha \rho D_\alpha \frac{\partial Y_\alpha}{\partial x_j}. \tag{4.6}$$

Here, μ is the dynamic viscosity, κ is the thermal conductivity, T is temperature, and h_α is the specific enthalpy of species α.

Component pressures and temperatures of each species are determined using ideal gas equations of state. Under the assumption of pressure and temperature equilibrium, an iterative process is performed to determine volume fractions v_α that allow for computation of partial densities and energies. More details on the hydrodynamics equations and computation of component quantities can be found in Morgan *et al.* (2018).

Finally, total pressure is determined as the weighted sum of component pressures:

$$p = \sum_{\alpha=1}^{N} v_\alpha p_\alpha. \tag{4.7}$$

In general, in these compressible equations, Y_α are not passive scalars. However, the component equations of state are scaled so that a consistent hydrostatic pressure gradient is maintained across the mixing layer. Thus, in this work, Y_α are effectively passive.

4.2. *Computational approach*

Simulations for 2D RTI are run using the Ares code, a hydrodynamics solver developed at Lawrence Livermore National Laboratory (LLNL) (Morgan & Greenough 2015; Bender *et al.* 2021). Ares employs an arbitrary Lagrangian-Eulerian (ALE) method based on the one by Sharp & Barton (1981), in which the governing equations (equations 4.1 to 4.4) are solved in a Lagrangian frame and then remapped to an Eulerian mesh through a second-order scheme. The spatial discretization is a second-order non-dissipative finite element method, and time advancement is a second-order explicit predictor-corrector scheme.

The Reynolds number (more specifically, the kinematic viscosity ν) is set through a numerical Grashof number, such that

$$\nu = \sqrt{\frac{-2gA\Delta^3}{Gr}}. \tag{4.8}$$

Here, Δ is the grid spacing; in the simulations, a uniform mesh is used, and $\Delta = \Delta x = \Delta y$. To ensure that the unsteady structures are properly resolved and for the simulation to appropriately be considered a DNS, Gr should be kept small. A Gr that is too large results in a simulation with dissipation dominated by numerics rather than the physics. Morgan & Black (2020) found that past $Gr \approx 12$ in the Ares code, numerical diffusivity dominates molecular diffusivity. For our simulations, we use $A = 0.05$ and $Gr = 1$, the latter of which is in line with the DNS by Cabot & Cook (2006). These choices give a ν of $10^{-9} m^2/s$. The Schmidt number Sc, defined as ν/D_M, is set to unity, so $D_M = 10^{-9} m^2/s$.

The Mach number, $Ma = \frac{u}{c}$, where c is the speed of sound, characterizes compressibility effects of the flow. Ma is set by the specific heat ratio γ, which is $5/3$ in the simulations im this work. The maximum Ma is measured at the last timestep to be approximately 0.03, which is ascertained to be small enough to assume incompressibility.

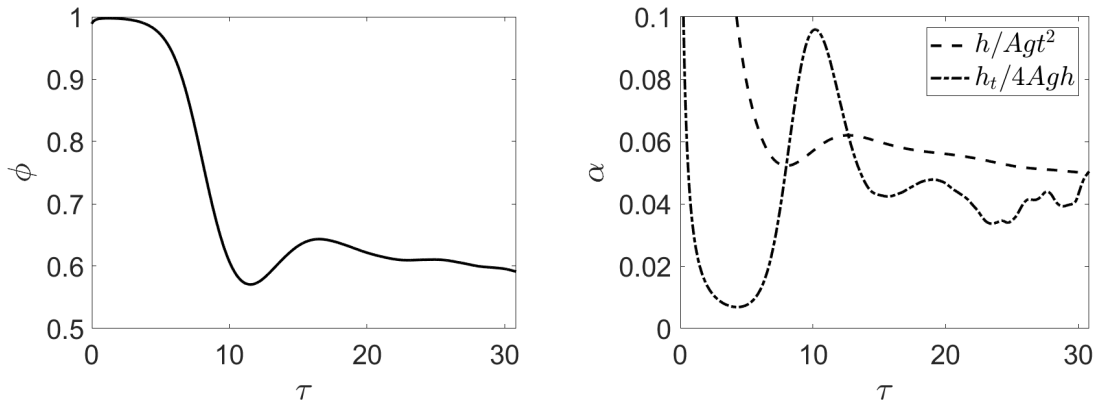

(a) (b)

Figure 2: Self-similarity parameters computed from a donor simulation.

The Peclet number Pe characterizes the advection versus diffusion rate and is defined as $ReSc$. Here, a Pe_L and a Pe_T are reported, which use a large-scale Re_L and the Taylor Reynolds number Re_T, respectively. In the presented simulations, $Sc = 1$. The two Pe are computed in post-processing: Pe_L is approximately $8,000$, and Pe_T is approximately 54. Both are below the criterion established by Dimotakis (2000), suggesting that the simulated flow is transitional or pre-transitional.

The number of cells in each simulation is 2049×2049. The width L_x of the domain is 1, and the height L_y is 1. The boundary conditions are periodic in x and no slip and no penetration in y.

Initially, the velocity field is zero, temperature is 293.15 K, and pressure is 1 atm. A tophat perturbation based on the ones used by Morgan & Greenough (2015) and Morgan (2022) is imposed on the density field at the interface of the heavy and light fluids:

$$\xi(x) = \sum_{k=\kappa_{\min}}^{\kappa_{\max}} \frac{\Delta}{\kappa_{\max} - \kappa_{\min} + 1} \left(\cos\left(2\pi k x + \phi_{1,k}\right) + \sin\left(2\pi k x + \phi_{2,k}\right)\right), \tag{4.9}$$

$$\rho(x, y) = \rho_L + \frac{\rho_H - \rho_L}{2}\left(1 + \tanh\left(\frac{y - L_y/2 + \xi}{2\Delta}\right)\right), \tag{4.10}$$

where $\phi_{1,k}$ and $\phi_{2,k}$ are phase shift vectors randomly taken from a uniform distribution, and L_y is the length in y of the domain. Here, the minimum and maximum wavenumbers are set to $\kappa_{\min} = 8$ and $\kappa_{\max} = 256$, respectively.

The stop condition of the simulations is when h is approximately half the domain size in y. This corresponds to the nondimensional simulation time τ of 30.84. τ is defined as $\frac{t}{t_0}$, where $t_0 = \sqrt{\frac{h_0}{Ag}}$ and h_0 is the dominant lengthscale determined by the peak of the initial perturbation spectrum.

Before the MFM analysis was conducted, the results of the donor simulations were examined. In figure 2a, mixedness is observed to reach a value of around 0.6 but appears to not have converged yet. Figure 2b shows the two definitions of α over time. The first definition, $\alpha = h/Agt^2$, reaches a value of about 0.05 by the end of the simulation, but it does not appear to be converged. The second definition, $\alpha = \dot{h}^2/4Agh$, is oscillatory, due to the sensitivity of the time derivative to noise, and it appears to fluctuate about a value of approximately 0.04. It is acknowledged that this behavior indicates that the RTI simulated here is only weakly turbulent. However, it is observed that the flow is still self-similar at late times. The contour plot of $\langle Y_H \rangle$ in figure 3 exhibits parallel contour lines after $\tau \approx 17$, indicating self-similarity at those times. It is also shown in

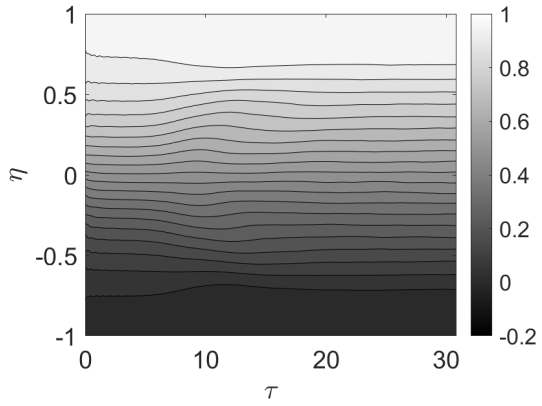

Figure 3: Contours of $\langle Y_H \rangle$ showing self-similarity at late times.

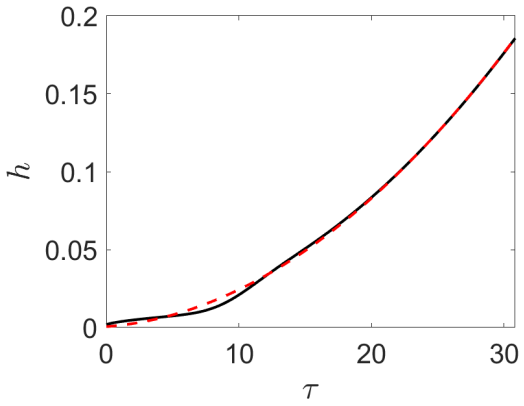

Figure 4: Black solid line: h measured from DNS; red dashed line: h_{fit}.

the Appendix that the mean concentration and normalized turbulent scalar flux profiles exhibit self-similar collapse after $\tau \approx 17$, so the presented self-similar analysis is valid.

Figure 4 shows a plot of the algebraic fit for h, described in equation 3.23. For the simulations presented here, α^* is 0.0046 and t^* is -1.6×10^3. The plot shows a strong quadratic dependence of h on t at late time, as h_{fit} matches DNS at $\tau \gtrapprox 17$, validating the self-similar ansatz of $h \sim t^2$.

To further ensure the simulations are working as desired, the flow fields of the donor and receiver simulations can be examined qualitatively. The Y_H contours at the last timesteps of each simulation are shown in figure 5. The receiver simulation shown is the one used to compute D^{00} (where $\langle Y_H \rangle = y$). Self-similar RTI turbulent mixing is observed at this timestep, where the characteristic heavy spikes are sinking into the lighter fluid and the light bubbles rise into the heavier fluid. Both simulations have the same velocity fields, since the receiver simulation "receives" the velocity field from the donor simulation. In contrast with the donor simulation, which has a stark black-and-white difference between the heavy and light fluids, there is a grey gradient of density in the receiver simulation due to the imposed mean scalar gradient. The fluctuations of Y_H in each simualtion are also compared in figure 6. The Y_H' contours are not identical but are qualitatively very similar. In both simulations, Y_H' is constrained to the mixing layer. Based on these observations, it is concluded that the simulations are visually working as intended.

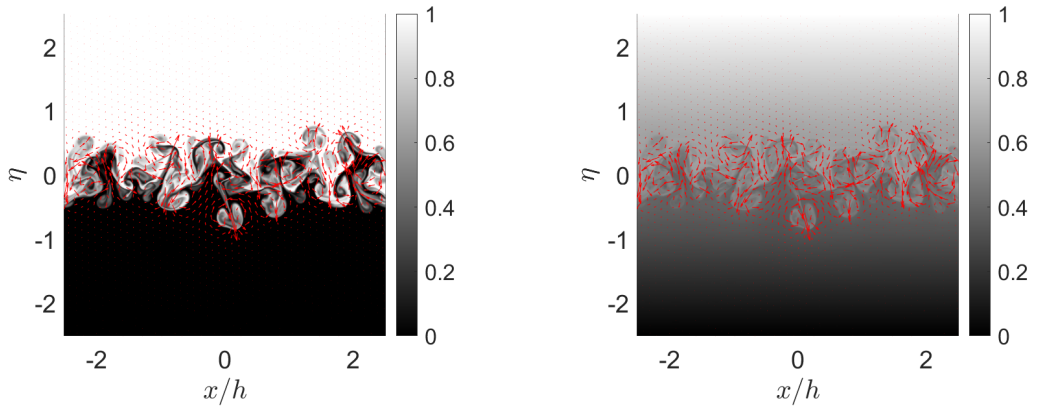

(a) (b)

Figure 5: Y_H contours (black: light, white: heavy) and velocity vector fields (red arrows) of the (a) donor simulation and (b) receiver simulation with s enforcing $\langle Y_H \rangle = y$. These snapshots are taken at the last timestep.

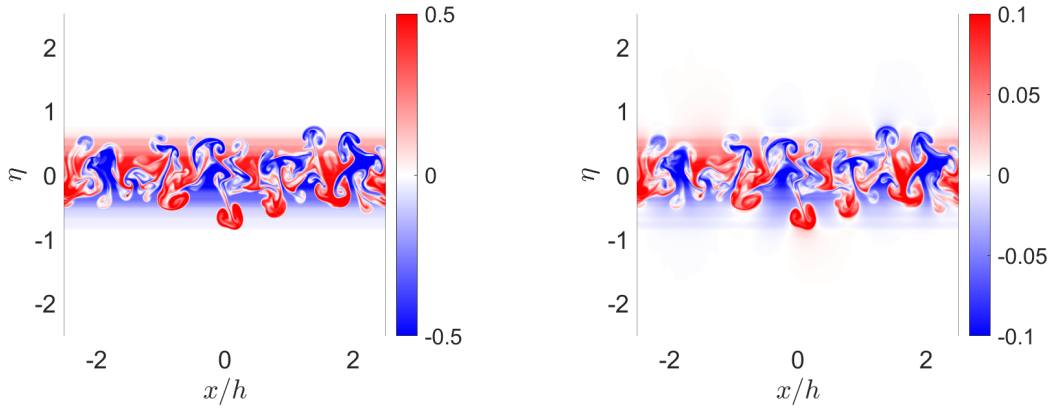

(a) (b)

Figure 6: Y'_H contours of the (a) donor simulation and (b) receiver simulation. These snapshots are taken at the last timestep. Note that different colorbars have been used to improve interpretability.

5. Results

5.1. *Eddy diffusivity moments*

Figure 7 shows normalized MFM measurements of the eddy diffusivity moments D^{00}, D^{10}, D^{01}, and D^{20} averaged over $1,000$ realizations and the homogeneous direction x. Some expected characteristics of the measured moments are observed:

(i) The leading order moment is over two magnitudes larger than the molecular diffusivity ($10^{-9} m^2/s$). The scaled higher order moments shown are all at least one magnitude larger than the molecular diffusivity.

(ii) D^{00} is symmetric and always positive.

(iii) D^{10} is antisymmetric. This antisymmetry can be understood by interpreting D^{10}/D^{00} as the centroid of the eddy diffusivity kernel. Physically, for $\eta > 0$, it is expected that the mean scalar gradient at the center of the mixing layer (at a negative distance away) has more influence on the turbulent scalar flux than the mean scalar gradient at the outer edges, since the mixing layer is

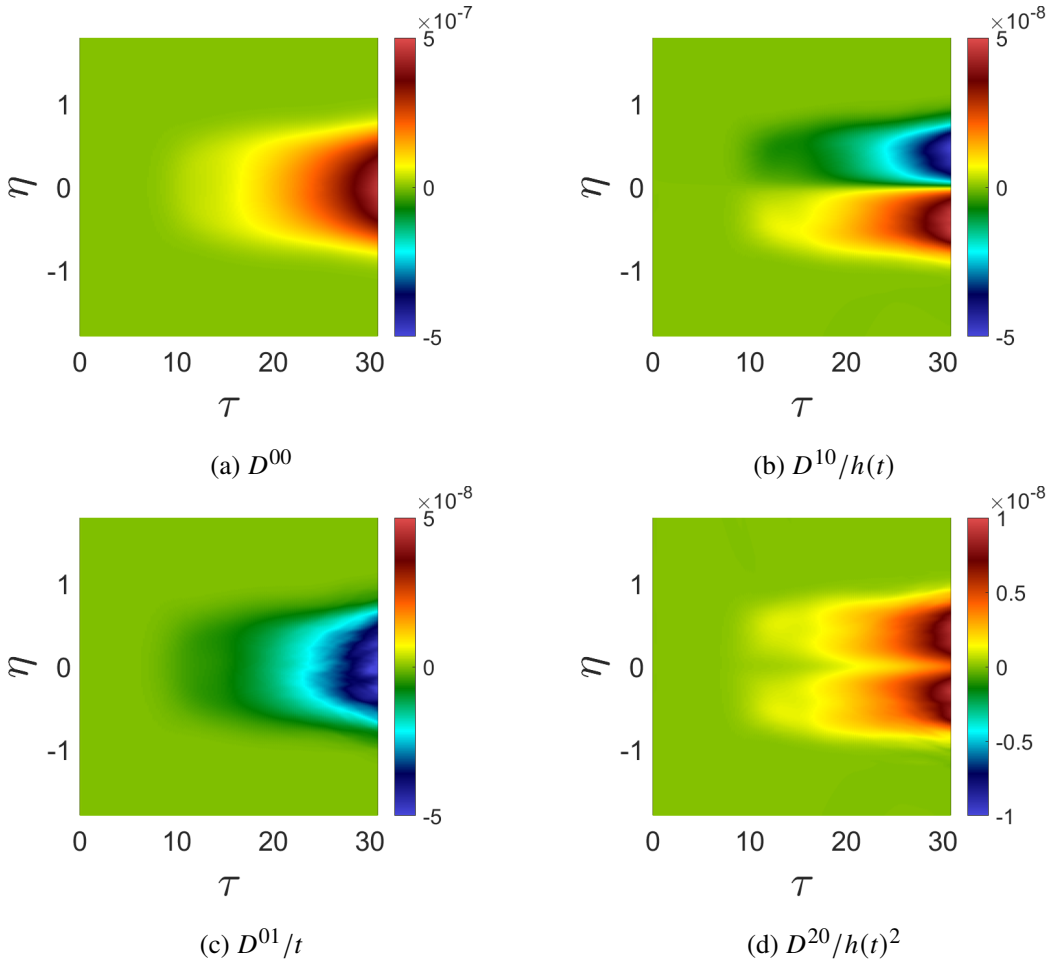

(a) D^{00} (b) $D^{10}/h(t)$

(c) D^{01}/t (d) $D^{20}/h(t)^2$

Figure 7: Moments of eddy diffusivity kernel normalized by appropriate length and timescales. Data averaged over 1,000 realizations and homogeneous direction x.

growing outwards. This makes the eddy diffusivity kernel skewed more towards the center of the domain, so $D^{10} < 0$ for $\eta > 0$. A similar effect occurs for $\eta < 0$, which results in $D^{10} > 0$.

(iv) D^{01} is symmetric and always negative. The latter must be true for the flow to depend on its history (it does not violate causality).

(v) D^{20} is symmetric and always positive, as is characteristic of moment of inertia of a positive kernel.

Based on the magnitudes of the normalized moments, some initial observations on importance of each moment can be made. D^{00} has the highest magnitude of all the moments, which is expected since it is the leading-order moment. The magnitudes of D^{10}/h and D^{01}/t are on the order of 10% of the magnitude of D^{00}, which suggests that they are non-negligible. On the other hand, the magnitude D^{20}/h^2 is on the order of 1% that of D^{00}, so D^{20} is likely not an important moment to include in modeling RTI. More robust studies will be presented in the following sections to determine importance of each of the eddy diffusivity moments.

It is also observed that there is statistical error in the measurements. Due the chaotic nature of RTI, the moment measurements contain statistical error, but this error can be reduced by averaging many realizations. To demonstrate statistical convergence of the measurements, plots of D^{00} averaged over different numbers of realizations are included in figure 8. As the number of realizations increases, the plots become smoother, and it is found that after $1,000$ realizations, the rate of reduction in statistical error slows down significantly. Averaging over this number of

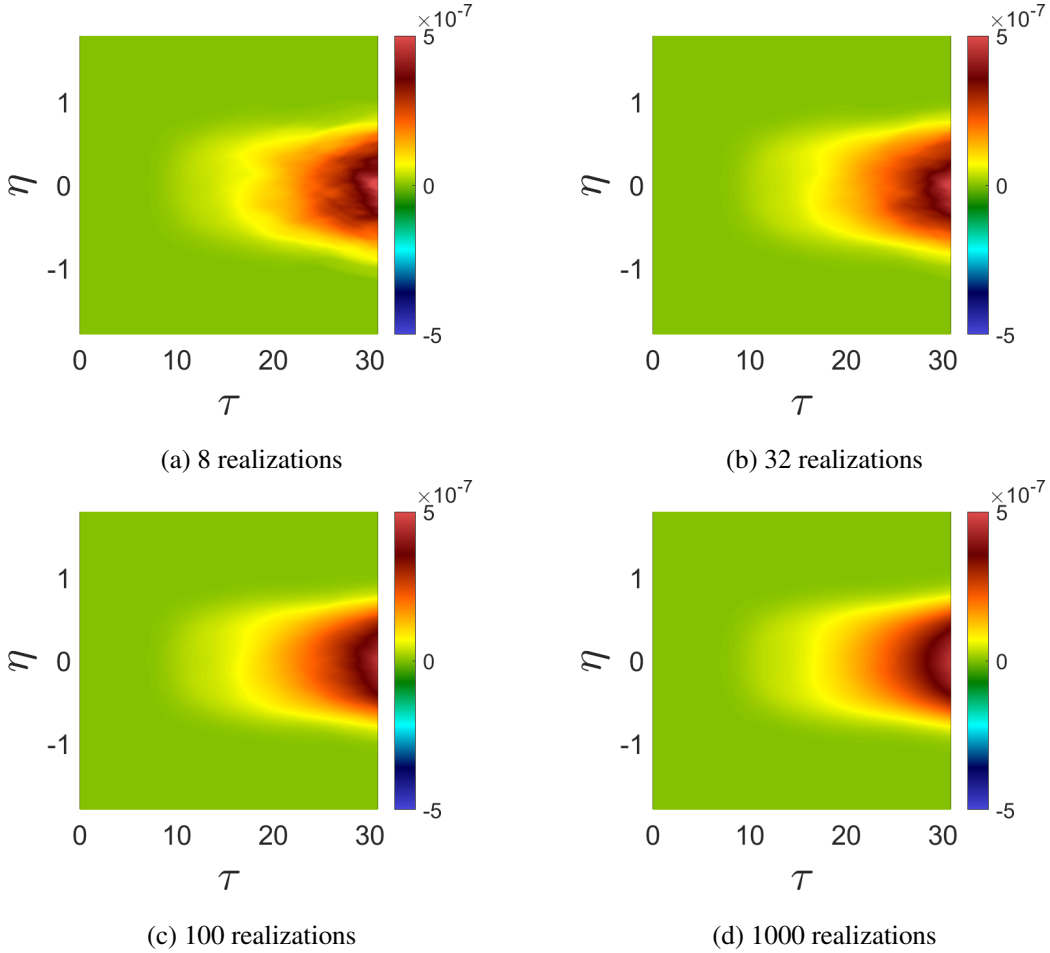

(a) 8 realizations

(b) 32 realizations

(c) 100 realizations

(d) 1000 realizations

Figure 8: D^{00} averaged over different numbers of realizations.

realizations results in a smooth D^{00} measurement and higher-order moment measurements with acceptably less statistical error.

Additionally, the higher the order of the moment, the slower its rate of statistical convergence. Recall that determination of higher-order moments requires information from lower-order moments. For example, in determining D^{01}, tD^{00} is subtracted from F^{01}, the turbulent scalar flux measurement in the simulation associated with D^{01}. Naturally, there is statistical error associated with both D^{01} and D^{00}. However, the error in D^{00} is amplified by t, so the overall statistical error of D^{01} increases with time. This statistical error "leakage" occurs for all higher-order moments. The higher the order of the moment, the worse the statistical error, since information from more lower-order moments is needed, and so more statistical error is accumulated and amplified. The relatively high statistical error of the higher-order moments makes it challenging to study their importance. Particularly, taking derivatives of quantities with high statistical error amplifies the error, so smoother measurements are desired. In this work, the moment measurements are smoothed using a Savitzky-Golay filter function in Matlab with a polynomial order of unity and window size of 191. These smoothed moments are shown in figure 9. While it is possible to design an alternative formulation of MFM that removes leakage of statistical error from low-order moments to higher-order moments (see Lavacot *et al.* 2022), for this 2D study and for the order of moments considered here, the statistical convergence is sufficient.

Using these measurements, nonlocal timescales and lengthscales (t_{NL} and L_{NL}, respectively)

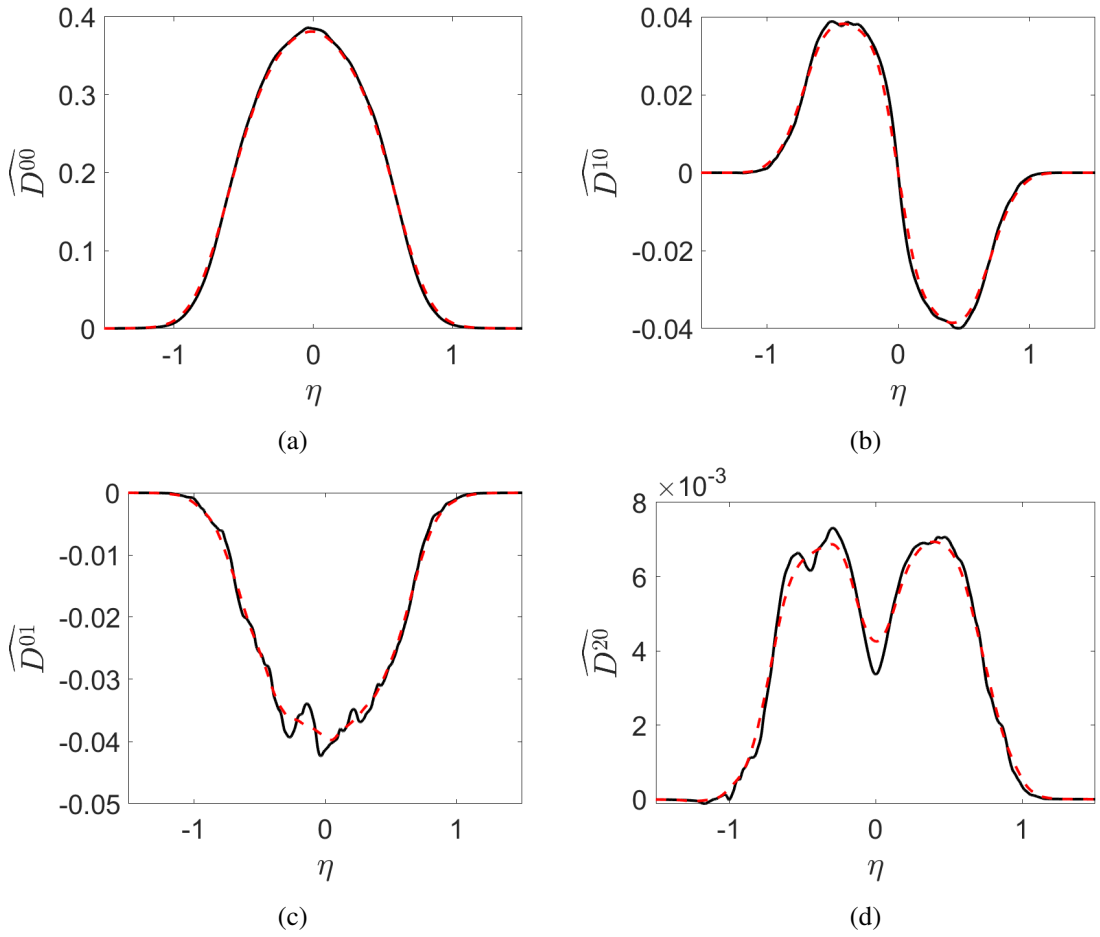

Figure 9: Smoothed moments (dashed red) over raw MFM measurements of moments (solid black). The moments are taken from the mean data at the last timestep of the simulations and are transformed to self-similar space.

can be defined:

$$t_{NL} = -\frac{D^{01}}{D^{00}}, \quad L_{NL} = \sqrt{\frac{D^{20}}{D^{00}}}. \tag{5.1}$$

Note that this analysis can only be done for $-1 \leqslant \eta \leqslant 1$, since the moments are analytically zero outside the mixing layer.

Nondimensionally, the nonlocal timescale is $\tau_{NL} = t_{NL}/t_0$, and the nonlocal lengthscale is $\eta_{NL} = L_{NL}/h$. Contour plots of the nondimensionalized nonlocal timescale and lengthscale are in figure 10. Note that τ_{NL} scales as τ, so profiles of τ_{NL}/τ against η are also plotted in figure 11 in the self-similar time regime ($\tau > 17$). The scaled profiles collapse and have a centerline value of approcimately 0.1. This means that the mean fluxes at some time τ are affected by mean scalar gradients 0.1τ earlier. Figure 12 shows the minimum nonlocal lengthscale is at the centerline, where $\eta_{NL} \approx 0.09$. The maximum lengthscales occur near the outer edges of the mixing layer: at around $\eta = \pm 0.87$, $\eta_{NL} \approx 0.27$. This indicates that mean fluxes at the mixing layer edges depend mostly on mean scalar gradients about a quarter of a mixing width away, while mean fluxes at the centerline depend on mean scalar gradients about one tenth of a mixing width away; nonlocality appears to be stronger at the mixing layer edges than at the centerline. These nonlocal properties of the eddy diffusivity for RTI could not be predicted without direct measurement of the eddy diffusivity moments, which has been made possible through MFM.

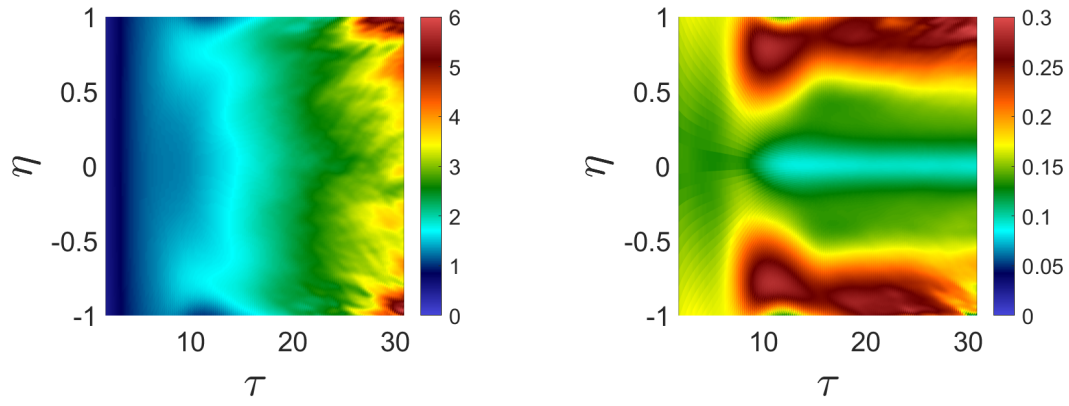

(a) τ_{NL} (b) η_{NL}

Figure 10: Nondimensional nonlocal timescale and lengthscale contours. Only $-1 \leqslant \eta \leqslant 1$ is plotted, since moments are zero outside the mixing layer. Early times ($\tau < 2$) not plotted due to transient behavior.

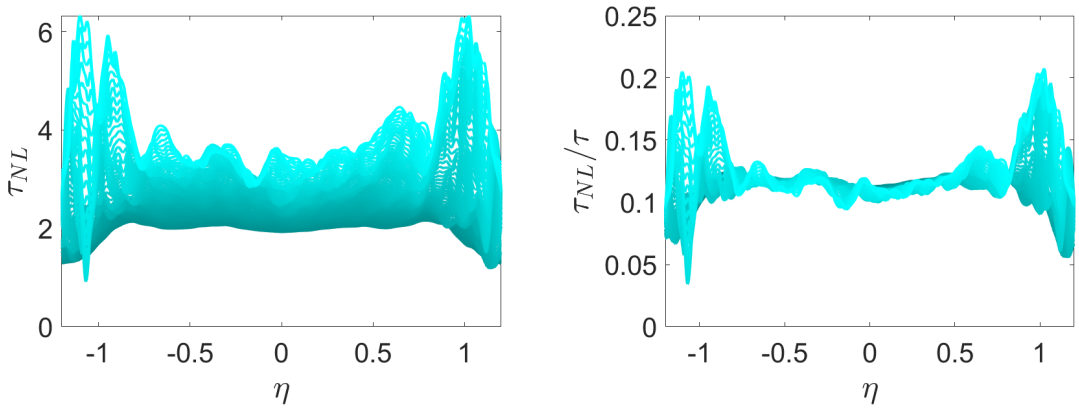

(a) (b)

Figure 11: Nondimensional nonlocal timescale profiles at different times for $\tau > 17$. Lighter lines correspond to later times; darker lines correspond to earlier times. (a) is unscaled and shows the linear time dependence of τ_{NL} on τ. (b) shows the collapse of the profiles when scaled by τ.

5.2. *Assessment of importance of nonlocal effects*

5.2.1. *Comparison of terms in turbulent scalar flux expansion*

To aid in the determination of which moments are important for a RANS model, a comparison of the terms in the expansion of the turbulent scalar flux (equation 3.6) is presented. These terms involve gradients of $\langle Y_H \rangle$. Instead of using $\langle Y_H \rangle$ directly from the DNS, a fit to $\langle Y_H \rangle$ is used, since the statistical error in the raw measurement gets amplified by derivatives in η. That is, the quantities of interest are sufficiently converged for plotting but not for operations involving

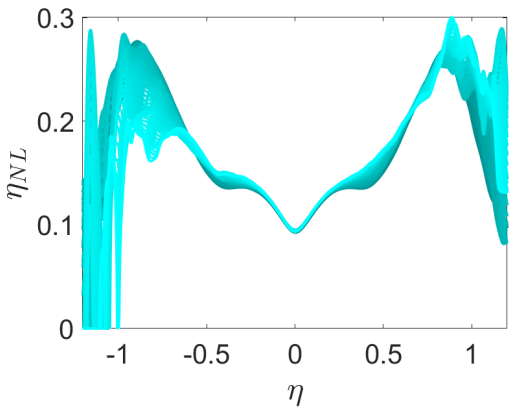

Figure 12: Nondimensional nonlocal lengthscale profiles at different times for $\tau > 17$. Lighter lines correspond to later times; darker lines correspond to earlier times.

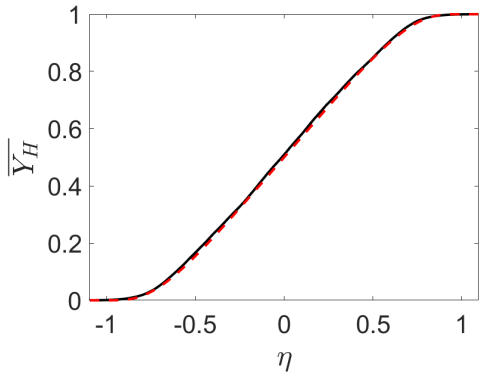

Figure 13: Semi-analytical fit to $\langle Y_H \rangle$ (dashed red) against DNS measurement of $\langle Y_H \rangle$ (solid black).

derivatives. Thus, an analytical fit to $\langle Y_H \rangle$ is obtained as follows:

$$\langle Y_H \rangle^* = \begin{cases} 0 & \text{if } \eta < -a \\ \int_{-a}^{\eta} \frac{1}{\left(a^2-\eta'^2\right)^2} \exp\left(\frac{1}{B\left(a^2-\eta'^2\right)}\right) d\eta' & \text{if } -a \leqslant \eta \leqslant a \\ 1 & \text{if } \eta > a \end{cases}, \tag{5.2}$$

$$\langle Y_H \rangle = \frac{\langle Y_H \rangle^*}{\langle Y_H \rangle^*_{\max}}, \tag{5.3}$$

where the integral is determined numerically, and a and B are fitting coefficients. The coefficients $a^2 = 1.2$ and $B = 0.36$ are found to give good agreement to the mean concentration profile from DNS, as shown in figure 13.

The terms on the right hand side of equation 3.6 are plotted against the DNS measurement of the turbulent scalar flux in figure 14. Clearly, the $\widehat{D^{00}}$ term is not enough to capture the turbulent scalar flux. It is observed that the $\widehat{D^{01}}$ term is significant in magnitude in the middle of the domain, and the $\widehat{D^{10}}$ term carries importance at the outer edges of the mixing layer. The term associated with the highest-order moment that was measured, $\widehat{D^{20}}$ also appears to be of similar magnitude as the other moments, indicating it may also carry important information about nonlocality of the eddy diffusivity. These preliminary findings indicate nonlocality is certainly important for accurate modeling of mean scalar transport in this RTI problem, since the higher-order terms

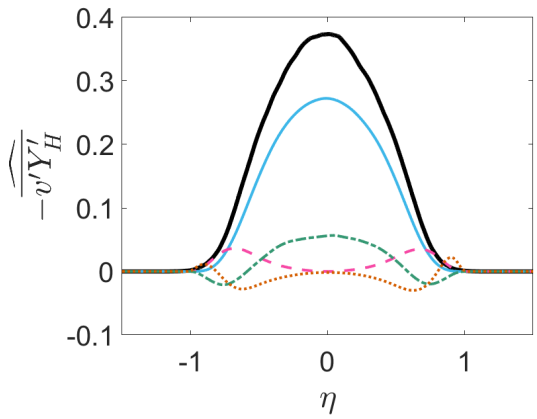

Figure 14: Comparison of terms in the expansion of the turbulent scalar flux. Black: DNS measurement of turbulent scalar flux, solid blue: $\widehat{D^{00}}$ term, dashed pink: $\widehat{D^{10}}$ term, dash-dotted green: $\widehat{D^{01}}$ term, dotted orange: $\widehat{D^{20}}$ term.

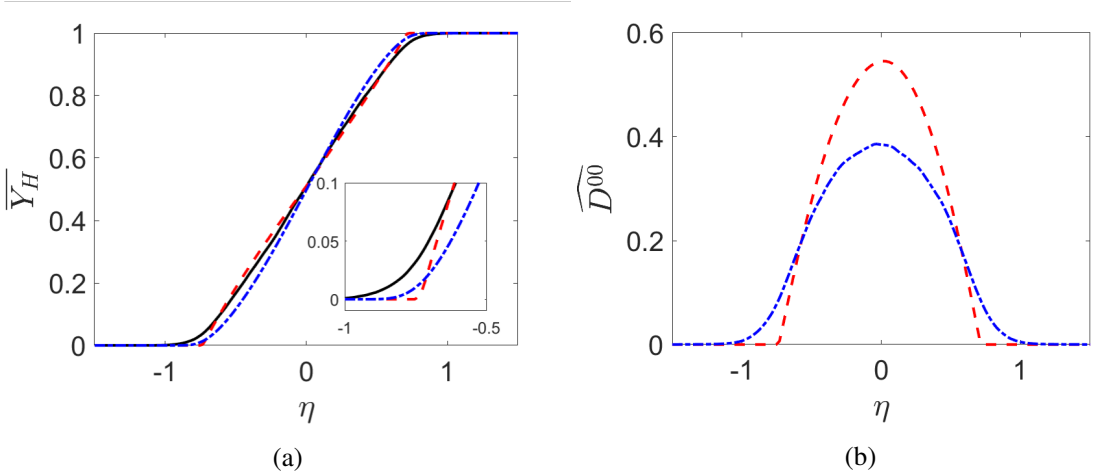

(a) (b)

Figure 15: Comparisons of (a) model coefficient from k-L model with leading-order moment measured using MFM and (b) resulting similarity solutions for $\langle Y_H \rangle$. Inset plot in (a) shows zoomed-in view around $\eta = -1$ to highlight divergence of k-L model from DNS. Solid black: DNS measurement, dash-dotted blue: leading-order MFM-based model, dashed red: k-L model.

in equation 3.6 appear non-negligible compared to the leading-order term. It may be tempting to ascribe physical reasons for the behavior of the terms plotted in figure 14, but this is not so straightforward, especially since the full eddy diffusivity kernel for this problem as not yet been measured. Further, it would be inappropriate to draw conclusions about importance of each eddy diffusivity moment in a RANS model, since the operator form must be scrutinized first. A faulty operator form could give misleading implications about certain eddy diffusivity moments. It turns out that a simple superposition of these terms, which would represent a truncation of equation 3.6, does not accurately represent the true eddy diffusivity kernel and actually leads to divergence of predictions, so such an operator form would not be appropriate; this will be covered more in depth later in §5.3. Nevertheless, the results shown here are strong evidence of nonlocality of the eddy diffusivity kernel for the RTI simulated here.

5.2.2. *Comparison of leading-order model against a local model*

To demonstrate the shortcomings of models using purely local coefficients, an MFM-based leading-order model and the k-L RANS model are compared. The intent of this study is not to immediately propose a "better" RANS model to replace k-L, nor is it to suggest the MFM-based leading-order model is more accurate than the k-L model. In fact, it is expected that the MFM-based leading-order model will perform poorly, since it does not include important higher-order moments of eddy diffusivity. Instead, this study emphasizes the necessity of higher-order moments and shows how MFM can reveal incorrect model forms.

In particular, a 1D k-L simulation is run, and the eddy diffusivity and mean concentration profiles are extracted from the results to be compared to those of the MFM-based model using the measured D^{00} that was presented in §5.1. The k-L simulation used in this section is implemented in Ares, and details of the implementation are in Morgan & Greenough (2015) and Morgan (2018). Note that the k-L simulation is used here for illustration purposes and should not be confused with the 2D DNS simulations used to obtain our MFM moments.

The MFM-measured D^{00} is used for the leading-order MFM-based model:

$$-\langle v'Y_H'\rangle = D^{00}_{\text{MFM}}\frac{\partial\langle Y_H\rangle}{\partial y}. \tag{5.4}$$

To solve this, D^{00}_{MFM} is obtained from the smoothed MFM measurements and transformed to self-similar coordinates. The resulting $\widehat{D^{00}_{\text{MFM}}}$ is a function of $\eta = \frac{y}{h_{\text{DNS}}}$, where $h_{\text{DNS}} = \alpha^*_{\text{DNS}} Ag(t - t^*_{\text{DNS}})^2$ is an algebraic fit to the mixing width from the DNS. The equation is then solved semi-analytically in conjunction with the mean mass fraction evolution equation in self-similar coordinates:

$$-2\eta\frac{d\langle Y_H\rangle}{d\eta} = \frac{d}{d\eta}\left(-\widehat{\langle v'Y_H'\rangle}\right), \tag{5.5}$$

$$-\widehat{\langle v'Y_H'\rangle} = \widehat{D^{00}_{\text{MFM}}}\frac{d\langle Y_H\rangle}{d\eta}. \tag{5.6}$$

The k-L model uses the gradient diffusion approximation for the turbulent flux:

$$-\langle v'Y_H'\rangle = \frac{\mu_t}{\langle\rho\rangle N_Y}\frac{\partial\langle Y_H\rangle}{\partial y} = D^{00}_{k\text{-}L}\frac{\partial\langle Y_H\rangle}{\partial y}, \tag{5.7}$$

where $\mu_t = C_\mu\langle\rho\rangle L\sqrt{2k}$. N_Y is one of the model coefficients set by similarity constraints derived by Dimonte & Tipton (2006). Particularly, this work uses the coefficient calibration detailed in (Morgan & Greenough 2015), and the coefficients are chosen to achieve the same α as the DNS. Here, C_μ is unity and N_Y is 2.47. The k-L RANS model is solved in spatio-temporal coordinates, and the $\langle\rho\rangle$, k, and L obtained from the solution are used to compute μ_t and, consequently, $D^{00}_{k\text{-}L}$, which is purely local. For a meaningful comparison with the MFM-based model, $D^{00}_{k\text{-}L}$ is transformed to $\widehat{D^{00}_{k\text{-}L}}$ according to the self-similar coordinate $\xi = \frac{y}{h_{k\text{-}L}}$, where $h_{k\text{-}L} = \alpha^*_{k\text{-}L} Ag(t - t^*_{k\text{-}L})^2$. It must be noted that the h fitting coefficients α^* and t^* are not the same between the DNS and k-L solutions. In this work, $\alpha^*_{\text{DNS}} = 0.046$, $t^*_{\text{DNS}} = -1600\ s$, $\alpha^*_{k\text{-}L} = 0.04$, and $t^*_{k\text{-}L} = 1250\ s$ ($t^*_{k\text{-}L}$ is positive due to the relaxation time to the self-similar profiles in the beginning of the k-L simulation).

Figure 15a shows the mean concentration profiles computed using each of the two models. As expected, the MFM-based leading-order model performs poorly, not capturing the slope of the DNS profile, since that model only uses the leading-order eddy diffusivity moment and incorporates no information about nonlocality of the eddy diffusivity. The k-L model exhibits divergence from DNS at the outer edges of the mixing layer, since it is designed to predict a

linear $\langle Y_H \rangle$ profile. However, it does capture the slope of the DNS profile, despite it also using a leading-order closure. In addition, it is observed in figure 15b that the MFM-measured $\widehat{D^{00}_{\text{MFM}}}$ is significantly lower in magnitude than $\widehat{D^{00}_{k\text{-}L}}$. Here, MFM reveals that the k-L model is using an incorrect model form, since the D^{00} it is using does not match the MFM measurement. In fact, the k-L model is using this higher-magnitude coefficient in order to compensate for the error in model form and achieve a linear mean concentration profile with a slope that matches DNS. Despite this compensation, the k-L model still disagrees with DNS results at the outer edges of the mixing layer, which are important to capturing the average reaction rate in reacting flows like in ICF. A more accurate RANS model would more closely match the eddy diffusivity moments measured by MFM. As results will show shortly, the gap between the leading-order MFM-based model $\langle Y_H \rangle$ and the DNS measurement would be bridged by inclusion of higher-order moments, which would introduce information about the nonlocality of the eddy diffusivity.

5.3. *Assessment of nonlocal operator forms*

In this section, two RANS operator forms using information about the nonlocality of the eddy diffusivity are presented. These are the explicit and implicit operator forms; the former is a truncation of the turbulent scalar flux expansion 3.6, and the latter will be presented shortly. It must be stressed that the intention of the following studies is not to propose a new RANS model. Ultimately, a RANS model should not depend on direct MFM measurements that can only be retrieved from impractically many DNS. Instead, these studies are performed to further assess the importance of each of the eddy diffusivity moments, determine which combinations of moments best enhance the performance of a RANS model, and examine the differences between the explicit and implicit operator forms. The aim of these studies is to inform development of more predictive RANS models for RTI, not to suggest that these are the exact models that should be used.

In addition, D^{20} will not be included in the following studies. This is mainly due to the high statistical error in the measurement that makes it difficult to ascertain whether errors in the results are due to this statistical error or solely the addition of the moment to the model. From the comparison of terms in §5.2.1, it is expected that D^{20} is not as important as D^{10} and D^{01} to include in a RANS model. This should be tested in future work when a more statistically-converged measurement is achieved for D^{20}, ideally in a 3D analysis.

5.3.1. *Explicit operator form*

The explicit operator form is a truncation of the expansion of the turbulent scalar flux, as defined in equation 3.6. Hamba (1995) and Hamba (2004) have examined this form in the context of shear flows. Transformation of this expansion to self-similar coordinates and substitution into 3.3 results in

$$-2\eta\frac{d\langle Y_H\rangle}{d\eta} = \frac{d}{d\eta}\left[\left(\widehat{D^{00}}-\widehat{D^{01}}\right)\frac{d\langle Y_H\rangle}{d\eta} + \left(-\eta\widehat{D^{01}} + \widehat{D^{10}}\right)\frac{d^2\langle Y_H\rangle}{d\eta^2} + \widehat{D^{20}}\frac{d^3\langle Y_H\rangle}{d\eta^3} + \ldots\right], \quad (5.8)$$

which can be solved numerically for $\langle Y_H \rangle$. The $\widehat{D^{mn}}$ used in the numerical solve are the smoothed, normalized moments. To determine which eddy diffusivity moments are important in constructing RANS models for RTI, different combinations of $\widehat{D^{mn}}$ terms are kept in equation 5.8, and the results are compared to DNS. In the numerical solve, equation 5.8 is discretized on a staggered mesh, and derivatives are computed using central finite differences. A matrix-vector equation is assembled and solved for $\langle Y_H \rangle$ with Dirichlet boundary conditions.

Figure 16 shows the turbulent scalar fluxes computed using the explicit operator form, and figure 17 shows the corresponding mean concentration profiles. Again, it is apparent that the leading-order moment is not enough to capture the turbulent scalar flux. The combination using

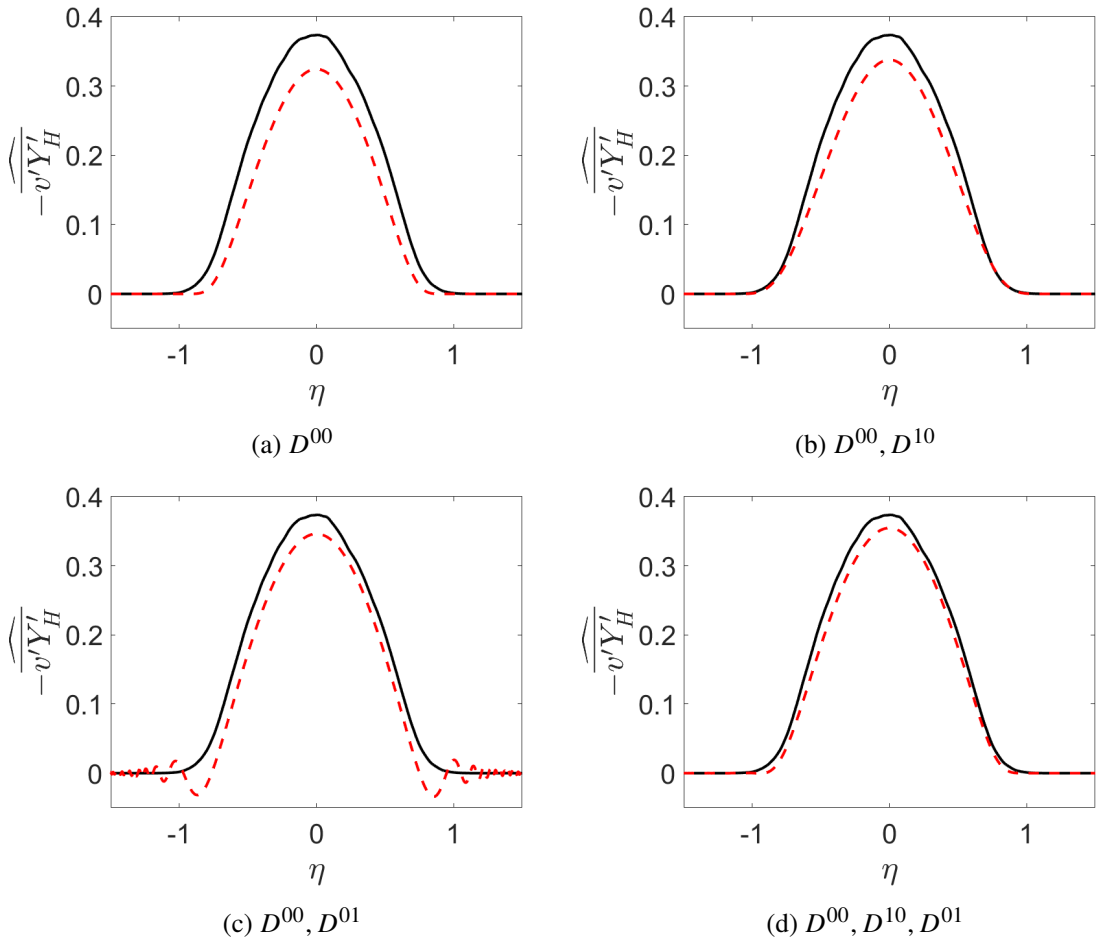

(a) D^{00} (b) D^{00}, D^{10}

(c) D^{00}, D^{01} (d) D^{00}, D^{10}, D^{01}

Figure 16: Turbulent scalar flux predictions using the explicit operator form. Captions of each plot list moments used in the model.

D^{00}, D^{10}, and D^{01}—the moments deemed most important in §5.2.1—gives the best match to the DNS measurement.

It is particularly remarkable that a converged turbulent scalar flux can be obtained using D^{00}, D^{10}, and D^{01}. As mentioned previously, it is known that equation 3.6 may not converge. That is, the expansion must be taken to infinite terms to remove error; truncating the expansion can result in significant error. This is analogous to a Kramers-Moyal expansion, which cannot be approximated adequately by more than two terms, after which it requires infinite terms for convergence (Pawula 1967; Mauri 1991). To understand how adding terms to equation 3.6 can result in greater error, one can consider the eddy diffusivity kernel associated with each term. The leading-order moment is associated with a delta function kernel, as it is purely local. However, when equation 3.4 is replaced by equation 3.6, an integral operator is replaced with a high-order differential operator. This means that the nonlocal effects are approximated by derivatives of delta functions; see Liu *et al.* (2023) for more details. It has been shown that, in general, the eddy diffusivity kernel is not a superposition of finite delta functions, as it is smooth (Mani & Park 2021; Liu *et al.* 2023). Therefore, truncation of the expansion does not match the shape of the eddy diffusivity kernel, leading to errors in prediction of the turbulent scalar flux. While the D^{00}, D^{10}, and D^{01} combination did not diverge, adding D^{20} does lead to divergent results for these reasons, so this combination is not presented here.

Another issue with the explicit operator form is its numerical implementation. In spatio-

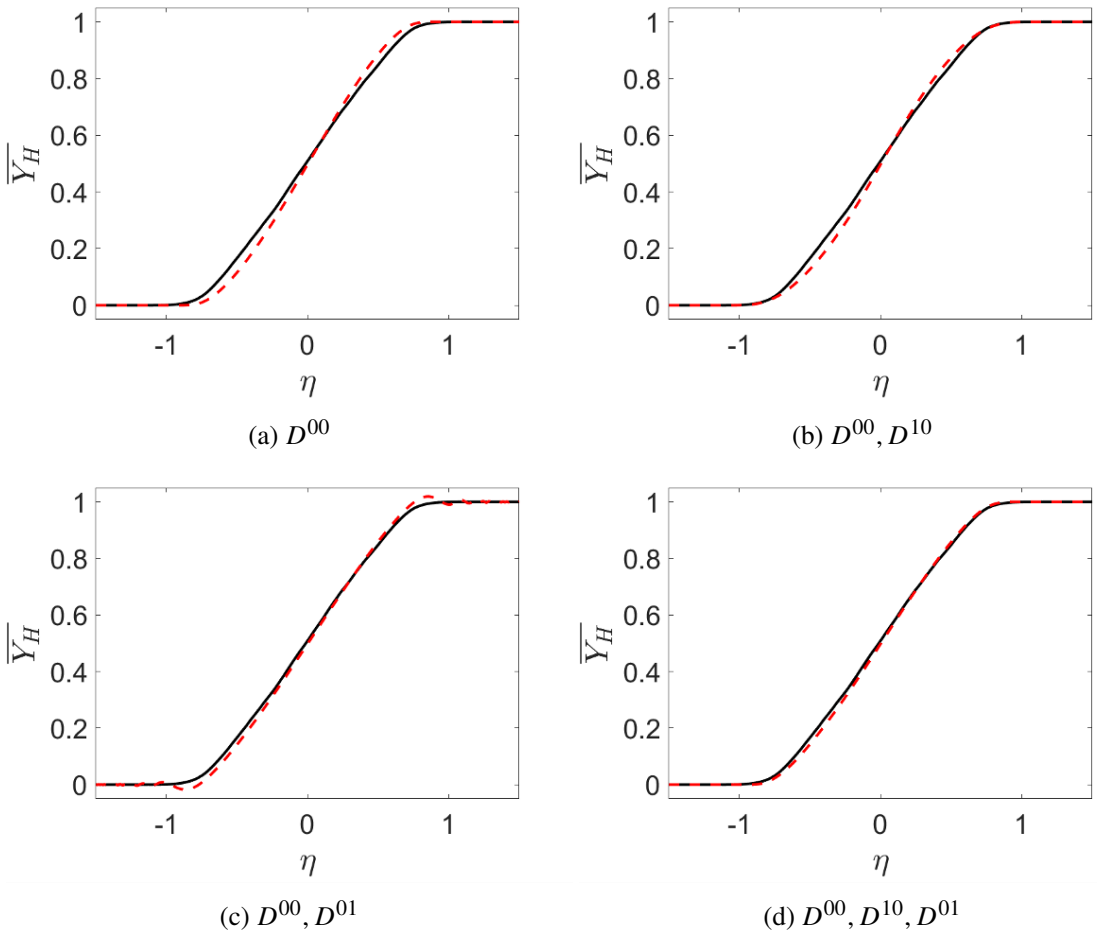

(a) D^{00} (b) D^{00}, D^{10}

(c) D^{00}, D^{01} (d) D^{00}, D^{10}, D^{01}

Figure 17: Mean concentration profile predictions using the explicit operator form. Captions of each plot list moments used in the model.

temporal space, some terms associated with higher-order moments involve mixed derivatives (e.g., the term $D^{01}\frac{\partial^2}{\partial t \partial y}$), which would undergo another spatial gradient when substituted into equation 3.3. Such terms are difficult to handle numerically. In this work, the model is implemented in the more convenient self-similar space, but, ultimately, a spatio-temporal model would be developed, as it is more practical. It is thus pertinent to work towards a better method to incorporate nonlocal information in a RANS model that does not encounter the Kramers-Moyal-like convergence issue and is easier to implement.

5.3.2. *Implicit operator form and the Matched Moment Inverse (MMI)*

In this section, an implicit operator form is introduced as a solution to both the increasing error when adding terms from the turbulent scalar flux expansion and implementation challenges associated with the explicit operator form. Recall that the explicit operator form fails to match the shape of the eddy diffusivity kernel without infinite terms of the turbulent scalar flux expansion. In this implicit operator form, the aim is to match the shape of the eddy diffusivity kernel, instead of using the truncated expansion for the turbulent scalar flux. Using the four moments that have been measured, this model form is

$$\left[1 + a^{01}\frac{\partial}{\partial t} + a^{10}\frac{\partial}{\partial y} + a^{20}\frac{\partial^2}{\partial y^2} + \ldots\right](-\langle v' Y_H' \rangle) = a^{00}\frac{\partial \langle Y_H \rangle}{\partial y}, \tag{5.9}$$

where $a^{mn}(y,t)$ are model coefficients fitted corresponding to each of the eddy diffusivity moments D^{mn} measured using MFM. The bracketed operator on the left hand side is the Matched Moment Inverse (MMI) operator. The way this model form is designed to match the eddy diffusivity kernel shape is detailed in Liu *et al.* (2023). In addition, this form is significantly easier to implement numerically in spatio-temporal space, since it can be directly time-integrated using explicit methods. In this way, it is also easy to add more terms with higher-order moments, as it simply requires extension of the operator.

In self-similar coordinates, this becomes

$$\left[1+\widehat{a^{01}}\left(1-2\eta\frac{d}{d\eta}\right)+\widehat{a^{10}}\frac{d}{d\eta}+\widehat{a^{20}}\frac{d^2}{d\eta^2}+\dots\right](-\widehat{\langle v'Y'_H\rangle})=\widehat{a^{00}}\frac{d\langle Y_H\rangle}{d\eta}, \tag{5.10}$$

where it is found through self-similar analysis that

$$\widehat{a^{00}}=\frac{1}{\alpha^{*2}A^2g^2(t-t^*)^3}a^{00}, \tag{5.11}$$

$$\widehat{a^{01}}=\frac{1}{t-t^*}a^{01}, \tag{5.12}$$

$$\widehat{a^{10}}=\frac{1}{\alpha^*Ag(t-t^*)^2}a^{10}, \tag{5.13}$$

$$\widehat{a^{20}}=\frac{1}{\alpha^{*2}A^2g^2(t-t^*)^4}a^{20}. \tag{5.14}$$

The coefficients are determined through a process illustrated as follows in spatio-temporal coordinates for simplicity. If one wants to construct a model in the form of equation 5.9, four equations must be formulated to determine the four coefficients. This is done by using measurements from the four simulations used to determine the four moments D^{00}, D^{10}, D^{01}, and D^{20}. For example, the first equation results from substitution of F^{00} for $-\langle v'Y'_H\rangle$ and the associated desired $\frac{\partial\langle Y_H\rangle}{\partial y}$; the remaining three equations follow, using the other three moments:

$$\left[1+a^{10}\frac{\partial}{\partial y}+a^{01}\frac{\partial}{\partial t}+a^{20}\frac{\partial^2}{\partial y^2}\right]F^{00}=a^{00}, \tag{5.15}$$

$$\left[1+a^{10}\frac{\partial}{\partial y}+a^{01}\frac{\partial}{\partial t}+a^{20}\frac{\partial^2}{\partial y^2}\right]F^{10}=a^{00}\left(y-\frac{1}{2}\right), \tag{5.16}$$

$$\left[1+a^{10}\frac{\partial}{\partial y}+a^{01}\frac{\partial}{\partial t}+a^{20}\frac{\partial^2}{\partial y^2}\right]F^{01}=a^{00}t, \tag{5.17}$$

$$\left[1+a^{10}\frac{\partial}{\partial y}+a^{01}\frac{\partial}{\partial t}+a^{20}\frac{\partial^2}{\partial y^2}\right]F^{20}=a^{00}\frac{1}{2}\left(y-\frac{1}{2}\right)^2. \tag{5.18}$$

This system of equations is then rearranged into a matrix equation $M_{\mathrm{MMI}}\mathbf{a}=\mathbf{b}$, which is solved for the coefficients in vector $\mathbf{a}=(a^{00},a^{10},a^{01},a^{20})^T$. Note that this matrix equation is constructed over every point in space and time, so $\mathbf{a}=\mathbf{a}(y,t)$. In this work, analysis is done in self-similar coordinates, in which $\mathbf{a}=\mathbf{a}(\eta)$. If one wishes to construct a model with different moments, the MMI operator and equations must be modified accordingly. For example, a model using only D^{00} and D^{10} would have an MMI operator of the form $1+a_{10}\frac{\partial}{\partial y}$ and use only the first two equations (with the a^{01} and a^{20} terms removed). Thus, models using different combinations of moments would use different MMI coefficients a^{mn}.

To summarize, for this implicit operator form, the following system of equations is solved in

self-similar coordinates:

$$\mathcal{L}_{\text{MMI}}\left\{-\widehat{\langle v'Y'_H\rangle}\right\} = \widehat{a^{00}}\frac{d\langle Y_H\rangle}{d\eta}, \tag{5.19}$$

$$\frac{d}{d\eta}\left(-\widehat{\langle v'Y'_H\rangle}\right) = -2\eta\frac{d\langle Y_H\rangle}{d\eta}, \tag{5.20}$$

where $\mathcal{L}_{\text{MMI}}$ is the MMI operator constructed using some combination of moments, such as in equation 5.10. Numerically, the following system is solved:

$$P(-\widehat{\langle v'Y'_H\rangle}) = \widehat{a^{00}}\mathcal{D}_\eta\langle Y_H\rangle, \tag{5.21}$$

$$\mathcal{D}_\eta\left(-\widehat{\langle v'Y'_H\rangle}\right) = -2\eta\mathcal{D}_\eta\langle Y_H\rangle, \tag{5.22}$$

where P is the matrix representing the numerical MMI operator, and $\mathcal{D}_\eta$ is the matrix representing the numerical derivative with respect to η. This can be rewritten as a block matrix-vector multiplication:

$$M\mathbf{x} = \begin{bmatrix} P & -\widehat{a^{00}}\mathcal{D}_\eta \\ \mathcal{D}_\eta & 2\eta\mathcal{D}_\eta \end{bmatrix}\begin{bmatrix} -\widehat{\langle v'Y'_H\rangle} \\ \langle Y_H\rangle \end{bmatrix} = \mathbf{b}, \tag{5.23}$$

where $\mathbf{b}$ is a vector representing the right-hand side of equations 5.22, with the proper boundary conditions enforced. In this study, zero gradient boundary conditions are used for the turbulent scalar flux, and Dirichlet boundary conditions are used for the mean concentration. The system is solved using finite differences on a staggered mesh.

Presented in this work are the determinants of the MMI matrix and resulting a_{mn} for two different combinations of moments. Figure 18 shows that with the combination of D^{00}, D^{10}, and D^{01}, the determinant of the MMI matrix is positive for all η, so a_{mn} are all well-behaved. This is indicative of good model form. On the other hand, figure 19 shows that with the combination of D^{00} and D^{01}, the determinant of the MMI matrix crosses zero, so a_{mn} contain singularities which effect poor RANS predictions (observable in plots presented later). Singular matrices arising in the MMI solve for a certain form of the implicit operator form may indicate that form is poor, in the sense that the combination of moments does not make a good RANS model. Since MMI appears to be sensitive to the information it takes in to determine the implicit operator coefficients, one must take special care and choose a model form that avoids this issue. It is found that MMI determinant zero-crossings do not occur for any of the moment combinations tested in this work other than the D^{00} and D^{01} combination, but it may happen with combinations of other higher-order moments not measured here.

Turbulent scalar fluxes computed using the implicit operator form are shown in figure 20. The implicit operator form's turbulent scalar flux prediction using just D^{00} is identical to that of the explicit operator form, by construction. It is apparent that adding either D^{10} or D^{01} alone is insufficient. As noted earlier, adding D^{01} leads to a particularly poor prediction due to singular MMI matrices at some η. The best match to DNS is attained using the combination of D^{00}, D^{10}, and D^{01}. In fact, it is evident that the implicit operator form using D^{00}, D^{10}, and D^{01} predicts the turbulent scalar flux more accurately than the explicit operator form using the same moments. This is because the implicit operator form is designed to match the shape of the eddy diffusivity kernel, and the explicit operator form may not be accomplishing this.

These trends in the explicit and implicit operator forms can be observed again in the predictions of the mean concentration profile, shown in figure 21. Particularly, the implicit operator form using D^{00}, D^{10}, and D^{01} gives a very good prediction of the mean concentration that nearly overlaps the DNS measurement. For a clearer comparison of the explicit and implicit operator forms using these moments, figure 22 shows the derivatives of the DNS- and model-computed $\langle Y_H\rangle$. The implicit operator form predicts a magnitude and shape closer to the DNS measurement

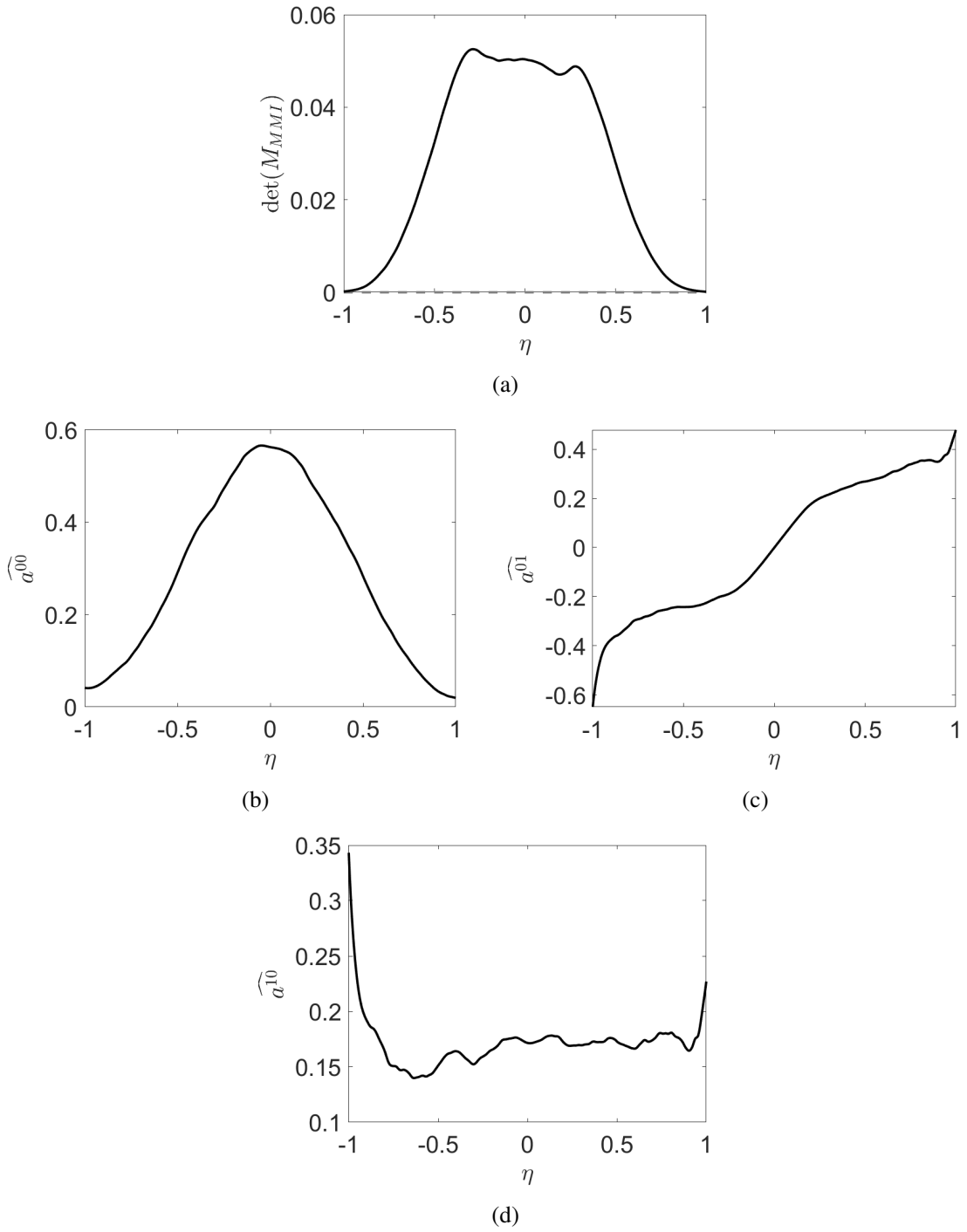

Figure 18: (a) Determinant of M_{MMI} over η and (b, c, d) MMI coefficients $\widehat{a^{mn}}$ over η for the implicit operator form using D^{00}, D^{10}, and D^{01}.

than the explicit operator form does. In particular, the implicit operator form captures the shape of the tails much better than the explicit operator form.

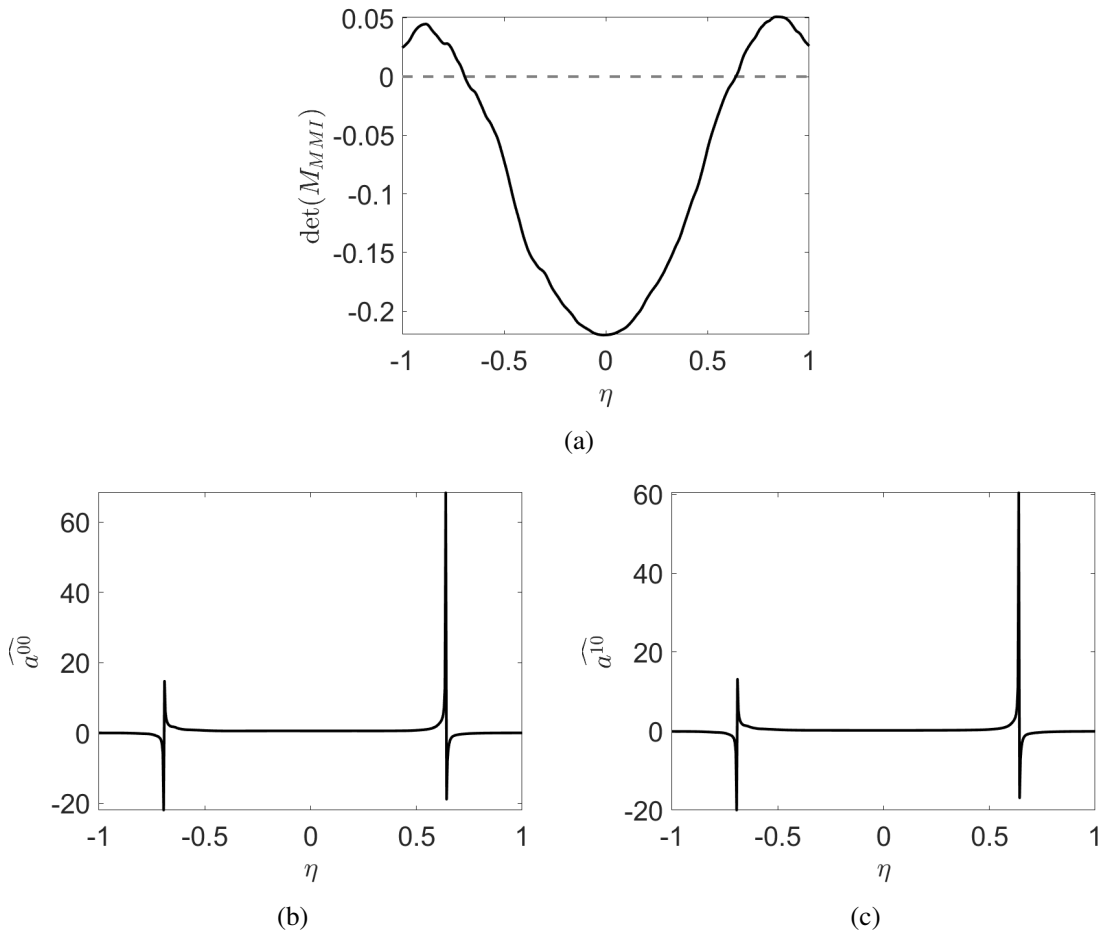

Figure 19: (a) Determinant of M_{MMI} over η and (b, c) MMI coefficients $\widehat{a^{mn}}$ over η for the implicit operator form using D^{00} and D^{01}. M_{MMI} is singular at the η at which its determinant crosses zero.

6. Conclusion

In this assessment, it is determined that nonlocality must be considered in developing more predictive models for RTI. The studies presented in this work are facilitated using MFM, a numerical tool for precisely measuring closure operators. Four of the eddy diffusivity moments of RTI (D^{00}, D^{10}, D^{01}, and D^{20}) are measured, and it is demonstrated that the higher-order moments, which contain information about the nonlocality of the eddy diffusivity kernel, should not be neglected when constructing models for RTI.

Specifically, it is determined that D^{00}, D^{10}, and D^{01} are the most important moments for constructing a model for RTI. Two methods for constructing RANS models using these moments are presented. First, an explicit operator form, based on a Kramers-Moyal-like expansion derived by taking the Taylor series expansion of the scalar gradient in the generalized eddy diffusivity, is described and tested. While incorporation of higher-order moments in the explicit operator form results in more accurate predictions than a leading-order model, there exist several issues. One problem is that the expansion used for the explicit operator form may not converge, so addition of higher-order moments leads to less accurate predictions. Another problem is that the explicit operator form is difficult to implement numerically.

Thus, an implicit operator form is presented to address these issues with the explicit operator form. Since an implicit operator form involves an invertible matrix operator, it is easier to implement than an explicit operator form. In addition, the proposed implicit operator form is

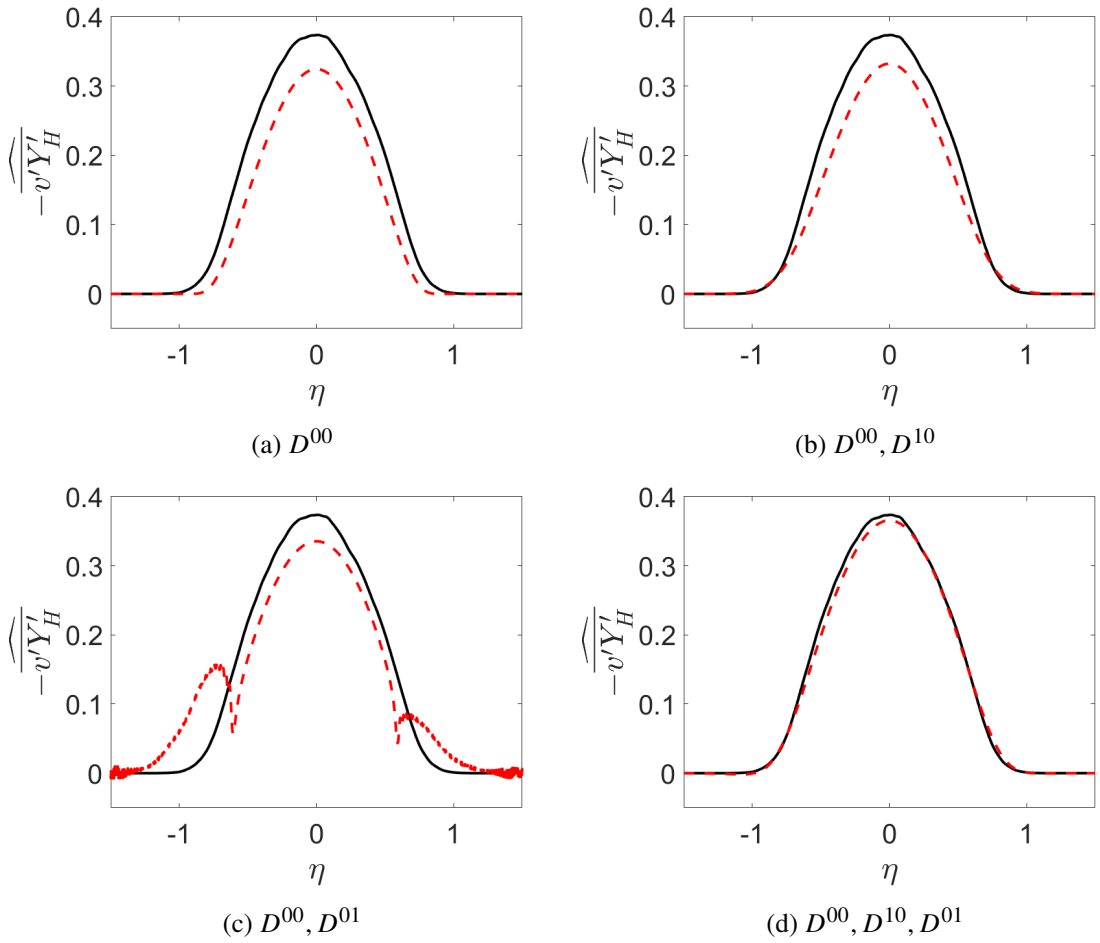

(a) D^{00} (b) D^{00}, D^{10}

(c) D^{00}, D^{01} (d) D^{00}, D^{10}, D^{01}

Figure 20: Turbulent scalar flux predictions using the implicit operator form. Captions of each plot list moments of eddy diffusivity used in the model.

designed to match the shape of the eddy diffusivity kernel via the MMI operator, in contrast to the explicit operator form, which truncates a non-converging Kramer-Moyal expansion. It is shown that the implicit operator form exhibits a marked improvement in predictions over the explicit operator form.

Incorporation of nonlocality into RANS models via these operator forms comes with several challenges. For one, development of any new model must consider scalar realizability. While this is not thoroughly explored in this work, since an actual model is not yet proposed, one approach to preserve realizability is suggested by Braun & Gore (2021), where the turbulent scalar flux is rewritten as an advection-like term and added to the original advection term in order to enforce physical mean component mass fractions; a conservative numerical scheme maintains realizability. Further, the new model must be tested on more complex RTI for it to be useful in practical settings such as ICF. This includes assessment of the model for 3D, finite Atwood, and compressible (Richtmeyer-Meshkov) flows. The model should be tested in the same validation cases as other models for RTI, such as the tilted rig (Denissen *et al.* 2014) and gravity reversal (Banerjee *et al.* 2010). Based on these evaluations, which may also involve new MFM measurements where the method is extended to more complex flow regimes, the new model can be amended, as is the usual process of turbulence model development. This is left for future work, when a new model is developed based on the findings presented here.

One obstacle encountered in these studies is the inherent statistical error in the DNS com-

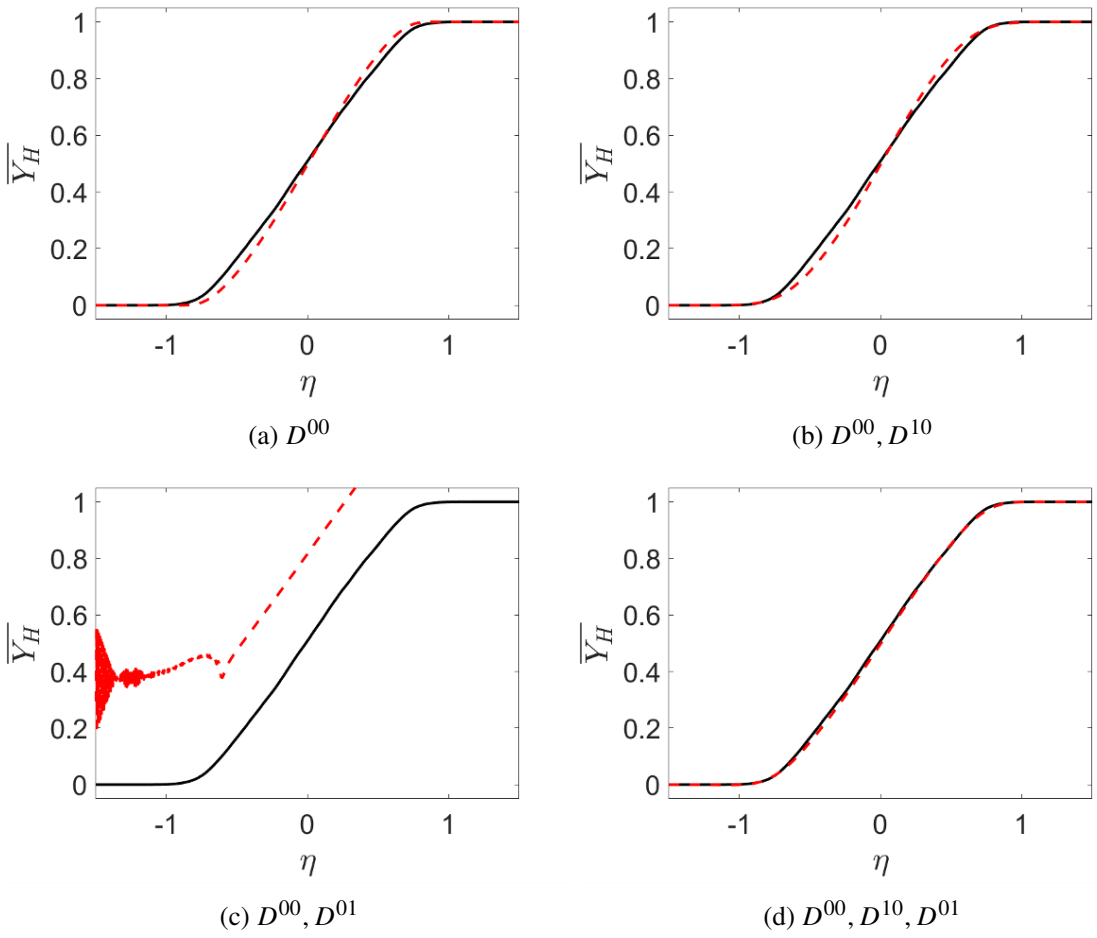

(a) D^{00} (b) D^{00}, D^{10}

(c) D^{00}, D^{01} (d) D^{00}, D^{10}, D^{01}

Figure 21: Mean concentration profile predictions using the implicit operator form. Captions of each plot list moments of eddy diffusivity used in the model.

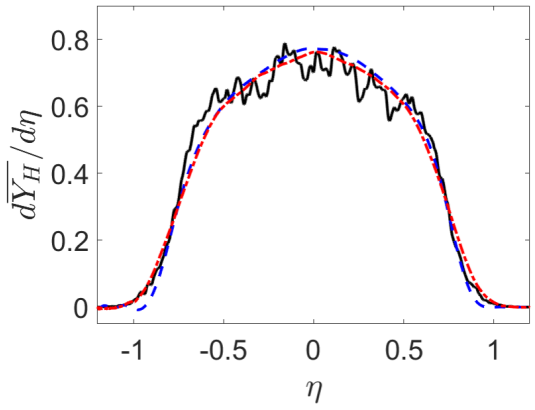

Figure 22: Derivatives of $\langle Y_H \rangle$ computed using DNS (solid black), an explicit operator form (dashed blue), and an implicit operator form (dash-dotted red).

putations. The higher-order moments particularly contain high statistical error due to buildup of error from the lower-order moments on which they depend. Because of this, it is admittedly difficult to draw definite conclusions about the effect of higher-order moments beyond the first-order moments. That is, due to the statistical error, it is currently unclear if inclusion of moments beyond first-order in a RANS model would significantly improve its predictions, or if just the first-order temporal and spatial moments along with the leading-order moment are sufficient. This motivates development of a technique to accelerate the statistical convergence of these higher-order moments. Such a method could also be used to study the effect of other higher-order moments that were not measured in this present work, since they would have suffered from high statistical error with the current method.

It must be stressed that the results in this work are for 2D RTI and should not be directly applied to 3D RTI. As noted previously, the third spatial dimension significantly impacts the turbulent physics of RTI. In particular, 3D RTI has a lower growth rate than 2D, so lower magnitudes of the eddy diffusivity moments are expected in 3D. Despite the quantitative difference in physics between 2D and 3D, they are qualitatively similar in the RANS space, so trends in the shapes of the eddy diffusivity moments are expected to persist in 3D. In other words, the form of the turbulent scalar flux closure in 3D is expected to be the same as in 2D, but the coefficients would be different. These expected trends are yet to be confirmed, and future work should involve applying MFM to 3D RTI.

Through this work, an understanding of nonlocality in 2D RTI has been developed. It has been shown that incorporation of information about the nonlocality of the eddy diffusivity may greatly improve the accuracy of a RANS model. This work demonstrates this by testing operators using MFM measurements of the nonlocal eddy diffusivity. In practice, a RANS model for RTI would not have to rely on these MFM measurements directly; one would not have to perform many MFM simulations to construct a model. In other words, MFM should be seen as a diagnostic tool rather than the means for building the actual model. The ultimate goal is to develop an improved, more predictive model for RTI by incorporating nonlocal information, which the present work has demonstrated to be significant for accurate prediction of mean scalar transport in 2D RTI.

Acknowledgements. This work was performed under the auspices of the US Department of Energy by Lawrence Livermore National Laboratory under Contract No. DE-AC52-07NA27344. D.L. was additionally supported by the Charles H. Kruger Stanford Graduate Fellowship. J.L. was additionally supported by the Burt and Deedee McMurtry Stanford Graduate Fellowship.

Declaration of Interests. The authors report no conflict of interest.

Appendix A. Nondimensionalizations

To determine the nondimensionalizations in equations 3.24 - 3.28, a self-similarity analysis is performed. The following self-similarity coordinate is used:

$$\eta = \frac{y}{h_{\text{fit}}(t)} = \frac{y}{\alpha^* A g \, (t - t^*)^2}. \tag{A 1}$$

To perform transformations to this self-similar space, all derivatives are written in terms of η:

$$\frac{\partial}{\partial t} = -\frac{2\eta}{t - t^*} \frac{d}{d\eta}, \tag{A 2}$$

$$\frac{\partial}{\partial y} = \frac{1}{\alpha^* A g \, (t - t^*)^2} \frac{d}{d\eta}, \tag{A 3}$$

$$\frac{\partial^2}{\partial t \partial y} = -\frac{2}{\alpha^* A g \, (t - t^*)^3} \left(\frac{\partial}{d\eta} + \eta \frac{d^2}{d\eta^2} \right). \tag{A 4}$$

To nondimensionalize the eddy diffusivity moments, equation 3.6 is substituted into equation 3.3:

$$\frac{\partial\langle Y_H\rangle}{\partial t} = \frac{\partial}{\partial y}\left(D^{00}\frac{\partial\langle Y_H\rangle}{\partial y} + D^{10}\frac{\partial^2\langle Y_H\rangle}{\partial y^2} + D^{01}\frac{\partial^2\langle Y_H\rangle}{\partial t\partial y} + D^{20}\frac{\partial^3\langle Y_H\rangle}{\partial y^3} + \dots\right). \tag{A 5}$$

The equation is then transformed to self-similar space:

$$\begin{aligned}-\frac{2\eta}{t-t^*}\frac{d\langle Y_H\rangle}{d\eta} = \frac{1}{\alpha^* Ag\,(t-t^*)^2}\frac{d}{d\eta}\Bigg[&\frac{1}{\alpha^* Ag\,(t-t^*)^2}D^{00}\frac{d\langle Y_H\rangle}{d\eta}\\ &+\frac{1}{\alpha^{*2}A^2g^2\,(t-t^*)^4}D^{10}\frac{d^2\langle Y_H\rangle}{d\eta^2}\\ &-\frac{2}{\alpha^* Ag\,(t-t^*)^3}D^{01}\left(\frac{d\langle Y_H\rangle}{d\eta}+\eta\frac{d^2\langle Y_H\rangle}{d\eta^2}\right)\\ &+\frac{1}{\alpha^{*3}A^3g^3\,(t-t^*)^6}D^{20}\frac{d^3\langle Y_H\rangle}{d\eta^3}\dots\Bigg].\end{aligned} \tag{A 6}$$

Rearranging,

$$\begin{aligned}-2\eta\frac{d\langle Y_H\rangle}{d\eta} = \frac{d}{d\eta}\Bigg[&\frac{1}{\alpha^{*2}A^2g^2\,(t-t^*)^3}D^{00}\frac{d\langle Y_H\rangle}{d\eta}\\ &+\frac{1}{\alpha^{*3}A^3g^3\,(t-t^*)^5}D^{10}\frac{d^2\langle Y_H\rangle}{d\eta^2}\\ &-\frac{2}{\alpha^{*2}A^2g^2\,(t-t^*)^4}D^{01}\left(\frac{d\langle Y_H\rangle}{d\eta}+\eta\frac{d^2\langle Y_H\rangle}{d\eta^2}\right)\\ &+\frac{1}{\alpha^{*4}A^4g^4\,(t-t^*)^7}D^{20}\frac{d^3\langle Y_H\rangle}{d\eta^3}\dots\Bigg].\end{aligned} \tag{A 7}$$

This reveals nondimensionalizations for the eddy diffusivity moments. The prefactors to the derivatives of $\langle Y_H\rangle$ on the right hand side are denoted as the normalized eddy diffusivity moments $\widehat{D^{mn}}$.

The turbulent scalar flux scales with the leading-order term in equation 3.6. Substitution of the nondimensionalization for D^{00} (equation 3.25) into the leading-order term in equation 3.6 and transformation to self-similar coordinates gives the scaling for the turbulent scalar flux:

$$-\langle v'Y_H'\rangle \sim \alpha^* Ag\,(t-t^*)\,\widehat{D^{00}}\frac{d\langle Y_H\rangle}{d\eta}. \tag{A 8}$$

Figure 23 shows the unscaled moments measured directly from the MFM simulations. The profiles are taken from the portion of the simulation where the flow is self-similar ($\tau \gtrapprox 17$). It is obvious that without normalizing the moments as described above there is no self-similar collapse. The moments are scaled and plotted against η in figure 24 to demonstrate the self-similar collapse. The normalized turbulent scalar flux and mean concentration profiles are shown in figures 25 and 26, also showing self-similar collapse.

REFERENCES

Banerjee, A., Gore, R. A. & Andrews, M. J. 2010 Development and validation of a turbulent-mix model for variable-density and compressible flows. *Phys. Rev. E* **82**, 046309.

Bender, J. D., Schilling, O., Raman, K. S., Managan, R. A., Olson, B. J., Copeland, S. R., Ellison, C. L., Erskine, D. J., Huntington, C. M., Morgan, B. E. & others 2021 Simulation and flow physics of a shocked and reshocked high-energy-density mixing layer. *Journal of Fluid Mechanics* **915**.

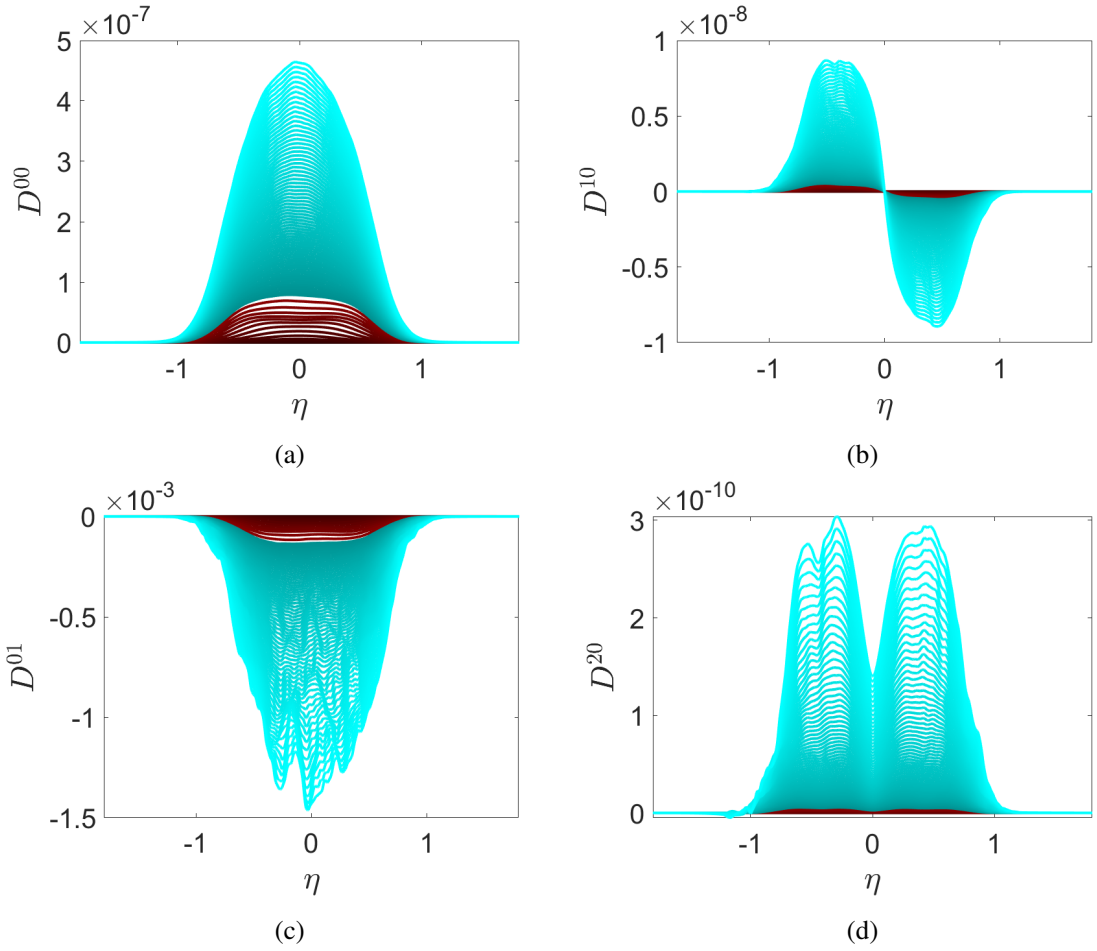

Figure 23: Unscaled moments at different times over x. Dimensions of the moments are as follows: D^{00} is m^2/s, D^{10} is m^3/s, D^{01} is m^2, and D^{20} is m^4/s. Red profiles are from early times, and cyan profiles are from late times, when the flow is self-similar. Lighter lines correspond to later times; darker lines correspond to earlier times.

Braun, N. O. & Gore, R. A. 2021 A multispecies turbulence model for the mixing and de-mixing of miscible fluids. *Journal of Turbulence* **22** (12), 784–813.

Cabot, W. 2006 Comparison of two- and three-dimensional simulations of miscible Rayleigh-Taylor instability. *Physics of Fluids* **18** (4).

Cabot, W. H. & Cook, A. W. 2006 Reynolds number effects on Rayleigh-Taylor instability with possible implications for type Ia supernovae. *Nature Physics* **2** (8), 562–568.

Casey, D. T., Smalyuk, V. A., Tipton, R. E., Pino, J. E., Grim, G. P., Remington, B. A., Rowley, D. P., Weber, S. V., Barrios, M., Benedetti, L. R. & et al. 2014 Development of the CD SYMCAP platform to study gas-shell mix in implosions at the National Ignition Facility. *Physics of Plasmas* **21** (9).

Clark, T. T., Harlow, F. H. & Moses, R. W. 1997 Comparison of a spectral turbulence model with experimental data of Rayleigh-Taylor mixing. *Tech. Rep.*. Los Alamos National Lab.(LANL), Los Alamos, NM (United States).

Clark, T. T. & Spitz, P. B. 1995 Two-point correlation equations for variable density turbulence. *Tech. Rep.*. Los Alamos National Lab.(LANL), Los Alamos, NM (United States).

Cook, A. W., Cabot, W. & Miller, P. L. 2004 The mixing transition in Rayleigh-Taylor instability. *Journal of Fluid Mechanics* **511**, 333–362.

Cook, A. W. & Dimotakis, P. E. 2001 Transition stages of Rayleigh-Taylor instability between miscible fluids. *Journal of Fluid Mechanics* **443**, 69–99.

Cook, A. W. & Zhou, Y. 2002 Energy transfer in Rayleigh-Taylor instability. *Physical Review E* **66** (2).

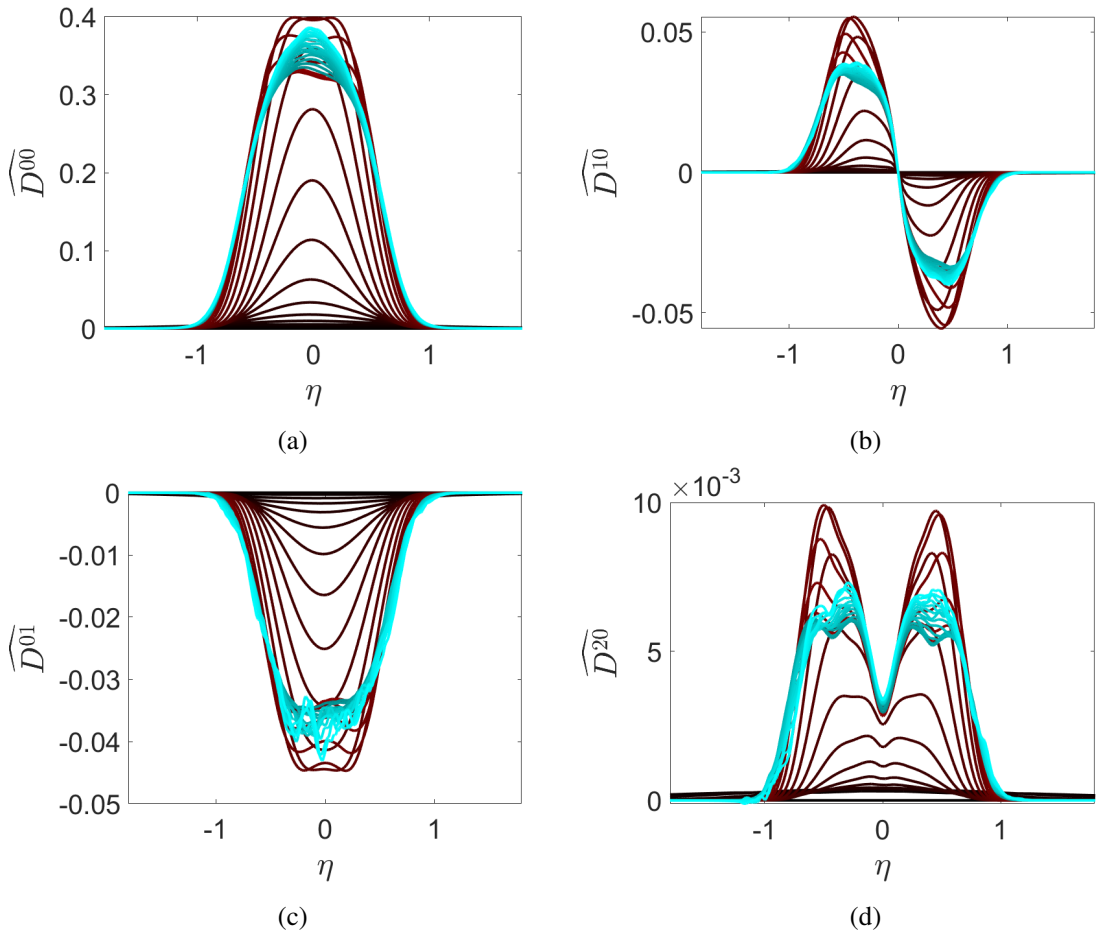

Figure 24: Self-similar collapse of moments. All $\widehat{D^{mn}}$ are dimensionless. Red profiles are from early times, and cyan profiles are from late times, when the flow is self-similar. Lighter lines correspond to later times; darker lines correspond to earlier times.

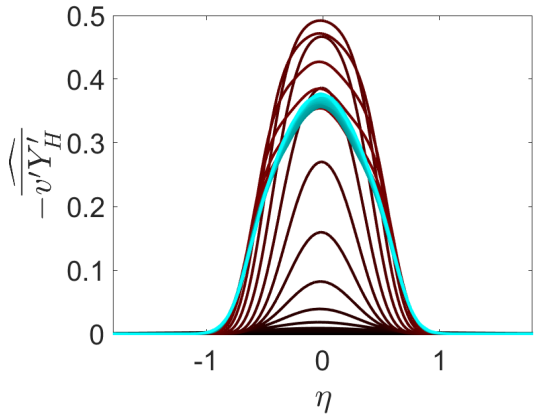

Figure 25: Self-similar collapse of turbulent scalar flux. $\widehat{-\langle v'Y'_H \rangle}$ is dimensionless. Red profiles are from early times, and cyan profiles are from late times, when the flow is self-similar. Lighter lines correspond to later times; darker lines correspond to earlier times.

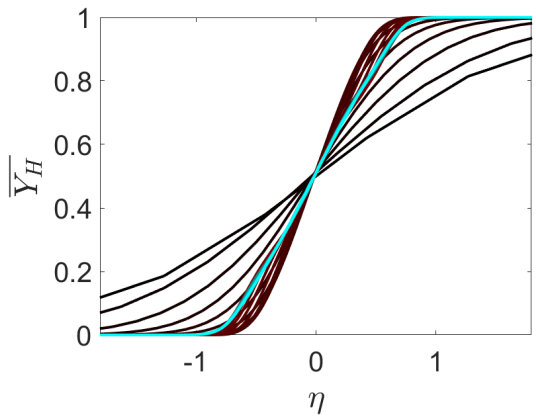

Figure 26: Mean concentration profiles at different times. Red profiles are from early times, and cyan profiles are from late times, when the flow is self-similar. Lighter lines correspond to later times; darker lines correspond to earlier times.

Darlington, R. M., McAbee, T. L. & Rodrigue, G. 2002 Large eddy simulation and ALE mesh motion in Rayleigh-Taylor instability simulation. *Computer Physics Communications* **144** (3), 261–276.

Denissen, N. A., Rollin, B., Reisner, J. M. & Andrews, M. J. 2014 The Tilted Rocket Rig: A Rayleigh-Taylor Test Case for RANS Models. *Journal of Fluids Engineering* **136** (9), 091301.

Dimonte, G. & Tipton, R. 2006 K-L turbulence model for the self-similar growth of the Rayleigh-Taylor and Richtmyer-Meshkov instabilities. *Physics of Fluids* **18** (8), 085101.

Dimotakis, P. E. 2000 The mixing transition in turbulent flows. *Journal of Fluid Mechanics* **409**, 69–98.

Gauthier, S. & Bonnet, M. 1990 A k-ε model for turbulent mixing in shock-tube flows induced by Rayleigh-Taylor instability. *Physics of Fluids A: Fluid Dynamics* **2** (9), 1685–1694.

Gull, S. F. 1975 The x-ray, optical and radio properties of young supernova remnants. *Monthly Notices of the Royal Astronomical Society* **171** (2), 263–278.

Hamba, F. 1995 An analysis of nonlocal scalar transport in the convective boundary layer using the Green's function. *Journal of Atmospheric Sciences* **52** (8), 1084–1095.

Hamba, F. 2004 Nonlocal expression for scalar flux in turbulent shear flow. *Physics of Fluids* **16** (5), 1493–1508.

Hamba, F. 2022 Analysis and modelling of non-local eddy diffusivity for turbulent scalar flux. *Journal of Fluid Mechanics* **950**, A38.

Khan, S. F., MacLaren, S. A., Salmonson, J. D., Ma, T., Kyrala, G. A., Pino, J. E., Rygg, J. R., Field, J. E., Tommasini, R., Ralph, J. E. & et al. 2016 Symmetry tuning of a near one-dimensional 2-shock platform for code validation at the National Ignition Facility. *Physics of Plasmas* **23** (4).

Kraichnan, R. H. 1987 Eddy viscosity and diffusivity: exact formulas and approximations. *Complex Systems* **1** (4-6), 805–820.

Kurien, S. & Pal, N. 2022 The local wavenumber model for computation of turbulent mixing. *Philosophical Transactions of the Royal Society A* **380** (2219), 20210076.

Launder, B. E. & Spalding, D. B. 1974 The numerical computation of turbulent flows. *Computer Methods in Applied Mechanics and Engineering* **3** (2), 269–289.

Lavacot, D. L. O.-L., Liu, J., Morgan, B. E. & Mani, A. 2022 Continuing investigations of nonlocality in Rayleigh-Taylor instability using the Macroscopic Forcing Method. *Bulletin of the American Physical Society* .

Lindl, J. 1995 Development of the indirect-drive approach to inertial confinement fusion and the target physics basis for ignition and gain. *Physics of Plasmas* **2** (11), 3933–4024.

Liu, J., Williams, H. & Mani, A. 2023 Systematic approach for modeling a nonlocal eddy diffusivity. *Physical Review Fluids* **8** (12), 124501.

Mani, A. & Park, D. 2021 Macroscopic forcing method: A tool for turbulence modeling and analysis of closures. *Phys. Rev. Fluids* **6**, 054607.

Mauri, R. 1991 Dispersion, convection, and reaction in porous media. *Physics of Fluids A: Fluid Dynamics* **3** (5), 743–756.

Morgan, B. E. 2018 Response to "Comment on 'Large-eddy simulation and unsteady RANS simulations of a shock-accelerated heavy gas cylinder'by BE Morgan, J. Greenough". *Shock Waves* **28** (6), 1301–1302.

Morgan, B. E. 2022 Large-eddy simulation and Reynolds-averaged Navier-Stokes modeling of three Rayleigh-Taylor mixing configurations with gravity reversal. *Phys. Rev. E* **106**, 025101.

Morgan, B. E. & Black, W. J. 2020 Parametric investigation of the transition to turbulence in Rayleigh-Taylor mixing. *Physica D: Nonlinear Phenomena* **402**, 132223.

Morgan, B. E. & Greenough, J. A. 2015 Large-eddy and unsteady RANS simulations of a shock-accelerated heavy gas cylinder. *Shock Waves* **26** (4), 355–383.

Morgan, B. E., Olson, B. J., Black, W. J. & McFarland, J. A. 2018 Large-eddy simulation and Reynolds-averaged Navier-Stokes modeling of a reacting Rayleigh-Taylor mixing layer in a spherical geometry. *Physical Review E* **98** (3), 033111.

Morgan, B. E., Olson, B. J., White, J. E. & McFarland, J. A. 2017 Self-similarity of a Rayleigh-Taylor mixing layer at low Atwood number with a multimode initial perturbation. *Journal of Turbulence* **18** (10), 973–999.

Mueschke, N. J., Andrews, M. J. & Schilling, O. 2006 Experimental characterization of initial conditions and spatio-temporal evolution of a small-Atwood-number Rayleigh-Taylor mixing layer. *Journal of Fluid Mechanics* **567**, 27–63.

Mueschke, N. J. & Schilling, O. 2009 Investigation of Rayleigh-Taylor turbulence and mixing using direct numerical simulation with experimentally measured initial conditions. I. Comparison to experimental data. *Physics of Fluids* **21** (1), 014106.

Olson, B. J. & Greenough, J. A. 2014 Comparison of two-and three-dimensional simulations of miscible Richtmyer-Meshkov instability with multimode initial conditions. *Physics of Fluids* **26** (10), 101702.

Pal, N., Kurien, S., Clark, T. T., Aslangil, D. & Livescu, D. 2018 Two-point spectral model for variable-density homogeneous turbulence. *Phys. Rev. Fluids* **3**, 124608.

Parish, E. J. & Duraisamy, K. 2017 Non-Markovian closure models for large eddy simulations using the Mori-Zwanzig formalism. *Phys. Rev. Fluids* **2**, 014604.

Park, D., Liu, J. & Mani, A. 2022 Direct measurement of the eddy viscosity tensor in a canonical separated flow: What is the upper bound of accuracy for local Reynolds stress models? *AIAA SCITECH 2022 Forum* .

Park, D. & Mani, A. 2023*a* Direct calculation of the eddy viscosity operator in turbulent channel flow at Re_τ=180, arXiv: 2108.10898.

Park, D. & Mani, A. 2023*b* Direct measurement of the eddy viscosity tensor in a turbulent separation bubble with sweep. In *AIAA AVIATION 2023 Forum*, p. 3268.

Pawula, R. F. 1967 Approximation of the linear Boltzmann equation by the Fokker-Planck equation. *Phys. Rev.* **162**, 186–188.

Pope, S. B. 2001 Turbulent flows. *Measurement Science and Technology* **12** (11), 2020–2021.

Ristorcelli, J. R. & Clark, T. T. 2004 Rayleigh-Taylor turbulence: self-similar analysis and direct numerical simulations. *Journal of Fluid Mechanics* **507**, 213–253.

Romanof, N. 1985 Application of the orthonormal expansion. In *Proceedings of the seventh conference on probability theory: Aug. 29-Sept. 4, 1982, Braşov, Romania*, p. 493. VSP.

Sawford, B. L. 2004 Conditional scalar mixing statistics in homogeneous isotropic turbulence. *New Journal of Physics* **6** (1), 55.

Sharp, Jr, R. W. & Barton, R. T. 1981 Hemp advection model. *Tech. Rep.*. Lawrence Livermore Laboratory.

Shende, O. B., Storan, L. & Mani, A. 2023 A model for drift velocity mediated scalar eddy diffusivity in homogeneous turbulent flows, arXiv: 2310.16372.

Shirian, Y. 2022 Application of macroscopic forcing method (MFM) for revealing turbulence closure model requirements. PhD thesis, Stanford University.

Shirian, Y. & Mani, A. 2022 Eddy diffusivity operator in homogeneous isotropic turbulence. *Phys. Rev. Fluids* **7**, L052601.

Steinkamp, M.J., Clark, T.T. & Harlow, F.H. 1999*a* Two-point description of two-fluid turbulent mixing—II. Numerical solutions and comparisons with experiments. *International Journal of Multiphase Flow* **25** (4), 639–682.

Steinkamp, M. J., Clark, T. T. & Harlow, F. H. 1999*b* Two-point description of two-fluid turbulent mixing—I. Model formulation. *International Journal of Multiphase Flow* **25** (4), 599–637.

Taylor, G. I. 1922 Diffusion by continuous movements. *Proceedings of the london mathematical society* **2** (1), 196–212.

Young, Y.-N., Tufo, H., Dubey, A. & Rosner, R. 2001 On the miscible Rayleigh-Taylor instability: two and three dimensions. *Journal of Fluid Mechanics* **447**, 377–408.

Youngs, D. L. 1994 Numerical simulation of mixing by Rayleigh-Taylor and Richtmyer–Meshkov instabilities. *Laser and Particle Beams* **12** (4), 725–750.

Zhou, Y. 2017 Rayleigh-Taylor and Richtmyer–Meshkov instability induced flow, turbulence, and mixing. ii. *Physics Reports* **723-725**, 1–160, Rayleigh-Taylor and Richtmyer–Meshkov instability induced flow, turbulence, and mixing. II.

New techniques for improved statistical convergence in quantification of eddy diffusivity moments

Dana L. O.-L. Lavacot[a,*], Jessie Liu[a,*], Brandon E. Morgan[b], Ali Mani[a]

[a] *Department of Mechanical Engineering, Stanford University, Stanford, CA 94305, USA*

[b] *Lawrence Livermore National Laboratory, Livermore, CA 94550, USA*

Abstract

While recent approaches, such as the macroscopic forcing method (MFM) of Mani and Park [1] or Green's function approach of Hamba [2, 3], can be used to compute Reynolds-averaged Navier–Stokes closure operators using forced direct numerical simulations, MFM can also be used to directly compute moments of the effective nonlocal and anisotropic eddy diffusivities. The low-order spatial and temporal moments contain limited information about the eddy diffusivity but are often sufficient for quantification and modeling of nonlocal and anisotropic effects. However, when using MFM to compute eddy diffusivity moments, the statistical convergence can be slow for higher-order moments. In this work, we demonstrate that using the same direct numerical simulation (DNS) for all forced MFM simulations improves statistical convergence of the eddy diffusivity moments. We present its implementation in conjunction with a decomposition method that handles the MFM forcing semi-analytically and allows for consistent boundary condition treatment, which we develop for both scalar and momentum transport. We demonstrate a reduction from $\mathcal{O}(1000)$ simulations to $\mathcal{O}(100)$ simulations for ensemble averaging in a two-dimensional Rayleigh–Taylor instability case study. We then demonstrate the impacts of improved convergence on modeling and quantification of the eddy diffusivity.

Keywords: RANS closure; Eddy diffusivity; Moments

1. Introduction

For many flows, direct numerical simulation (DNS) of the governing equations is computationally cost-prohibitive and only the averaged quantities, e.g., spatially- or temporally-averaged mean scalar or velocity fields, are needed. Reynolds-averaged Navier–Stokes (RANS) models are widely used in such applications. In RANS modeling, the flow variables are Reynolds decomposed into mean and fluctuating components, and closure models are needed for unclosed terms involving the product of fluctuating quantities, e.g., scalar fluxes or Reynolds stresses.

Many closure models use the Boussinesq approximation [4] which, under an assumption of scale separation and isotropy of the underlying mixing process, results in a local and isotropic eddy diffusivity for scalar transport or, analogously, eddy viscosity for momentum transport. For many

*These authors contributed equally to this work (alphabetical by last name).
Email address: dlol@stanford.edu (Dana L. O.-L. Lavacot)

complex flows, the Boussinesq approximation is invalid [5], and generally the eddy diffusivity is nonlocal and anisotropic [2, 6, 7].

Recent approaches, such as the macroscopic forcing method (MFM) of Mani and Park [1] or Green's function approach of Hamba [2, 3], can be used to compute the nonlocal and anisotropic eddy diffusivity. These eddy diffusivities (or viscosities) are exact in that substitution of these operators back into the mean scalar (or mean momentum) equations results in DNS mean quantities. Kraichnan [7] derived an exact nonlocal and anisotropic expression for the scalar flux and Reynolds stress tensor using a Green's function. Hamba [2, 3] modified the expression to be feasible for numerical implementation for scalar and momentum transport, respectively. Because this approach needs the Green's function solution at each location in the averaged space, using a separate DNS for each location, computing the nonlocal and anisotropic eddy diffusivity requires as many DNSs as degrees of freedom in the averaged space.

Mani and Park [1] developed MFM, a linear-algebra-based method for numerically obtaining closure operators. In MFM, one examines the closure operator by applying an appropriate forcing (not necessarily a Dirac delta function) to the governing equations and measures the averaged response. While MFM can obtain the exact nonlocal and anisotropic eddy diffusivity similar to the approach of Hamba [2, 3], MFM can also directly obtain spatial or temporal moments of the eddy diffusivity, using one simulation per desired moment. Liu et al. [8] showed how to use the limited information from a few low-order moments to model the eddy diffusivity. The modeled eddy diffusivity is nonlocal and matches the measured low-order moments, while the shape of its kernel approximately resembles the true kernel. Lavacot et al. [9] quantified nonlocal effects in two-dimensional Rayleigh–Taylor instability by using MFM-measured eddy diffusivity moments and showed improvement over a local model when including these low-order moments in the nonlocal model form suggested by Liu et al. [8].

In MFM, two sets of equations are solved: the donor and receiver equations. The donor equations provide flow fields needed for the solution of the receiver equations, which are macroscopically forced when probing the eddy diffusivity moments. Each moment requires its own receiver equation, and each receiver equation requires flow fields from the donor solution. For ease of implementation, it is natural to run simulations for each eddy diffusivity moment separately where each simulation solves its own donor and receiver equations. For example, to determine one moment, one could structure a simulation so that the Navier-Stokes equations with certain initial and boundary conditions would be the set of donor equations to a set of receiver equations. Then, another simulation can be run to determine another moment, which requires a different receiver but analytically identical donor as the previous simulation. These two simulations can be run independently from each other, each solving the donor separately. However, while the analytical solutions of the donors are identical, some statistical differences may arise in the donors between the two solutions. This may occur, for example, due to numerical differences between processes in the simulations. The statistical error can accumulate and ultimately lead to slow statistical convergence of the eddy diffusivity moments,

particularly in chaotic problems, where averaging is done over many realizations.

To avoid this slow convergence, an MFM simulation can instead use one donor to service multiple receiver equations. That is, the individual MFM simulations described in the previous paragraph can be combined into one simulation using one donor but solving for multiple sets of receiver equations. Using one donor then prevents statistical error from random processes and reduces the overall computational cost of MFM, since only one donor needs to be solved.

With this method, we can also utilize the decomposition introduced by Liu et al. [8] to semi-analytically treat the MFM forcing; we call this combined single donor and semi-analytical forcing approach the *decomposition MFM*. The decomposition method alleviates boundary condition issues when the MFM forcing is incompatible with the boundary conditions of the problem. Liu et al. [8] demonstrated the decomposition method for scalar transport in a steady laminar inhomogeneous flow. In this work, we extend the decomposition method to obtain spatiotemporal moments of the eddy diffusivity for general unsteady and chaotic flows as well as momentum transport. We then apply the decomposition MFM to scalar transport in Rayleigh-Taylor (RT) instability to illustrate the acceleration of statistical convergence due to use of a single donor and its compatibility with the proposed decomposition method.

In this work, we begin with scalar transport before generalizing to momentum transport. In Section 2, we define the nonlocal and anisotropic eddy diffusivity and its moments. In Section 3, we introduce MFM for directly computing the eddy diffusivity moments. In Section 4, we develop the decomposition method for general unsteady and chaotic flows. In Section 5, we generalize to momentum transport and the nonlocal and anisotropic eddy viscosity. In Section 6, as an illustrative example, we demonstrate the improved statistical convergence of the eddy diffusivity moments for 2D RT instability and discuss the modeling impacts and physical findings.

2. Problem formulation for scalar transport

The governing equation for a passive scalar is

$$\frac{\partial c}{\partial t} + \frac{\partial}{\partial x_i}\left(u_i c\right) = D_M \frac{\partial^2 c}{\partial x_i \partial x_i}, \tag{1}$$

where $c(\mathbf{x}, t)$ is a passive scalar field, $u_i(\mathbf{x}, t)$ is an incompressible velocity field, and D_M is the molecular diffusivity. The average, which we denote using $\langle\cdot\rangle$, may be defined as an ensemble average if the flow is ergodic, a temporal average if the flow is statistically stationary, and/or a spatial average if the flow is homogeneous. Substitution of the Reynolds decomposition, $c = \langle c\rangle + c'$, into the scalar transport equation in (1) and averaging gives

$$\frac{\partial \langle c\rangle}{\partial t} + \frac{\partial}{\partial x_i}\left(\langle u_i\rangle\langle c\rangle\right) = D_M \frac{\partial^2 \langle c\rangle}{\partial x_i \partial x_i} - \frac{\partial}{\partial x_i}\langle u_i' c'\rangle, \tag{2}$$

where $\langle u_i' c'\rangle$ is the unclosed turbulent scalar flux that needs to be modeled.

If 1) the length and time scales of the underlying fluctuations are much smaller than those of the mean scalar gradient, and 2) the mixing by the underlying fluctuations is isotropic, then the Boussinesq approximation [4] is valid, and the turbulent scalar flux can be modeled as

$$-\langle u_i' c' \rangle = D \frac{\partial \langle c \rangle}{\partial x_i}, \tag{3}$$

where D is a local and isotropic eddy diffusivity. Although widely-used, the Boussinesq approximation is often invalid for complex flows [5].

More generally, the turbulent scalar flux can be formulated exactly using the nonlocal and anisotropic eddy diffusivity [2, 6, 7]:

$$-\langle u_i' c' \rangle (\mathbf{x}, t) = \int \int D_{ij}(\mathbf{x}, \mathbf{x}', t, t') \left. \frac{\partial \langle c \rangle}{\partial x_j} \right|_{\mathbf{x}', t'} \mathrm{d}\mathbf{x}' \mathrm{d}t', \tag{4}$$

where $D_{ij}(\mathbf{x}, \mathbf{x}', t, t')$ is the eddy diffusivity kernel. The eddy diffusivity is nonlocal in that the kernel allows the turbulent scalar flux to depend on the mean scalar gradient at all points in space and in its time history, $\mathbf{x}'$ and t', respectively. The eddy diffusivity is anisotropic in that the second-order tensor allows the turbulent scalar flux to depend on all directions of the mean scalar gradient.

The eddy diffusivity may also be characterized by its moments, which are related to the eddy diffusivity kernel by considering the Taylor series expansion locally about $\mathbf{x}' = \mathbf{x}$ and $t' = t$ (also known as a Kramers–Moyal expansion [10]):

$$-\langle u_i' c' \rangle (\mathbf{x}, t) = \int \int D_{ij}(\mathbf{x}, \mathbf{x}', t, t') \left(\left. \frac{\partial \langle c \rangle}{\partial x_j} \right|_{\mathbf{x}, t} + \left(x_k' - x_k \right) \left. \frac{\partial^2 \langle c \rangle}{\partial x_k \partial x_j} \right|_{\mathbf{x}, t} + \cdots + \left(t' - t \right) \left. \frac{\partial^2 \langle c \rangle}{\partial t \partial x_j} \right|_{\mathbf{x}, t} + \ldots \right) \mathrm{d}\mathbf{x}' \mathrm{d}t' \tag{5}$$

Since the derivatives of $\langle c \rangle$ are no longer functions of $\mathbf{x}'$ and t', they can be moved out of the integral, and the above equation can be rearranged as

$$-\langle u_i' c' \rangle (\mathbf{x}, t) = \left[D_{ij}^{00}(\mathbf{x}, t) + D_{ijk}^{10}(\mathbf{x}, t) \frac{\partial}{\partial x_k} + \cdots + D_{ij}^{01}(\mathbf{x}, t) \frac{\partial}{\partial t} + \ldots \right] \frac{\partial \langle c \rangle}{\partial x_j}, \tag{6}$$

where the eddy diffusivity moments, $D_{ij}^{mn}(\mathbf{x}, t)$ are defined as

$$D_{ij}^{00}(\mathbf{x}, t) = \int \int D_{ij}(\mathbf{x}, \mathbf{x}', t, t') \mathrm{d}\mathbf{x}' \mathrm{d}t', \tag{7}$$

$$D_{ijk}^{10}(\mathbf{x}, t) = \int \int (x_k' - x_k) D_{ij}(\mathbf{x}, \mathbf{x}', t, t') \mathrm{d}x_k' \mathrm{d}t', \tag{8}$$

$$\vdots$$

$$D_{ij}^{01}(\mathbf{x}, t) = \int \int (t' - t) D_{ij}(\mathbf{x}, \mathbf{x}', t, t') \mathrm{d}\mathbf{x}' \mathrm{d}t', \tag{9}$$

$$\vdots$$

The superscripts denote the m-th order spatial moment and n-th order temporal moment. The leading-order term in the expansion is the zeroth-order spatiotemporal moment, D_{ij}^{00}, and is local and anisotropic. The higher-order spatiotemporal moments can be used to characterize nonlocal effects. For example, by using MFM [1] to measure the moments, Park and Mani [11] investigated nonlocality and anisotropy in turbulent channel flow and Lavacot et al. [9] investigated spatiotemporal nonlocality in Rayleigh–Taylor instability. Liu et al. [8] showed how to use the low-order eddy diffusivity moments to model the nonlocal eddy diffusivity kernel.

3. Eddy diffusivity moments using the macroscopic forcing method (MFM)

In this section, we briefly introduce MFM for computing closure operators, e.g., the nonlocal and anisotropic eddy diffusivity in Equation (4), before showing MFM for directly computing the eddy diffusivity moments in Equations (7)-(9). We discuss slow convergence in the higher-order moments due to error propagation from the lower-order moments.

In MFM, forcing is added to the scalar transport equation:

$$\frac{\partial c}{\partial t} + \frac{\partial}{\partial x_i}\left(u_i c\right) = D_M \frac{\partial^2 c}{\partial x_i \partial x_i} + s, \tag{10}$$

where s is the MFM forcing with the important macroscopic property, $s = \langle s \rangle$. As detailed in Mani and Park [1], by explicitly specifying the MFM forcing, one can arrive at the closure operator by post-processing $\langle c \rangle$. Alternatively, by using the MFM forcing to maintain a specified mean scalar, $\langle c \rangle$, one can also arrive at the closure operator using what is known as inverse MFM. For example, one can compute the nonlocal and anisotropic eddy diffusivity in (4) by specifying the mean scalar such that the gradient is a Dirac delta function at each point in the averaged space and post-processing the turbulent scalar flux. Each point requires a separate forced DNS, and thus obtaining the eddy diffusivity kernel for the entire domain requires as many DNSs as degrees of freedom in the averaged space. Due to the large number of DNSs needed, this brute force approach is computationally expensive and practically infeasible for problems with many degrees of freedom in the averaged space. The brute force application of inverse MFM with Dirac delta functions is identical to the Green's function approach of Hamba [2] as discussed in Liu et al. [8].

As an alternative to a computationally expensive brute force approach, inverse MFM can also be used to directly compute the moments of the eddy diffusivity in Equations (7)-(9) by specifying the mean scalar as polynomials [1]. The eddy diffusivity moments need just one forced DNS per moment, and a few low-order moments are often sufficient for quantification and modeling of nonlocal and anisotropic effects. Consider a simple one-dimensional (1D) example, in which averaging is taken over all directions except x_1 and there is only one component of the scalar flux, $\langle u_1' c' \rangle$. Equation (6) becomes

$$-\langle u_1' c' \rangle(x_1, t) = \left[D^{00}(x_1, t) + D^{10}(x_1, t)\frac{\partial}{\partial x_1} + D^{20}(x_1, t)\frac{\partial^2}{\partial x_1^2} + \cdots + D^{01}(x_1, t)\frac{\partial}{\partial t} + \ldots \right] \frac{\partial \langle c \rangle}{\partial x_1}, \tag{11}$$

where we have omitted the tensorial notation, D_{ij}, since here we only consider the $D = D_{11}$ component. To obtain the zeroth-order spatiotemporal moment of the eddy diffusivity, one specifies $\langle c \rangle = x_1$ using inverse MFM and solves the forced scalar transport equation in (10). At each time step, the forcing is used to maintain the specified $\langle c \rangle$ while c is free to evolve. Practically, one can first time advance the governing equation without the forcing and solve for an intermediate scalar field, and then add the forcing in a correction step to ensure the scalar field at the next time step has the requisite $\langle c \rangle$ as discussed in [1, 12]. Postprocessing of $-\langle u_1' c' \rangle$ leads to the zeroth moment:

$$-\langle u_1' c' \rangle|_{\langle c \rangle = x_1}(x_1, t) = D^{00}(x_1, t) \tag{12}$$

as shown by substitution of $\langle c \rangle = x_1$ into (11). Specifying $\langle c \rangle$ as higher-order polynomials leads to higher-order moments of the eddy diffusivity. For the first-order spatial moment, specifying $\langle c \rangle = x_1^2/2$ gives

$$-\langle u_1' c' \rangle|_{\langle c \rangle = x_1^2/2}(x_1, t) = x_1 D^{00}(x_1, t) + D^{10}(x_1, t) \tag{13}$$

as shown by substitution of $\langle c \rangle = x_1^2/2$ into (11). Post-processing the scalar flux and then subtracting out the contribution from the zeroth-order moment leads to D^{10}. Similarly, for the second-order spatial moment, specifying $\langle c \rangle = x_1^3/6$ gives

$$-\langle u_1' c' \rangle|_{\langle c \rangle = x_1^3/6}(x_1, t) = \frac{x_1^2}{2} D^{00}(x_1, t) + x_1 D^{10}(x_1, t) + D^{20}(x_1, t), \tag{14}$$

and post-processing the scalar flux and then subtracting out the contribution from the zeroth- and first-order spatial moments leads to D^{20}. For the first-order temporal moment, specifying $\langle c \rangle = x_1 t$ leads to

$$-\langle u_1' c' \rangle|_{\langle c \rangle = x_1 t}(x_1, t) = t D^{00}(x_1, t) + D^{01}(x_1, t) \tag{15}$$

as shown by substitution of $\langle c \rangle = x_1 t$ into (11). Post-processing the scalar flux and then subtracting out the contribution from the zeroth-moment leads to D^{01}.

For a general multi-dimensional problem, other components of D_{ij}^{mn} can be obtained by specifying the mean scalar in various coordinate directions and post-processing the components of the scalar flux. For example, specifying $\langle c \rangle = x_\alpha$ where $\alpha = 1, 2, \text{or } 3$ and substituting into the expansion in Equation (6) gives

$$-\langle u_i' c' \rangle(\mathbf{x}, t)|_{\langle c \rangle = x_\alpha} = D_{i\alpha}^{00}(\mathbf{x}, t). \tag{16}$$

Postprocessing the scalar flux gives the $j = \alpha$ component of the zeroth-order spatiotemporal moment of the eddy diffusivity, $D_{i\alpha}^{00}$. Similarly, for the first-order spatial moment, specifying $\langle c \rangle = x_\alpha^2/2$ leads to

$$-\langle u_i' c' \rangle(\mathbf{x}, t)|_{\langle c \rangle = x_\alpha^2/2} = x_\alpha D_{i\alpha}^{00}(\mathbf{x}, t) + D_{i\alpha\alpha}^{10}(\mathbf{x}, t), \tag{17}$$

with no summation over α implied. Postprocessing the scalar flux and then subtracting out the contribution from the zeroth-order moment leads to $D_{j\alpha\alpha}^{10}$. Cross components of the first-order spatial moment may be obtained by by specifying $\langle c \rangle = x_\alpha x_\beta$ where $\alpha, \beta = 1, 2, \text{or } 3$ and $\alpha \neq \beta$.

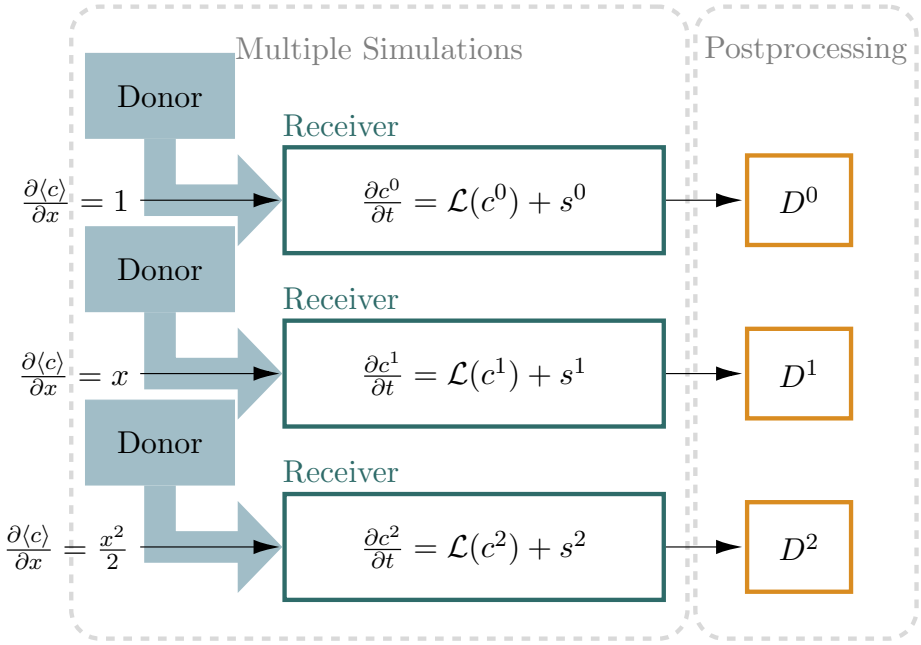

(a) Standard MFM.

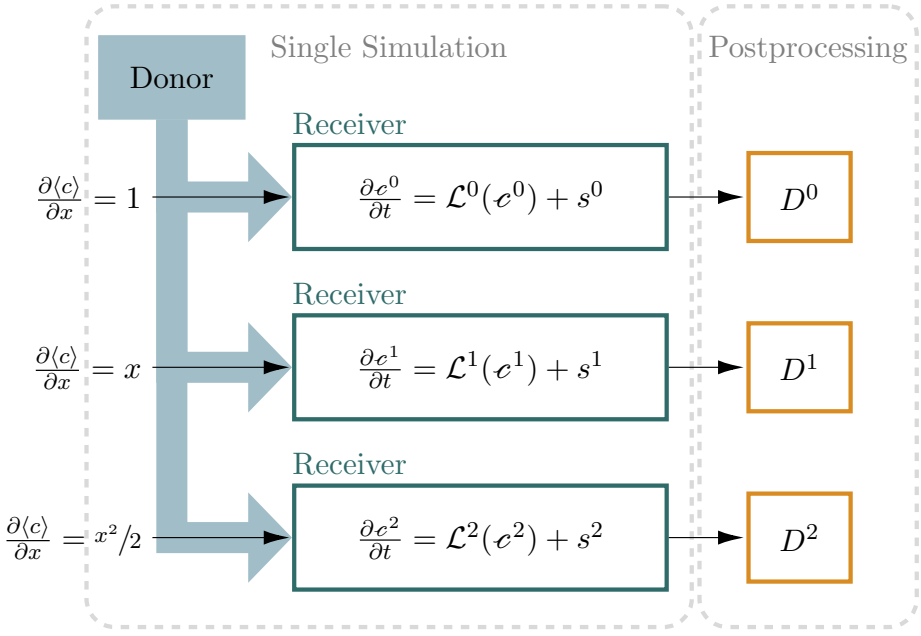

(b) Decomposition method.

Figure 1: Diagrams outlining MFM and the decomposition method in this work, presented in one dimension for simplicity. Superscripts denote variables (c^i, c^i, etc.) and operators ($\mathcal{L}^i$) belonging for the receiver equations solved to obtain D^i.

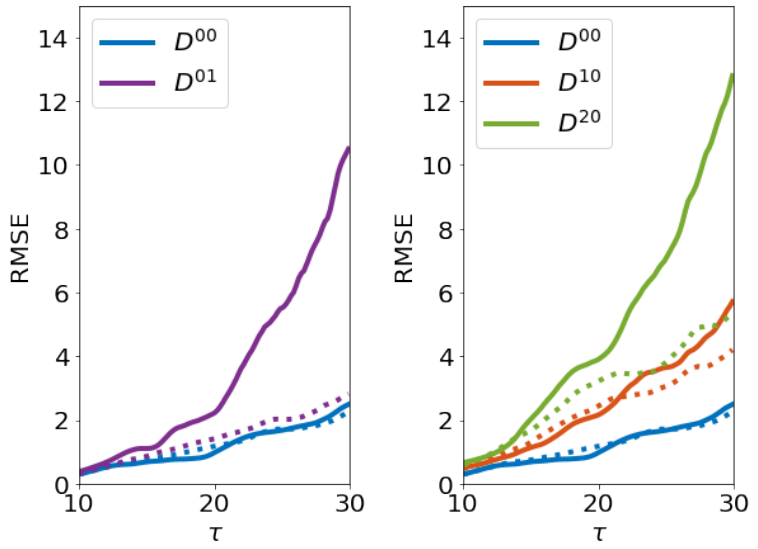

(a) Leading order and first temporal moments.

(b) Leading order and spatial moments.

Figure 2: Root mean square errors (RMSE) of standard (solid lines) and single donor (dotted lines) MFM as percent of maximum magnitude of each eddy diffusivity moment at each time. Errors are computed at 20 realizations with respect to 200 realizations for each method.

3.1. Discussion of statistical error

A natural implementation of MFM for some codes is to use separate sets of donor and receiver equations for each moment to be computed. This configuration is illustrated in Figure 1a. This approach is more computationally expensive, since the donor equations are solved multiple times, but is easier to implement, since just one set of receiver equations is one-way coupled to each donor equation. Another approach would be to run an MFM simulation using a single donor for multiple receivers, as illustrated in Figure 1b (the additional decomposition features of this proposed method will be detailed in a later section). While mathematically equivalent to using a single donor, using separate donor simulations can result in larger statistical error. Separate donor simulations, though solving for mathematically equivalent fields, may produce slightly different numerical results due to statistical differences in parallel computing. The resulting errors get amplified in space or time in higher-order moment computations, ultimately leading to slow statistical convergence. When statistical errors between donors match (i.e., a single donor is used for multiple receivers), the amplified error is removed, and statistical convergence is accelerated.

To illustrate, Figure 2 shows the statistical errors associated with the standard and single donor methods applied to the 2D RT problem. In 2D RT instability, the flow is averaged over the homogeneous x_1 direction and over multiple realizations. Details on the RT case study will be covered later in Section 6, but we present these plots here to demonstrate the differences in error between the two methods. Since computation of D^{01} involves multiplication of D^{00} (and therefore its associated statistical error) by t, we expect that at large τ, the largest difference in errors

between the two methods should be in D^{01}. This is indeed what we observe in the statistical error plots. Overall, across all higher-order moments, the standard MFM exhibits higher error than the single donor method. When a single donor is used, errors are not amplified in computation of the higher-order moments, so all errors scale similarly with time.

As further illustration, a qualitative analysis is provided in Appendix A.

4. Decomposition method

In the previous section, we demonstrated the need for using the same DNS simulation (donor) for all forced MFM simulations (receivers) to reduce statistical error. In conjunction, we now introduce a decomposition method that can be used simultaneously at no additional cost. The decomposition method treats the MFM forcing semi-analytically and was originally developed to address the issue of periodic boundary conditions in a steady laminar problem [8]. Here we extend the decomposition to general unsteady and chaotic problems and to momentum transport in Section 5.

Similar to the Green's function approach of Hamba [2], we begin by substituting the Reynolds decomposition, $c(\mathbf{x},t) = \langle c\rangle(\mathbf{x},t) + c'(\mathbf{x},t)$, into the scalar transport equation in (1) and subtracting the mean scalar transport equation to derive an equation for the scalar fluctuation, c':

$$\frac{\partial c'}{\partial t} + \frac{\partial}{\partial x_i}\left(u_i c' - \langle u_i' c'\rangle\right) - D_M \frac{\partial^2 c'}{\partial x_i \partial x_i} = -u_i' \frac{\partial \langle c\rangle}{\partial x_i}. \tag{18}$$

The general solution [2] for $c'(\mathbf{x},t)$ is

$$c'(\mathbf{x},t) = \int\int g_j(\mathbf{x},\mathbf{x}',t,t') \left.\frac{\partial \langle c\rangle}{\partial x_j}\right|_{\mathbf{x}',t'} \mathrm{d}\mathbf{x}'\mathrm{d}t', \tag{19}$$

where $g_j(\mathbf{x},\mathbf{x}',t,t')$ is the Green's function solution to

$$\frac{\partial g_j}{\partial t} + \frac{\partial}{\partial x_i}\left(u_i g_j - \langle u_i' g_j\rangle\right) - D_M \frac{\partial^2 g_j}{\partial x_i \partial x_i} = -u_j' \delta(\mathbf{x}-\mathbf{x}')\delta(t-t'). \tag{20}$$

As discussed in Liu et al. [8], the term $-\partial/\partial x_i \langle u_i' c'\rangle$ is related to the MFM forcing via

$$-\frac{\partial}{\partial x_i}\langle u_i' c'\rangle = \frac{\partial \langle c\rangle}{\partial t} + \langle u_i\rangle \frac{\partial \langle c\rangle}{\partial x_i} - D_M \frac{\partial^2 \langle c\rangle}{\partial x_i \partial x_i} - s, \tag{21}$$

and substitution of (21) into (18) leads to the forced transport equation for the scalar fluctuation:

$$\frac{\partial c'}{\partial t} + \frac{\partial}{\partial x_i}\left(u_i c'\right) - D_M \frac{\partial^2 c'}{\partial x_i \partial x_i} = s - \frac{\partial \langle c\rangle}{\partial t} - u_i \frac{\partial \langle c\rangle}{\partial x_i} + D_M \frac{\partial^2 \langle c\rangle}{\partial x_i \partial x_i}. \tag{22}$$

In this alternative formulation for inverse MFM, the forcing $s = \langle s\rangle$ is used to maintain $\langle c'\rangle = 0$. One advantage of using Equation (22) rather than Equation (10) for inverse MFM is that only the derivatives of the mean scalar appear rather than the mean scalar itself. The derivatives of the mean scalar are specified analytically and do not necessarily need a mathematically consistent mean scalar field. This point is further discussed in Liu et al. [13], where we take advantage of the

forced fluctuation equation to measure various components of the eddy viscosity tensor in turbulent channel flow independently. The other advantage is that now we can further decompose $c'(\mathbf{x},t)$. Similar to the expansion in (6), consider the Taylor series expansion of the general solution for $c'(\mathbf{x},t)$ in (19) locally about $\mathbf{x}'=\mathbf{x}$ and $t=t'$:

$$c'(\mathbf{x},t)=\left[\mathscr{c}_j^{00}(\mathbf{x},t)+\mathscr{c}_{jk}^{10}(\mathbf{x},t)\frac{\partial}{\partial x_k}+\cdots+\mathscr{c}_j^{01}(\mathbf{x},t)\frac{\partial}{\partial t}+\ldots\right]\frac{\partial\langle c\rangle}{\partial x_j}, \tag{23}$$

where

$$\mathscr{c}_j^{00}(\mathbf{x},t)=\int\int g_j(\mathbf{x},\mathbf{x}',t,t')\mathrm{d}\mathbf{x}'\mathrm{d}t', \tag{24}$$

$$\mathscr{c}_{jk}^{10}(\mathbf{x},t)=\int\int (x_k'-x_k)g_j(\mathbf{x},\mathbf{x}',t,t')\mathrm{d}x_k'\mathrm{d}t', \tag{25}$$

$$\vdots$$

$$\mathscr{c}_j^{01}(\mathbf{x},t)=\int\int (t'-t)g_j(\mathbf{x},\mathbf{x}',t,t')\mathrm{d}\mathbf{x}'\mathrm{d}t', \tag{26}$$

$$\vdots$$

By substituting this decomposition for $c'(\mathbf{x},t)$ into the forced scalar fluctuation equation in (22), we can derive governing equations for $\mathscr{c}^{mn}(\mathbf{x},t)$. As with inverse MFM, we can activate various $\mathscr{c}^{mn}(\mathbf{x},t)$ fields by specifying the mean scalar gradient. The main difference from inverse MFM as detailed in Section 3 is that the mean scalar gradient and MFM forcing are now treated semi-analytically. For example, specifying the mean scalar gradient as $\partial\langle c\rangle/\partial x_j=1$ leads to an equation for $\mathscr{c}^{00}(\mathbf{x},t)$. Specifying the mean scalar gradient as higher-order polynomials leads to higher-order $\mathscr{c}^{mn}(\mathbf{x},t)$, and equations for the lower-order $\mathscr{c}^{mn}(\mathbf{x},t)$ can be analytically subtracted to derive an equation for the desired order of $\mathscr{c}^{mn}(\mathbf{x},t)$. The $\mathscr{c}^{mn}(\mathbf{x},t)$ fields can then be used to compute the moments by multiplying (23) by $-u_i'$ and averaging:

$$-\langle u_i'c'\rangle(\mathbf{x},t)=-\left[\langle u_i'\mathscr{c}_j^{00}\rangle(\mathbf{x},t)+\langle u_i'\mathscr{c}_{jk}^{10}\rangle(\mathbf{x},t)\frac{\partial}{\partial x_k}+\cdots+\langle u_i'\mathscr{c}_j^{01}\rangle(\mathbf{x},t)\frac{\partial}{\partial t}+\ldots\right]\frac{\partial\langle c\rangle}{\partial x_j}. \tag{27}$$

Comparison with the expansion in (6) leads to

$$-\langle u_i'\mathscr{c}_j^{mn}\rangle(\mathbf{x},t)=D_{ij}^{mn}(\mathbf{x},t). \tag{28}$$

Consider the simple 1D example from Section 3, where averaging is taken over all spatial direction except x_1 and there is only one component of the scalar flux, $\langle u_1'c'\rangle(x_1,t)$. To compute the zeroth-order moment, we specify $\partial\langle c\rangle/\partial x_1=1$ and substitution of the mean scalar gradient into (23) leads to:

$$c'(\mathbf{x},t)=\mathscr{c}^{00}(\mathbf{x},t), \tag{29}$$

where we have omitted the subscript to only consider the $\mathscr{c}=\mathscr{c}_1$ component. Substitution of (29) into the forced scalar fluctuation transport equation in (22) leads to the equation for $\mathscr{c}^{00}(\mathbf{x},t)$:

$$\frac{\partial\mathscr{c}^{00}}{\partial t}+\frac{\partial}{\partial x_i}(u_i\mathscr{c}^{00})=D_M\frac{\partial^2\mathscr{c}^{00}}{\partial x_i\partial x_i}-u_i\delta_{i1}+s^{00}, \tag{30}$$

where the inverse MFM forcing maintains the specified mean scalar gradient by equivalently maintaining $\langle c' \rangle(x_1, t) = \langle \mathscr{c}^{00} \rangle(x_1, t) = 0$. Postprocessing $-\langle u_1' \mathscr{c}^{00} \rangle(x_1, t)$ leads to the zeroth-order moment of the eddy diffusivity, $D^{00}(x_1, t)$.

To compute the first-order temporal moment, we specify $\partial \langle c \rangle / \partial x_1 = t$ and substitution of the mean scalar gradient into (23) leads to:

$$c'(\mathbf{x}, t) = t\mathscr{c}^{00}(\mathbf{x}, t) + \mathscr{c}^{01}(\mathbf{x}, t), \tag{31}$$

and substitution of the the decomposed scalar fluctuation in (31) into (22) gives:

$$t\frac{\partial \mathscr{c}^{00}}{\partial t} + \mathscr{c}^{00} + \frac{\partial \mathscr{c}^{01}}{\partial t} + t\frac{\partial}{\partial x_i}(u_i \mathscr{c}^{00}) + \frac{\partial}{\partial x_i}(u_i \mathscr{c}^{01}) = D_M \left(t\frac{\partial^2 \mathscr{c}^{00}}{\partial x_i \partial x_i} + \frac{\partial^2 \mathscr{c}^{01}}{\partial x_i \partial x_i} \right) - t u_i \delta_{i1} + s. \tag{32}$$

We analytically subtract the equation for $\mathscr{c}^{00}(\mathbf{x}, t)$ in (30) multiplied by t from Equation (32) to arrive at an equation for $\mathscr{c}^{01}(\mathbf{x}, t)$:

$$\frac{\partial \mathscr{c}^{01}}{\partial t} + u_i \frac{\partial \mathscr{c}^{01}}{\partial x_i} = D_M \frac{\partial^2 \mathscr{c}^{01}}{\partial x_i \partial x_i} - \mathscr{c}^{00} + s^{01}, \tag{33}$$

where we have relabeled the inverse MFM forcing as $s^{01} = s - s^{00}t$. The forcing maintains $\langle \mathscr{c}^{01} \rangle(x_1, t) = 0$. Postprocessing $-\langle u_1' \mathscr{c}^{01} \rangle(x_1, t)$ leads to the first-order temporal moment of the eddy diffusivity, $D^{01}(x_1, t)$. Note the equation for $\mathscr{c}^{01}(\mathbf{x}, t)$ is coupled with the equation for $\mathscr{c}^{00}(\mathbf{x}, t)$. Generally, higher-order $\mathscr{c}^{mn}(\mathbf{x}, t)$ are one-way coupled with lower-order $\mathscr{c}^{mn}(\mathbf{x}, t)$.

The cost of using the decomposition method is identical to the cost of MFM. By treating the forcing semi-analytically, the decomposition method can be used for periodic problems where the mean scalar gradient needed for MFM, e.g., $\partial \langle c \rangle / \partial x_1 = x_1$, may be incompatible with periodic boundary conditions. The equations for the decomposed variables satisfy the periodic boundary conditions and all explicit dependence on the coordinate is analytically removed. Moreover, the decomposition method also allows one to probe different directions of the eddy diffusivity independently. For example, consider a 2D problem, where $-\langle u_i' c' \rangle(x_1, x_2)$ and $\langle c \rangle(x_1, x_2)$. The decomposition method allows one to specify various directions of the mean scalar gradient, e.g., $\partial \langle c \rangle / \partial x_1 = x_2$ and $\partial \langle c \rangle / \partial x_2 = 0$, even when a $\langle c \rangle(x_1, x_2)$ that satisfies both desired gradients may not exist. This allows one to probe different directions of the eddy diffusivity, e.g., quantify D_{11} independently from D_{12}. However, the resulting closure for $-\langle u_i' c \rangle$ is still mathematically consistent as a linear superposition of the various components of the eddy diffusivity.

5. Generalization to momentum transport

The generalized closure can be extended to momentum transport, which is governed by the incompressible Navier–Stokes equations:

$$\frac{\partial u_i}{\partial t} + \frac{\partial}{\partial x_j}(u_j u_i) = -\frac{1}{\rho}\frac{\partial p}{\partial x_i} + \nu \frac{\partial^2 u_i}{\partial x_j \partial x_j} + r_i, \tag{34a}$$

$$\frac{\partial u_i}{\partial x_i} = 0, \tag{34b}$$

where $p(\mathbf{x},t)$ is pressure, ρ is the fluid density, ν is the kinetic viscosity, and $r_i(\mathbf{x},t)$ is a general body force. Reynolds averaging results in the Reynolds-averaged Navier-Stokes (RANS) equations:

$$\frac{\partial\langle u_i\rangle}{\partial t}+\frac{\partial}{\partial x_j}\left(\langle u_j\rangle\langle u_i\rangle\right)=-\frac{1}{\rho}\frac{\partial\langle p\rangle}{\partial x_i}+\nu\frac{\partial^2\langle u_i\rangle}{\partial x_j\partial x_j}-\frac{\partial}{\partial x_j}\langle u_j'u_i'\rangle+\langle r_i\rangle. \tag{35}$$

The generalized nonlocal and anisotropic eddy viscosity [3] is

$$-\langle u_i'u_j'\rangle(\mathbf{x},t)=\int\int D_{ijkl}(\mathbf{x},\mathbf{x}',t,t')\left.\frac{\partial\langle u_l\rangle}{\partial x_k}\right|_{\mathbf{x}',t'}\mathrm{d}\mathbf{x}'\mathrm{d}t'. \tag{36}$$

To compute the generalized eddy viscosity, Mani and Park [1] simultaneously solve the Navier–Stokes equations in (34a) and (34b) and the generalized momentum (GMT) equations:

$$\frac{\partial v_i}{\partial t}+\frac{\partial}{\partial x_j}\left(u_jv_i\right)=-\frac{1}{\rho}\frac{\partial q}{\partial x_i}+\nu\frac{\partial^2 v_i}{\partial x_j\partial x_j}+s_i, \tag{37a}$$

$$\frac{\partial v_i}{\partial x_i}=0, \tag{37b}$$

where $v_i(\mathbf{x},t)$ is a vector field that is kept solenoidal by the scalar field $q(\mathbf{x},t)$, which acts similar to pressure, and s_i is an added forcing that is not necessarily the same as r_i. The velocity field u_j is computed from the Navier–Stokes equations, i.e., the GMT equations in (37a) and (37b) are one-way coupled with the Navier–Stokes equations in (34a) and (34b). The generalized closure [3] for the GMT equations is

$$-\langle u_i'v_j'\rangle(\mathbf{x},t)=\int\int D_{ijkl}(\mathbf{x},\mathbf{x}',t,t')\left.\frac{\partial\langle v_l\rangle}{\partial x_k}\right|_{\mathbf{x}',t'}\mathrm{d}\mathbf{x}'\mathrm{d}t'. \tag{38}$$

This closure is exact for the GMT equations, and the relationship between the closure operator in (38) and in (36) is further discussed in Mani and Park [1] and Hamba [3]. Park and Mani [11] numerically showed that substitution of the MFM-measured eddy viscosity kernel, $D_{ijkl}(\mathbf{x},\mathbf{x}',t,t')$, from (38) into (36) with the DNS mean velocity gradient results in Reynolds stresses identical to DNS for turbulent channel flow.

Taking the Taylor series expansion of the nonlocal and anisotropic eddy viscosity in (38) locally about $\mathbf{x}'=\mathbf{x}$ and $t'=t$:

$$-\langle u_i'v_j'\rangle(\mathbf{x},t)=\left[D^{00}_{ijkl}(\mathbf{x},t)+D^{10}_{ijklm}(\mathbf{x},t)\frac{\partial}{\partial x_m}+\cdots+D^{01}_{ijkl}(\mathbf{x},t)\frac{\partial}{\partial t}+\cdots\right]\frac{\partial\langle v_l\rangle}{\partial x_k} \tag{39}$$

where

$$D^{00}_{ijkl}(\mathbf{x},t)=\int\int D_{ijkl}(\mathbf{x},\mathbf{x}',t,t')\mathrm{d}\mathbf{x}'\mathrm{d}t', \tag{40}$$

$$D^{10}_{ijklm}(\mathbf{x},t)=\int\int (x_m'-x_m)D_{ijkl}(\mathbf{x},\mathbf{x}',t,t')\mathrm{d}x_m'\mathrm{d}t', \tag{41}$$

$$\vdots$$

$$D^{01}_{ijkl}(\mathbf{x},t)=\int\int (t'-t)D_{ijkl}(\mathbf{x},\mathbf{x}',t,t')\mathrm{d}\mathbf{x}'\mathrm{d}t'. \tag{42}$$

Similar to scalar transport in Section 4, the MFM fluctuating velocity and pressure fields can be expanded as

$$v_j'(\mathbf{x},t) = \left[v_{jkl}'^{00}(\mathbf{x},t) + v_{jklm}'^{10}(\mathbf{x},t)\frac{\partial}{\partial x_m} + \cdots + v_{jkl}'^{01}(\mathbf{x},t)\frac{\partial}{\partial t} + \cdots \right] \frac{\partial \langle v_l \rangle}{\partial x_k}, \tag{43}$$

$$q(\mathbf{x},t) = \left[q_{kl}^{00}(\mathbf{x},t) + q_{klm}^{10}(\mathbf{x},t)\frac{\partial}{\partial x_m} + \cdots + q_{kl}^{01}(\mathbf{x},t)\frac{\partial}{\partial t} + \cdots \right] \frac{\partial \langle v_l \rangle}{\partial x_k}. \tag{44}$$

For example, for a turbulent channel flow in which averaging is taken over the homogeneous streamwise (x_1) and spanwise (x_3) directions, the Reynolds stresses are only a function of the wall-normal (x_2) direction. The only nonzero component of the mean velocity gradient is $\partial\langle u_1\rangle/\partial x_2$. To compute the zeroth moment of the generalized eddy viscosity using inverse MFM, one would specify $\partial\langle v_1\rangle/\partial x_2 = 1$, and similar to scalar transport in Section 4, substitution of the specified mean velocity gradient into Equations (37a)-(37b) and Equations (43)-(44) leads to:

$$\frac{\partial v_{j21}'^{00}}{\partial t} + u_2\delta_{j1} + \frac{\partial}{\partial x_i}(u_i v_{j21}'^{00}) = -\frac{1}{\rho}\frac{\partial q_{21}^{00}}{\partial x_j} + \nu\frac{\partial^2 v_{j21}'^{00}}{\partial x_i \partial x_i} + s_j^{00}, \tag{45a}$$

$$\frac{\partial v_{j21}'^{00}}{\partial x_j} = 0, \tag{45b}$$

where inverse MFM is used to enforce $\langle s_j^{00}\rangle = 0$. Postprocessing $-\langle u_i' v_{j21}'^{00}\rangle$ leads to the zeroth-order moment of the eddy viscosity, D_{ij21}^{00}.

For the first-order spatial moment in the wall-normal direction, substitution of $\partial\langle v_1\rangle/\partial x_2 = x_2$ into Equations (37a)-(37b) and (43)-(44) and subtraction of the equations for the zeroth-order moment in (45a)-(45b) leads to

$$\frac{\partial v_{j212}'^{10}}{\partial t} + u_2 v_{j21}'^{00} + \frac{\partial}{\partial x_i}(u_i v_{j212}'^{10}) = -\frac{1}{\rho}\left[q_{21}^{00}\delta_{j2} + \frac{\partial q_{212}^{10}}{\partial x_j} \right] + \nu\left[2\frac{\partial v_{j21}'^{00}}{\partial x_2} + \frac{\partial^2 v_{j212}'^{10}}{\partial x_i \partial x_i} \right] + s_j^{10}, \tag{46a}$$

$$\frac{\partial v_{j212}'^{10}}{\partial x_j} = -v_{221}'^{00}. \tag{46b}$$

Inverse MFM is used to enforce $\langle s_j^{10}\rangle = 0$, and postprocessing $-\langle u_i' v_{j212}'^{10}\rangle$ leads to the first-order spatial moment of the eddy viscosity, D_{ij212}^{10}.

The continuity equation in (46b) is a direct result of substitution of the decomposition for v_j' in Equation (43) into $\partial v_j'/\partial x_j = 0$. Generally, in cases where the specified mean velocity gradient is not solenoidal, we enforce the solenoidal condition on v_j' rather than on v_j. As discussed in Liu et al. [13], the specified mean velocity gradient can be considered as a MFM forcing to the continuity equation for v_j that satisfies the requisite property $s = \langle s\rangle$.

Similarly, for the first-order temporal moment, substitution of $\partial\langle v_1\rangle/\partial x_2 = t$ into Equations (37a)-(37b) and (43)-(44) and subtraction of the equations for the zeroth-order moment in (45a)-(45b)

leads to

$$\frac{\partial v'^{01}_{j21}}{\partial t} + v'^{00}_{j21} + \frac{\partial}{\partial x_i}(u_i v'^{01}_{j21}) = -\frac{1}{\rho}\frac{\partial q^{01}_{21}}{\partial x_j} + \nu\frac{\partial^2 v'^{01}_{j21}}{\partial x_i \partial x_i} + s^{01}_j, \tag{47a}$$

$$\frac{\partial v'^{01}_{j21}}{\partial x_j} = 0. \tag{47b}$$

Inverse MFM is used to enforce $\langle s^{01}_j \rangle = 0$, and postprocessing $-\langle u'_i v'^{01}_{j21} \rangle$ leads to the first-order temporal moment of the eddy viscosity, D^{01}_{ij21}. In Park et al. [14], we computed the first-order temporal moment for turbulent channel flow at $Re_\tau = 180$. We then used the temporal moment as a qualitative estimate for a nonlocality timescale in a simple nonlocal model for a 2D separated boundary layer.

As was the case for scalar transport, the equations for momentum transport for higher-order spatiotemporal moments generally depends on lower-order moments, which are solved simultaneously. Equations for higher-order moments are one-way coupled with lower-order moments and does not raise the cost of the MFM procedure.

6. Case study: Rayleigh–Taylor instability

As an illustrative case study, we demonstrate the decomposition method for mean scalar transport in two-dimensional (2D) RT instability. RT instability occurs when a heavier fluid is accelerated into a lighter fluid with a perturbation at the interface of the two fluids. Over time, the instability becomes self-similar and enters a turbulent state. RT instability is a chaotic, unsteady flow, so statistical convergence must be achieved through ensemble averaging. In the 2D RT problem, the only homogeneous direction is x_1, and there is no homogeneity in time that can be leveraged for ensemble averaging. Thus, many realizations of RT instability, each with different initial conditions, are required to get statistical convergence of the eddy diffusivity moments. This corresponds to many DNS, which lends to the high computational expense of MFM for this problem. Past work Lavacot et al. [9] showed that $\mathcal{O}(10^3)$ DNS are required for statistical convergence of eddy diffusivity moments in 2D RT instability. In this case study, the decomposition method of MFM is applied to 2D RT instabiity to achieve faster statistical convergence of the eddy diffusivity moments.

6.1. Self-similarity

The MFM analysis is done in the self-similar limit of RT instability. In this limit, the mixing half width h, defined as half of the sum of the RT instability bubble and spike heights, is expected to grow quadratically in time:

$$h = \alpha A g t^2, \tag{48}$$

where A is the Atwood number, defined as

$$A = \frac{\rho_H - \rho_L}{\rho_H + \rho_L}, \tag{49}$$

where ρ_H is the density of the heavy fluid, and ρ_L is the density of the light fluid. Thus, a self-similar variable can be defined:

$$\eta = \frac{y}{h(t)}. \tag{50}$$

The mixing width can be computed from the mass fraction:

$$h \equiv 4 \int \langle Y_H \left(1 - Y_H\right) \rangle dy, \tag{51}$$

where $\langle * \rangle$ denotes an ensemble average; for this 2D RT problem, the averaging is done in x and over realizations. In a RANS simulation, h can instead be computed using closed quantities, as defined by Cabot and Cook [15] and Morgan et al. [16]:

$$h_{\text{hom}} \equiv 4 \int \langle Y_H \rangle \left(1 - \langle Y_H \rangle\right) dy. \tag{52}$$

A mixedness parameter ϕ can also be defined (Morgan et al. [16], Youngs [17]):

$$\phi \equiv \frac{h}{h_{\text{hom}}} = 1 - 4\frac{\int \langle Y_H' Y_H' \rangle dy}{h_{\text{hom}}}. \tag{53}$$

ϕ is expected to converge to a steady-state value in the self-similar limit.

6.2. Governing equations

The compressible Navier-Stokes equations are solved in the donor simulation:

$$\frac{D\rho}{Dt} = -\rho \frac{\partial u_i}{\partial x_i}, \tag{54}$$

$$\rho \frac{DY_\alpha}{Dt} = \frac{\partial}{\partial x_i}\left(\rho D_\alpha \frac{\partial Y_\alpha}{\partial x_i}\right), \tag{55}$$

$$\rho \frac{Du_j}{Dt} = -\frac{\partial}{\partial x_i}\left(p\delta_{ij} + \sigma_{ij}\right) + \rho g_j, \tag{56}$$

$$\rho \frac{De}{Dt} = -p\frac{\partial u_i}{\partial x_i} + \frac{\partial}{\partial x_i}\left(u_i \sigma_{ij} - q_j\right). \tag{57}$$

ρ is density, u_i is velocity, Y_α is mass fraction of component α, D_α is the molecular diffusivity of component α (in the problem considered here, $D_\alpha = D_M$), p is pressure, g_j is gravity (only the x_2 component is active in this problem), e is specific internal energy. The viscous stress σ_{ij} and the heat flux q_{ij} are

$$\sigma_{ij} = \mu\left(\frac{\partial u_i}{\partial x_j} + \frac{\partial u_j}{\partial x_i}\right) - \mu\frac{2}{3}\frac{\partial u_k}{\partial x_k}\delta_{ij}, \tag{58}$$

$$q_j = -\kappa\frac{\partial T}{\partial x_j} - \sum_{\alpha=1}^{N} h_\alpha \rho D_\alpha \frac{\partial Y_\alpha}{\partial x_j}. \tag{59}$$

Moment	$\frac{\partial Y_H}{\partial x_2}$
D^{00}	1
D^{01}	t
D^{10}	$x_2 - \frac{1}{2}$
D^{20}	$\frac{1}{2}(x_2 - \frac{1}{2})^2$

Table 1: Mean mass fraction gradients forced for each eddy diffusivity moment D^{mn} in the 2D RT case study.

μ is the dynamic viscosity, κ is the thermal conductivity, T is temperature, and h_α is the specific enthalpy of species α. Component pressures are determined using ideal gas equations of state. The total pressure is a weighted sum of component pressures:

$$p = \sum_{\alpha=1}^{N} v_\alpha p_\alpha. \tag{60}$$

More details on these equations can be found in Lavacot et al. [9] and Morgan et al. [18].

6.3. Computation of eddy diffusivity moments

For RT instability, after averaging over the homogeneous x_1 direction, the only surviving turbulent flux is $-\langle u_2' c' \rangle$, where c is the mass fraction of the heavy fluid, Y_H. The Kramers-Moyal expansion in Equation 6 becomes

$$-\langle u_2' c' \rangle(\mathbf{x}, t) = D^{00}\frac{\partial \langle c \rangle}{\partial x_2} + D^{10}\frac{\partial^2 \langle c \rangle}{\partial x_2^2} + D^{01}\frac{\partial^2 \langle c \rangle}{\partial t \partial x_2} + D^{20}\frac{\partial^3 \langle c \rangle}{\partial x_2^3} + \dots \tag{61}$$

In this work, D^{00}, D^{01}, D^{10}, and D^{20} are computed.

In standard MFM, forcings would be applied directly to Equation 55, and the eddy diffusivity moments would be obtained in postprocessing. For example, to compute D^{10}, a macroscopic forcing to Equation 55 would be determined to enforce $\frac{\partial \langle Y_H \rangle}{\partial x_2} = x_2$. From the solution to that receiver equation, the moment is computed as $D^{10} = -\langle u_2' c' \rangle|_{\frac{\partial \langle Y_H \rangle}{\partial x_2} = x_2} - x_2 D^{00}$. The forcings for the other moments are shown in Table 1.

Here, we instead use the decomposition MFM to determine the eddy diffusivity moments. According to the decomposition described in §4, we derive four receiver equations for this problem:

$$\frac{\partial c^{00}}{\partial t} + u_i \frac{\partial c^{00}}{\partial x_i} = D_M \frac{\partial^2 c^{00}}{\partial x_i \partial x_i} - u_i \delta_{i2} + s^{00}, \tag{62}$$

$$\frac{\partial c^{10}}{\partial t} + u_i \frac{\partial c^{10}}{\partial x_i} = D_M \frac{\partial^2 c^{10}}{\partial x_i \partial x_i} + D_M \left(1 + 2\frac{\partial c^{00}}{\partial x_i}\delta_{i2}\right) - u_i \delta_{i2} c^{00} + s^{10}, \tag{63}$$

$$\frac{\partial c^{01}}{\partial t} + u_i \frac{\partial c^{01}}{\partial x_i} = D_M \frac{\partial^2 c^{01}}{\partial x_i \partial x_i} - c^{00} + s^{01}, \tag{64}$$

$$\frac{\partial c^{20}}{\partial t} + u_i \frac{\partial c^{20}}{\partial x_i} = D_M \frac{\partial^2 c^{20}}{\partial x_i \partial x_i} + D_M \left(c^{00} + 2\frac{\partial c^{10}}{\partial x_i}\delta_{i2}\right) - u_i \delta_{i2} c^{10} + s^{20}. \tag{65}$$

The forcings s^{ij} are determined to enforce zero means in x for each c^{ij} in each realization. These forcings are computed per timestep in each realization, as detailed in Lavacot et al. [9]. With this formulation, the forcings in Table 1 are now semi-analytically applied. Each moment is computed in postprocessing:

$$D^{mn} = -\langle u_2' c^{mn} \rangle. \tag{66}$$

6.4. Simulations

The hydrodynamics solver Ares [19, 20] is used to run 2D RT simulations. Ares uses an arbitrary Lagrangian-Eulerian (ALE) method based on Sharp and Barton [21]. In this method, equations are solved in a Lagrangian frame and then remapped to an Eulerian mesh using a second-order scheme. Ares uses a second-order non-dissipative finite element method in space and a second-order explicit predictor-corrector scheme in time.

MFM is performed two different ways to measure eddy diffusivity moments for the 2D RT instability. The first is the standard MFM. In this case, for each realization, four receiver equations are solved alongside four separate donor equations, but all use the same initial conditions. The second case is the decomposition method, in which a single donor is used and the MFM forcing is applied semi-analytically, as described in §4. In the decomposition MFM, for each realization of RT instability, the four receiver equations (Equations (62)-(65)) are solved alongside one set of donor equations (Equations (54)-(57)).

The 2D simulations are run on a square domain of 2049×2049 cells with periodic boundary conditions in x_1 and no slip and no penetration in x_2. To trigger the instability, a tophat perturbation in wavespace between the heavy and light fluids is applied to the density field. The perturbation has a minimum wavenumber $\kappa_{min} = 8$, a maximum wavenumber $\kappa_{max} = 256$, and an amplitude of $\frac{\Delta}{\kappa_{max} - \kappa_{min} + 1}$, where Δ is the grid size. The simulations are stopped when the mixing width is approximately 30% the size of the domain.

The relevant nondimensional numbers of this problem are the Atwood number (A), the Reynolds number (Re) (which is set in the simulation by a numerical Grashof number (Gr)), Mach number (Ma), Peclet number (Pe), and Schmidt number (Sc). The Atwood number has already been defined; the rest are defined in Table 2. The RT flow can be considered turbulent when $Re_T > 100$ or

Number	Definition	Value
$Ma_{\max}$	$\frac{u}{c}$	0.05
Gr	$\frac{-2gA\Delta^3}{\nu^2}$	1
Sc	$\frac{\nu}{D_M}$	1
Re_T	$\frac{k^{1/2}\lambda}{\nu}$	54
Pe_T	$Re_T Sc$	54
Re_L	$\frac{h_{99}\dot{h}_{99}}{\nu}$	$8,000$
Pe_L	$Re_L Sc$	$8,000$

Table 2: Nondimensional numbers of simulated RT instability. Here, c is the speed of sound (set by the heat capacity ratio γ, which is 5/3 in the simulation), Δ is the grid spacing (the mesh is uniform, so $\Delta = \Delta_x = \Delta_y$), and D_M is the molecular diffusivity. The subscripts T and L refer to nondimensional numbers using the Taylor microscale (λ) and large-scale, respectively.

$Re_L > 10,000$ Dimotakis [22]. Details on how these numbers are computed for the donor simulation can be found in Lavacot et al. [9].

The values of each nondimensional number in this work are summarized in Table 2. Since the Atwood number is small, the bouyant-flow Boussinesq approximation can be made. Thus, it is assumed that mean velocities are negligible. In addition, a small Grashof number is used to minimize numerical diffusion and keep the simulation close to a DNS. It was found by Morgan and Black [23] that numerical diffusivity dominates molecular diffusivity when $Gr > 12$. Finally, it must be noted that Re_T and Re_L of the RT instability simulated here are lower than the turbulent transition criteria set by Dimotakis [22]. This indicates that the flow may not be fully turbulent; in fact, the simulation is 2D, so it cannot be truly turbulent. However, the late-time profiles from the simulations show self-similar behavior (see Lavacot et al. [9]), so self-similar analysis is valid.

6.5. Donor solution

Figure 3 shows the mixing half-widths measured from the standard MFM donor simulations. These donors use the same initial conditions, but due to numerical differences in parallel processes, Ares gives slightly different h at late time. For h, the percent error is only $\mathcal{O}(1\%)$, but the statistical error is amplified in the computation of higher-order eddy diffusivity moments, as discussed previously in §3.1. A more detailed description of the donor simulations can be found in Lavacot et al. [9].

6.6. Eddy diffusivity moments

The solutions to the receiver equations are postprocessed to obtain the eddy diffusivity moments.

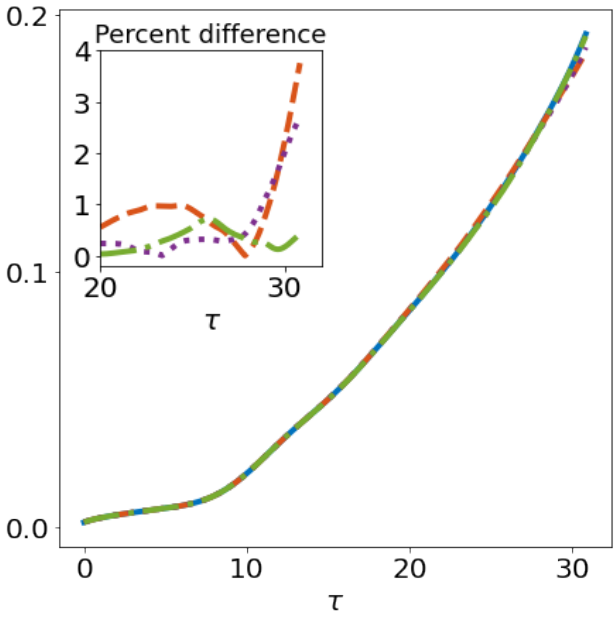

Figure 3: Mixing half-width h measured from different donor simulations in Ares for the same initial conditions. Inset plot is the percent differences of the last three donors with respect to the first donor.

Figure 4 shows eddy diffusivity moments measured using standard MFM. The data are averaged over $1,000$ realizations. Even with this large number of realizations, the standard MFM measurements exhibit substantial statistical error, especially in the higher-order moments; D^{01}, the first order moment in time is particularly affected by this issue. Figure 5 shows eddy diffusivity moments measured using the decomposition MFM. The D^{00} measurements using the two methods are qualitatively similar and have about the same level of statistical error. This is expected, since the calculations for the leading order moment in either method are mathematically equivalent. Among the higher-order moments, the decomposition MFM measurements show significantly improved statistical convergence at only 200 averaged realizations. This improvement is most noticeable in the measurement of D^{01}, which qualitatively shows less statistical error than the measurments made using standard MFM.

Since the statistical error is most obvious in the measurements of D^{01}, those measurements averaged over different numbers of realizations are presented in Figure 6. Even at just one realization, the decomposition MFM measurement exhibits much less statistical error than the standard MFM. As the number of realizations increases, the statistical error reduces much faster in the decomposition MFM than in the standard MFM. Visually, the decomposition MFM measurement has an acceptable level of statistical error at only 100 averaged realizations, but the standard MFM still has a high level of statistical error. Plots of the statistical convergence of the other moments can be found in Figures B.9 and B.10 in the Appendix.

Figure 7 shows plots of D^{10} measurements with qualitatively similar levels of statistical error. Statistical convergence is achieved with a higher number of realizations for the standard method

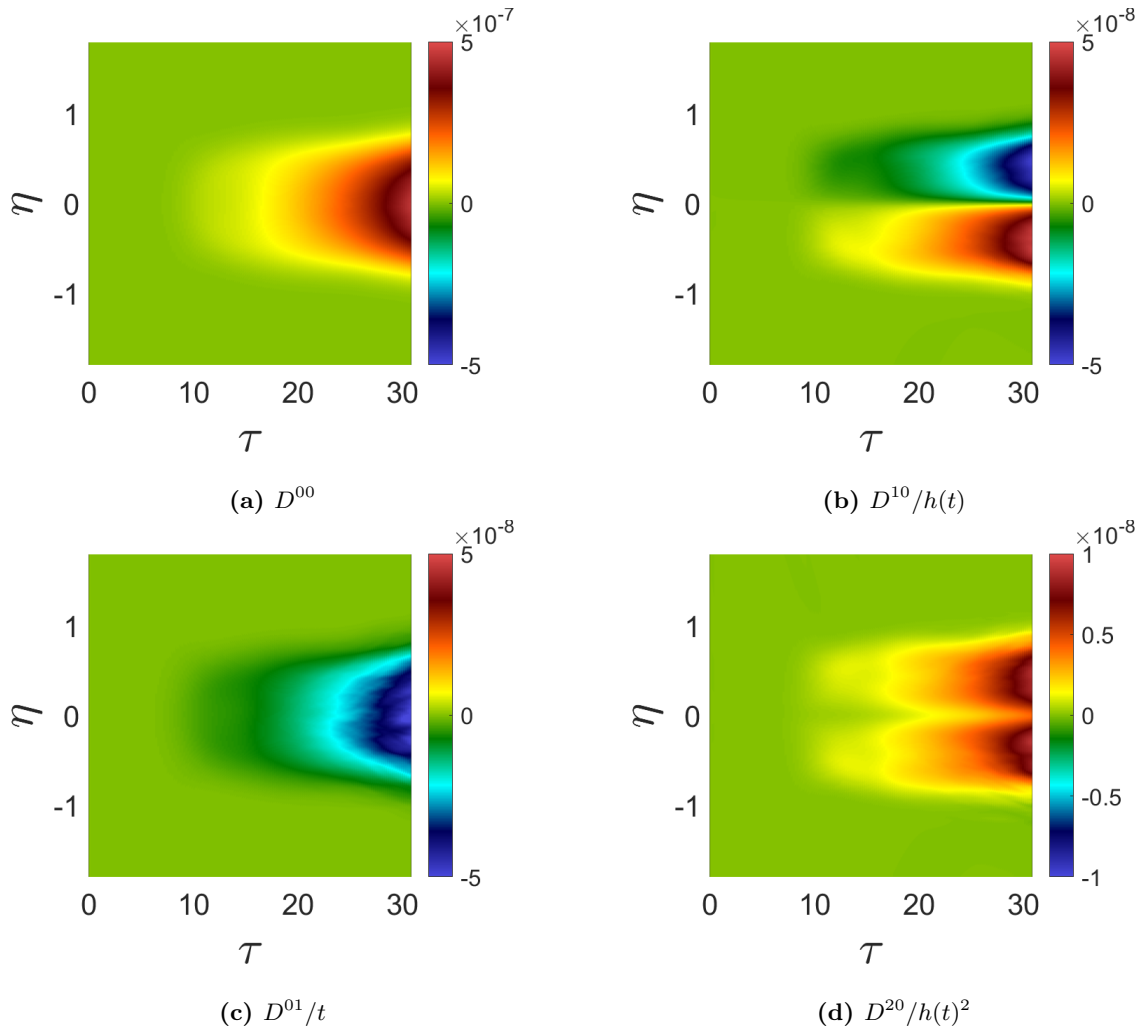

(a) D^{00} **(b)** $D^{10}/h(t)$

(c) D^{01}/t **(d)** $D^{20}/h(t)^2$

Figure 4: Normalized moments of the eddy diffusivity kernel of RT instability measured using the standard MFM. Data is averaged over 1,000 realizations and homogeneous direction x.

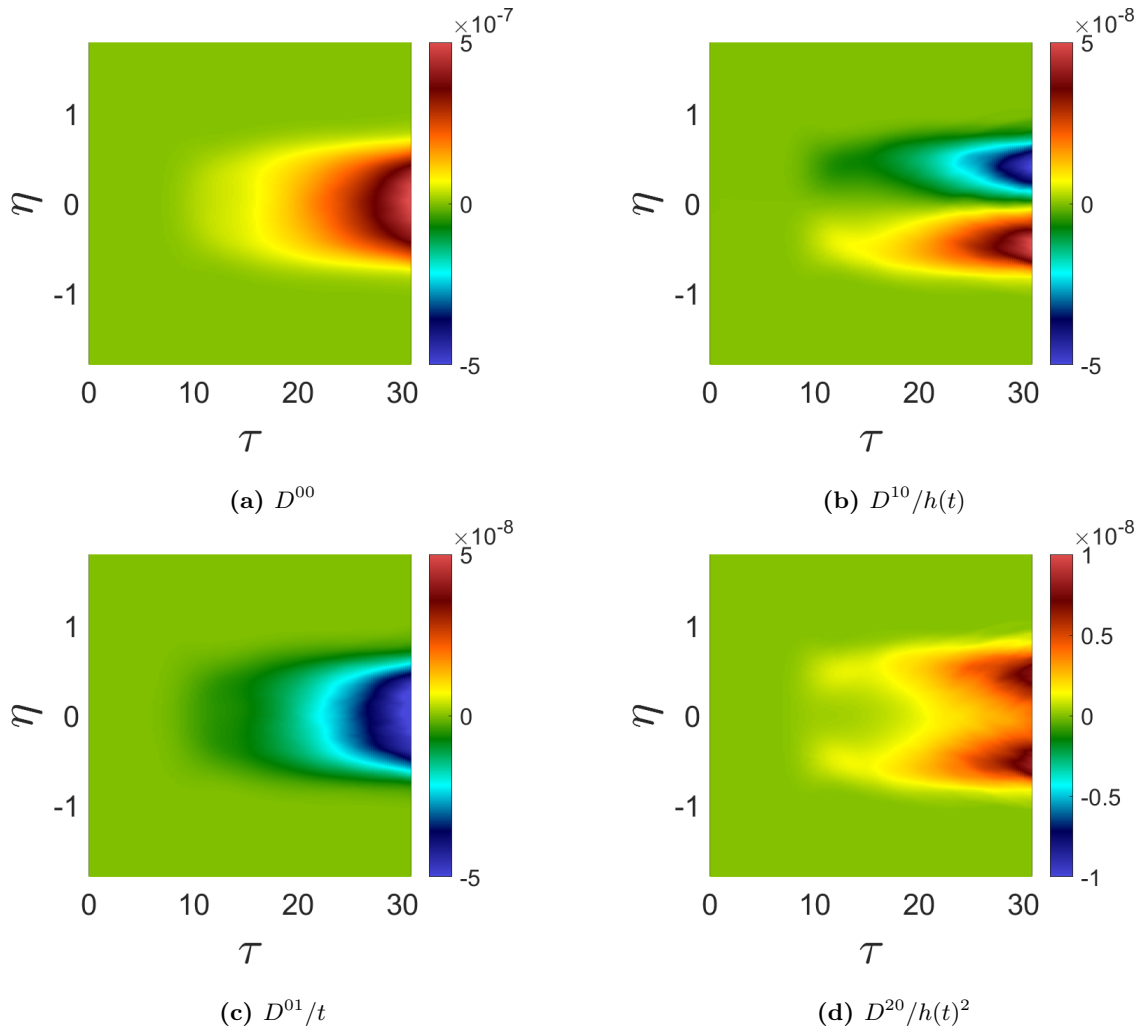

(a) D^{00} **(b)** $D^{10}/h(t)$

(c) D^{01}/t **(d)** $D^{20}/h(t)^2$

Figure 5: Normalized moments of the eddy diffusivity kernel of RT instability measured using the decomposition MFM. Data is averaged over 200 realizations and homogeneous direction x.

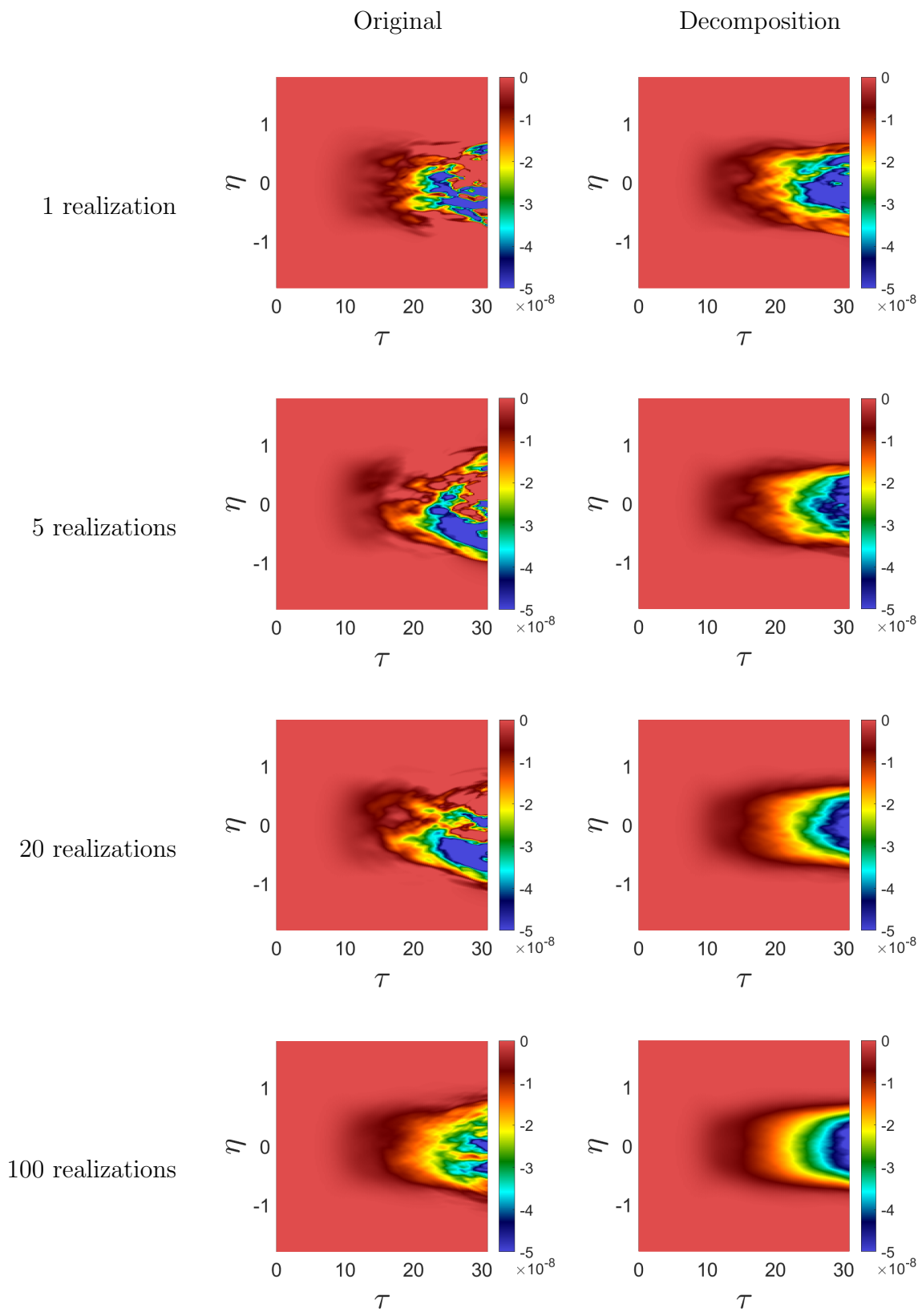

Figure 6: Convergence of D^{01} (normalized by t) MFM measurement using standard and decomposition methods for RT instability case.

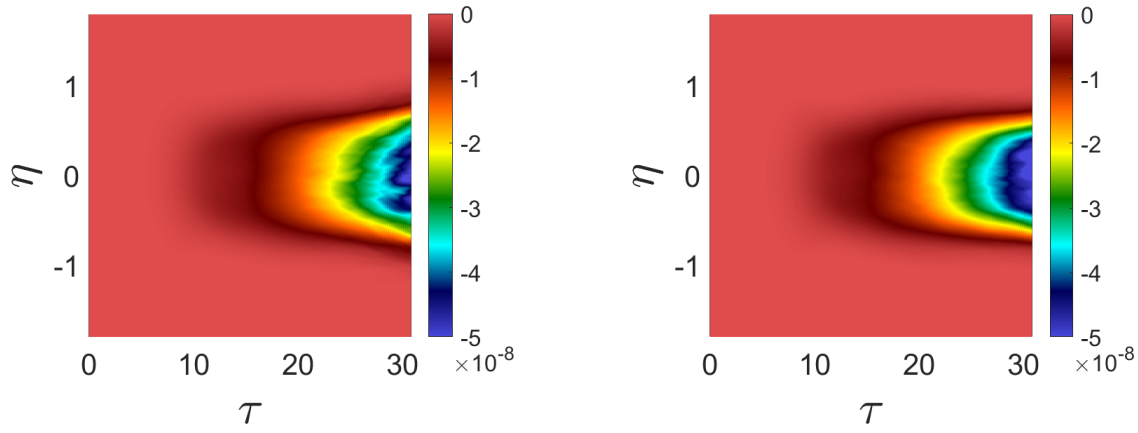

(a) Standard method, 1,000 realizations.

(b) Decomposition method, 100 realizations.

Figure 7: Qualitatively-similar states of statistically convergence of D^{01} (normalized by t) for each method.

(1,000) compared to the decomposition method (100). This suggests that the decomposition MFM may offer a speedup factor of about ten for the statistical convergence of MFM simulations.

6.7. Impact on modeling

Statistical convergence is crucial for development of accurate models. High statistical error can obstruct analysis by causing incorrect conclusions about the convergence of model predictions. Here, we demonstrate the impact of statistical error on the matched moment inverse (MMI) procedure for constructing a model for 2D RT instability. MMI is a systematic method for modeling nonlocal eddy diffusivity based on MFM-measured eddy diffusivity moments Liu et al. [8]. When applied to this spatiotemporal 2D RT problem, The result of the method is an implicit model form:

$$\left[1 + a^{01}\frac{\partial}{\partial t} + a^{10}\frac{\partial}{\partial x_2} + a^{20}\frac{\partial^2}{\partial x_2^2} + \ldots\right](-\langle u_2' c'\rangle) = a^{00}\frac{\partial\langle c\rangle}{\partial x_2}, \tag{67}$$

where $a^{mn}(x_2, t)$ are model coefficients determined using a process detailed in Liu et al. [8] and Lavacot et al. [9]. We use this implicit form rather than an explicit form that results from truncation of Equation 61 for several reasons. First, the Kramers-Moyal expansion does not converge. That is, finite truncation of the expansion leads to divergent results. This property of the Kramers-Moyal expansion was proven by Pawula [24] and was shown to be true in modeling eddy diffusivity by Liu et al. [8] and specifically in 2D RT instability by Lavacot et al. [9]. Secondly, an explicit form would be challenging to implement numerically in this spatiotemporal problem, since this would require time advancing spatial gradients of mixed derivatives. The implicit model addresses both of these issues. Equation 67 can be directly time-integrated using explicit methods. Additionally, the implicit method resulting from MMI converges as more terms are added. Details on this and the MMI process can be found in Liu et al. [8].

In Lavacot et al. [9], the importance of eddy diffusivity moments for modeling mean scalar transport was investigated using the standard MFM. Different combinations of moments (i.e., different

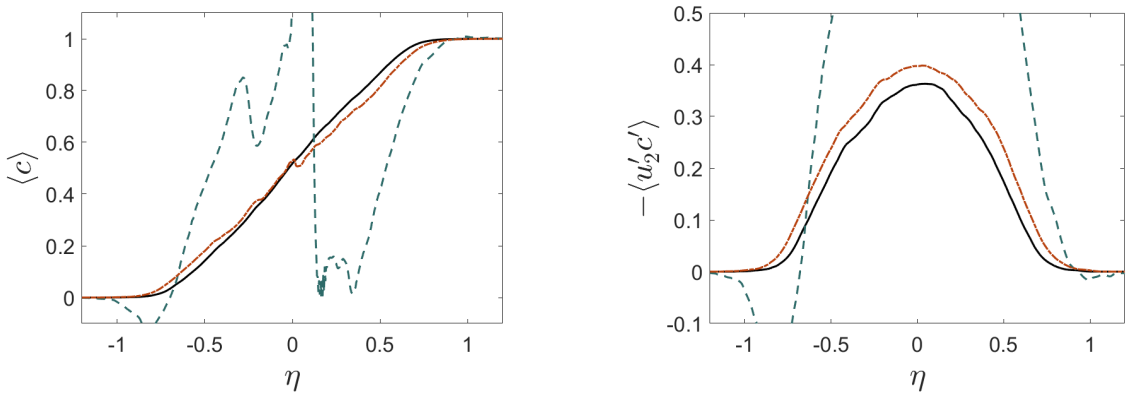

Figure 8: (a) Mean concentration profiles and (b) turbulent scalar flux from DNS (solid black) and models using eddy diffusivity moments measured with the standard MFM (dashed green) and decomposition MFM (dash-dotted red). Results from both methods are averaged over 200 realizations.

truncations of terms in the MMI operator in Equation 67) were tested to assess the importance of each moment. Here, we examine the truncation of the MMI operator to the four terms shown in Equation 67. Construction of this model form requires the eddy diffusivity moments D^{00}, D^{10}, D^{01}, and D^{20}. We compare results of models constructed directly using measurements of D^{mn} from the standard MFM and the decomposition MFM. For both methods, we use D^{mn} measurements averaged over 200 realizations. At this number of realizations, the moments are visually statistically converged for the decomposition MFM, but not the standard MFM.

Figure 8 shows mean concentration and turbulent scalar flux profiles resulting from each of the models. The results from the model using the standard MFM eddy diffusivity moments diverge significantly from the DNS results. This may lead to the incorrect conclusion that addition of terms in the MMI operator does not lead to convergence. However, the source of this error is actually the large amount of statistical error in the higher-order moments. On the other hand, the results from the model using the decomposition MFM moments agree much better with the DNS. There appears to be some statistical error still at this number of realizations, but there is not nearly as much as there is with the standard MFM-based model. This highlights the importance of statistically-converged higher order moments in modeling. Compared to the standard MFM, the decomposition MFM is a more efficient method for obtaining statistically-converged moments that are usable for constructing models.

7. Conclusion

In this work, modifications to the standard MFM are presented for faster statistical convergence of the eddy diffusivity moments. We first demonstrate the utility of using a single donor simulation for the receiver equations. Using a single donor prevents pileup of statistical error that may arise in separate donors, even when the same initial conditions are used. Due to the potentially slow

statistical convergence of MFM using separate donors, we recommend MFM using only one donor, though that may not be the natural implementation in some codes.

We also present formulations of the receiver equations based on the Kramers-Moyal expansion of the fluctuation field for both scalar and momentum transport—this is the decomposition MFM. Instead of solving for the scalar c, as in the standard MFM, the decomposition MFM solves for a variable based on the scalar fluctuation $\mathscr{c}$, allowing the mean forcing in the receiver equations to be handled semi-analytically. There is no additional cost to use decomposition MFM in place of the standard MFM, and the former has the added benefit that it also allows for consistent boundary condition treatment, such as in problems with periodic domains, like turbulent channel flow.

Decomposition MFM differs from other methods for accelerating MFM in its purpose for measuring eddy diffusivity (or eddy viscosity) moments. Fast MFM [12] was developed for approximating the nonlocal and anisotropic eddy diffusivity for the entire domain by leveraging hidden sparsity in the discretized eddy diffusivity. Likewise, adjoint MFM [13] was developed for targeted computation of the exact nonlocal and anisotropic eddy diffusivity at specific locations in the domain using an adjoint-based approach rather than eddy diffusivity moments.

To demonstrate its utility, we apply the decomposition and single donor MFM to 2D RT instability. In this case study, we demonstrate an approximate speedup factor of ten in reaching statistical convergence of eddy diffusivity moments compared to MFM using separate donors. We show that this improved statistical convergence is substantial and significantly impacts analysis of models, as poorly-converged eddy diffusivity moments can lead to incorrect conclusions.

Acknowledgements. This work was performed under the auspices of the US Department of Energy by Lawrence Livermore National Laboratory under Contract No. DE-AC52-07NA27344. D.L. was additionally supported by the Charles H. Kruger Stanford Graduate Fellowship.

Appendix A. Error analysis

We present the following error analysis to illustrate the propogation of error due to different or matching donor simulations. This analysis is done in one dimension (x) for simplicity. First, we define F^i to be the measurements of the turbulent scalar flux used to determine D^i:

$$F^0 = \langle -u_1' c' \rangle|_{\frac{\partial \langle c \rangle}{\partial x_1}=1}, \tag{A.1}$$

$$F^1 = \langle -u_1' c' \rangle|_{\frac{\partial \langle c \rangle}{\partial x_1}=x_1} \tag{A.2}$$

Since the numerical mean uses a finite number of ensembles, there exists statistical error when making the measurements F^i. Examination of Equation 23 reveals that the statistical error arises due to $\mathscr{c}^{mn}$; $\frac{\partial \langle c \rangle}{\partial x_j}$ are deterministic as they are set by the macroscopic forcing. In this manner, we can rewrite Equation 30 with statistical error:

$$c' + \varepsilon = \left[(\mathscr{c}^0 + \varepsilon^0) + (\mathscr{c}^1 + \varepsilon^1) \frac{\partial}{\partial x_1} + (\mathscr{c}^2 + \varepsilon^2) \frac{\partial^2}{\partial x_1^2} + \dots \right] \frac{\partial \langle c \rangle}{\partial x_1}. \tag{A.3}$$

Thus, statistical error can also be written as a Kramers-Moyal expansion:

$$\varepsilon = \left[\varepsilon^0 + \varepsilon^1 \frac{\partial}{\partial x_1} + \varepsilon^2 \frac{\partial^2}{\partial x_1^2} + \dots\right] \frac{\partial \langle c \rangle}{\partial x_1}. \tag{A.4}$$

In the following analysis, we use the notation ε^{ij}, where i denotes the error associated with $\mathscr{c}^i$, as in Equation A.4, and j denotes the simulation used to determine D^j. The addition of index j is introduced, because when different donor simulations are used in MFM, each simulation has its own statistical error. For example, ε^{00} is not necessarily the same as ε^{01}, despite them both being errors associated with $\mathscr{c}^0$. The measurement of D^0 can then be written as

$$D^0 = F^0 + \varepsilon^{00}, \tag{A.5}$$

where ε^{00} arises from substituting $\frac{\partial \langle c \rangle}{\partial x_1} = 1$ into Equation A.4. Similarly, D^1 can be written as

$$D^1 = F^1 - x_1 D^0 + \varepsilon^{01} x + \varepsilon^{11} = F^1 - x_1 F^0 + x_1(\varepsilon^{01} - \varepsilon^{00}) + \varepsilon^{11} \tag{A.6}$$

If one donor simulation is used for all receiver equations in MFM, the third term above disappears, since $\varepsilon^{00} = \varepsilon^{01} = \varepsilon^0$. When different donors are used, ε^{00} and ε^{01} are not the same, so the overall statistical error scales with x_1, making statistical convergence for D^1 slower than for D^0. While this analysis is presented in one dimension, the variable x_1, can be considered as either a spatial or temporal variable. Since time can become large in numerical simulations, and measurements are often taken in late time, the statistical convergence of the first temporal moment is especially slow.

This analysis can be extended to higher-order moments. For example, we analyze the error propagation in computing D^2:

$$D^2 = F^2 - x_1 D^1 - \frac{x^2}{2} D^0 + \varepsilon^{22} \tag{A.7}$$

$$= F^2 - x_1 F^1 - \frac{x_1^2}{2} F^0 + x_1^2(\varepsilon^{10} - \varepsilon^{00}) + \frac{x_1^2}{2}(\varepsilon^{00} - \varepsilon^{02}) + x_1(\varepsilon^{12} - \varepsilon^{11}) + \varepsilon^{22}. \tag{A.8}$$

If one donor is used, the fourth, fifth, and sixth terms vanish. If different donors are used, those terms remain and the overall statistical error scales by x_1^2, resulting in even slower statistical convergence for D^2.

It must be noted that this analysis assumes D^0 is constant in time, which is not true for unsteady flows such as RT. Additionally, we do not predict the scalings of the ε^{ij} with space or time. This is why the statistical error plots in Figure 2 do not exhibit the exact scalings derived here. The goal of this analysis is not to provide the scalings but to illustrate the error amplification in higher-order moments and the presence of this extra error in MFM simulations using separate donors.

Appendix B. Rayleigh-Taylor spatial eddy diffusivity moments

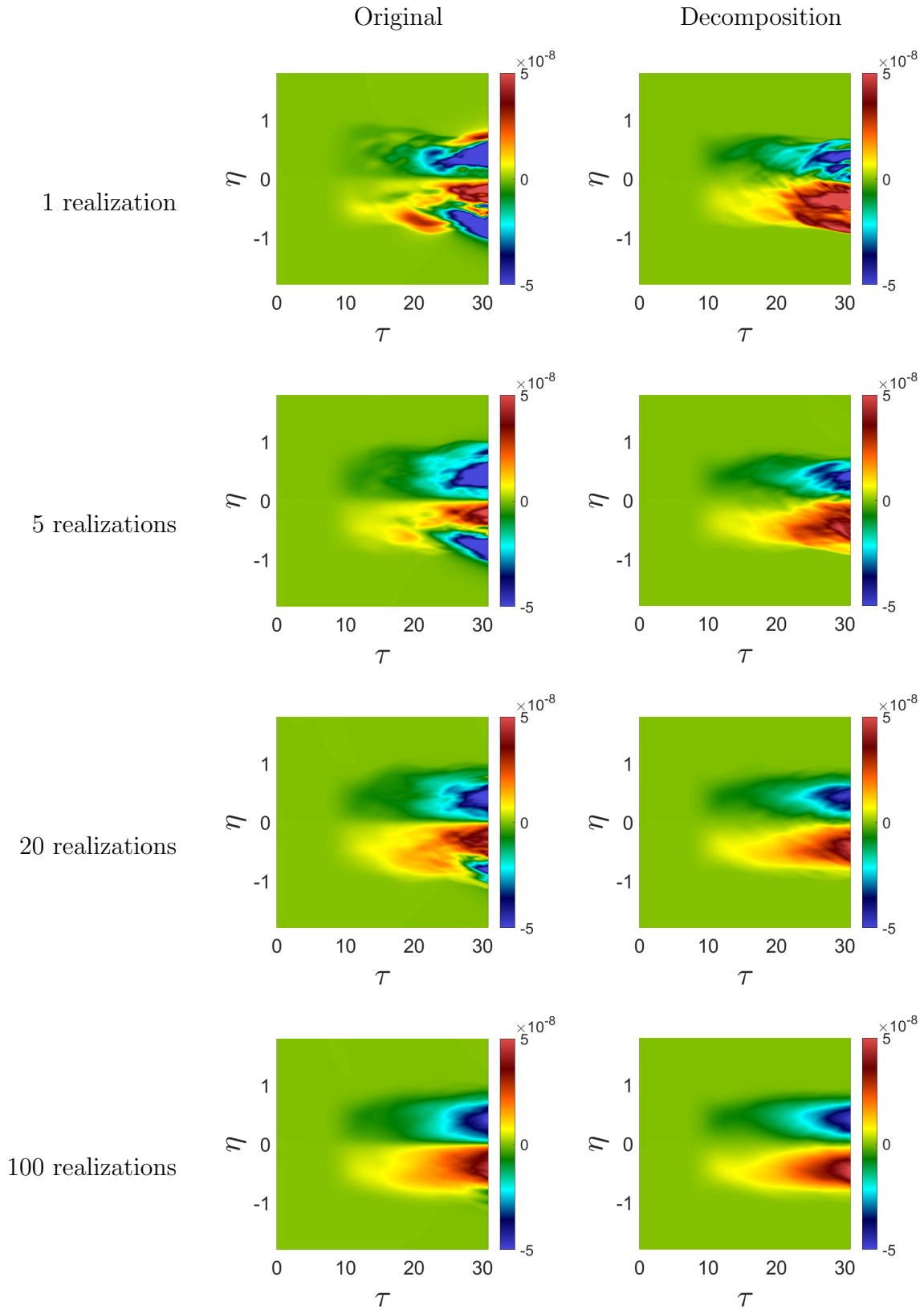

Figure B.9: Convergence of D^{10} (normalized by t) MFM measurement using standard and decomposition methods for RT instability case.

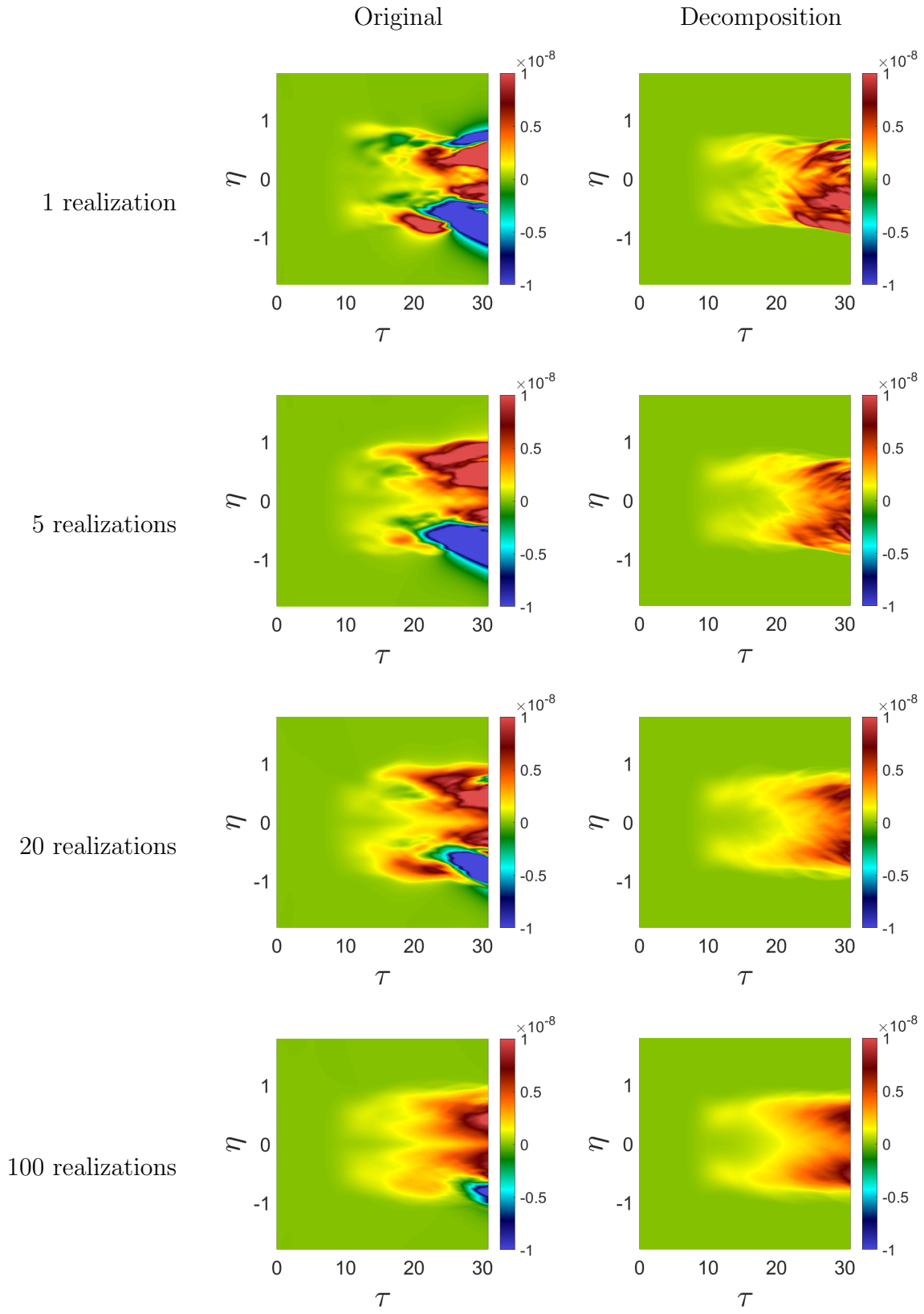

Figure B.10: Convergence of D^{20} (normalized by t) MFM measurement using standard and decomposition methods for RT instability case.

References

[1] A. Mani, D. Park, Macroscopic forcing method: A tool for turbulence modeling and analysis of closures, Phys. Rev. Fluids **6** (2021) 054607.

[2] F. Hamba, Nonlocal expression for scalar flux in turbulent shear flow, Phys. Fluids **16** (2004) 1493–1508.

[3] F. Hamba, Nonlocal analysis of the Reynolds stress in turbulent shear flow, Phys. Fluids **17** (2005) 115102.

[4] J. V. Boussinesq, Essai sur la théorie des eaux courantes, in: Mémoires présentés par divers savants a l'Academie des Sciences de l'Institute National de France, volume XXIII, Impr. Nationale, 1877.

[5] S. Corrsin, Limitations of gradient transport models in random walks and in turbulence, Adv. Geophys. **18** (1975) 25–60.

[6] N. Romanof, Application of the orthonormal expansion of random functions to turbulent diffusion, in: Proceedings of the seventh conference on probability theory: Aug. 29-Sept. 4, 1982, Braşov, Romania, VSP, 1985, p. 493.

[7] R. H. Kraichnan, Eddy viscosity and diffusivity: Exact formulas and approximations, Complex Systems **1** (1987) 805–820.

[8] J. Liu, H. H. Williams, A. Mani, Systematic approach for modeling a nonlocal eddy diffusivity, Phys. Rev. Fluids **8** (2023) 124501.

[9] D. L. O.-L. Lavacot, J. Liu, H. Williams, B. E. Morgan, A. Mani, Non-locality of mean scalar transport in two-dimensional rayleigh–taylor instability using the macroscopic forcing method, Journal of Fluid Mechanics **985** (2024) A47.

[10] N. G. v. Kampen, A power series expansion of the master equation, Can. J. Phys. **39** (1961) 551–567.

[11] D. Park, A. Mani, Direct calculation of the eddy viscosity operator in turbulent channel flow at $\mathrm{Re}_\tau = 180$, arXiv 2108.10898 (2022).

[12] S. H. Bryngelson, F. Schäfer, J. Liu, A. Mani, Fast macroscopic forcing method, J. Comp. Phys. **499** (2024) 112721.

[13] J. Liu, F. Schäfer, S. H. Bryngelson, T. A. Zaki, A. Mani, Adjoint-based computation of nonlocal eddy viscosity in turbulent channel flow, Phys. Rev. Fluids **9** (2024) 094606.

[14] D. Park, J. Liu, A. Mani, Non-Boussinesq effects of eddy viscosity in a separated turbulent boundary layer, in: 34th Symposium on Naval Hydrodynamics, 2022.

[15] W. H. Cabot, A. W. Cook, Reynolds number effects on Rayleigh–Taylor instability with possible implications for type Ia supernovae, Nat. Phys. **2** (2006) 562–568.

[16] B. Morgan, B. Olson, J. White, J. McFarland, Self-similarity of a Rayleigh–Taylor mixing layer at low Atwood number with a multimode initial perturbation, Journal of Turbulence **18** (2017) 973–999.

[17] D. L. Youngs, Numerical simulation of mixing by Rayleigh–Taylor and Richtmyer–Meshkov instabilities, Laser and Particle Beams **12** (1994) 725–750.

[18] B. E. Morgan, B. J. Olson, W. J. Black, J. A. McFarland, Large-eddy simulation and Reynolds-averaged Navier–Stokes modeling of a reacting Rayleigh–Taylor mixing layer in a spherical geometry, Phys. Rev. E **98** (2018) 033111.

[19] B. Morgan, J. Greenough, Large-eddy and unsteady RANS simulations of a shock-accelerated heavy gas cylinder, Shock Waves **26** (2016) 355–383.

[20] J. D. Bender, O. Schilling, K. S. Raman, R. A. Managan, B. J. Olson, S. R. Copeland, C. L. Ellison, D. J. Erskine, C. M. Huntington, B. E. Morgan, et al., Simulation and flow physics of a shocked and reshocked high-energy-density mixing layer, J. Fluid Mech. **915** (2021) A84.

[21] R. W. Sharp, Jr., R. Barton, HEMP advection model, Technical Report, California Univ., Livermore (USA). Lawrence Livermore Lab., 1981.

[22] P. E. Dimotakis, The mixing transition in turbulent flows, J. Fluid Mech. **409** (2000) 69–98.

[23] B. E. Morgan, W. J. Black, Parametric investigation of the transition to turbulence in Rayleigh–Taylor mixing, Physica D: Nonlinear Phenomena **402** (2020) 132223.

[24] R. F. Pawula, Approximation of the linear Boltzmann equation by the Fokker–Planck equation, Phys. Rev. **162** (1967) 186–188.

Atwood effects on nonlocality of the mean scalar transport operator in three-dimensional Rayleigh-Taylor mixing

Dana L. O.-L. Lavacot[a,], Brandon E. Morgan[b], Ali Mani[a]

[a] *Department of Mechanical Engineering, Stanford University, Stanford, CA 94305, USA*

[b] *Lawrence Livermore National Laboratory, Livermore, CA 94550, USA*

Abstract

We assess the importance of nonlocality in modeling mean scalar transport for three-dimensional variable density Rayleigh-Taylor (RT) mixing. Building on the two-dimensional incompressible work of Lavacot et al. [1], we extend the Macroscopic Forcing Method (MFM) to the variable density problem to measure moments of the generalized eddy diffusivity kernel in RT mixing for different Atwood numbers ($A = 0.05, 0.5, 0.8$). We find that as A increases: 1) the eddy diffusivity moments become asymmetric, and 2) the higher-order eddy diffusivity moments become closer in magnitude to the leading-order diffusivity, indicating that nonlocality becomes more important at higher A. There is a particularly strong temporal nonlocality at higher A, suggesting stronger history effects at these A. The implications of these findings for turbulence modeling for finite-Atwood RT are discussed.

Keywords: Turbulence modeling; Rayleigh-Taylor Instability, variable density

1. Introduction

Rayleigh-Taylor (RT) instability occurs when a heavy fluid is accelerated into a lighter fluid through a perturbed interface. Over time, the instability becomes self-similar and results in turbulent mixing. Understanding the effects of this turbulence is critical in engineering design applications, especially for inertial confinement fusion (ICF). In ICF, a plastic ablator is accelerated into deuterium gas to achieve high pressures and, consequently, ignition. If there are perturbations the ICF capsule surface, which can happen due to imperfections in manufacturing, RT instability can be triggered and cause premature mixing that ultimately reduces energy output [2].

In designing experiments for ICF, it is crucial to accurately predict the turbulent mixing in simulations. High-fidelity approaches such as direct numerical simulations (DNS) and large eddy simulations (LES) have been used to accurately predict turbulent mixing in RT instability [3–5]. However, the fine grids required to resolve turbulent scales make them prohibitively expensive for the iterative design process, in which thousands of simulations must be run. A more appealing and computationally feasible approach is simulation of the Reynolds-Averaged Navier-Stokes (RANS) equations, which requires resolution of only the macroscopic scales. In RANS simulations, only the mean quantities are evolved, so models are required to approximate the physics of the unresolved

Email address: dlol@stanford.edu (Dana L. O.-L. Lavacot)

scales. It is then crucial in the RANS approach to use accurate models for the unclosed terms.

In this work, we focus on the unclosed turbulent species flux (TSF) in the mean scalar transport equation. A common closure for this term is a gradient-diffusion approximation, which assumes the TSF depends only on local gradients of the mean scalar field. This is the closure used in popular models for RT mixing such as the k–ϵ model [6] (modified by Gauthier and Bonnet [7] for RT) and the k–L model [8]. However, the gradient-diffusion closure has been shown to not be sufficient for modeling scalar transport in RT mixing [9, 10]. Alternative models include those that use transport equations for the TSF [11] and those based on two-point correlations [12–14]. While these models address nonlocal effects in RT mixing, they do so without directly examining the nonlocality of the closure operator.

Traditional approaches towards studying nonlocality usually involve examination of two-point correlations. Indeed, there are extensive studies on two-point correlations for RT mixing [15–17], so nonlocality of the instability is well-known. However, for modeling, it is also valuable to directly examine the nonlocality of the closure operator. Through this lens, we can directly discern what form a model that correctly captures this nonlocality should take.

Nonlocality of the eddy diffusivity has been studied in a previous work [1] for two-dimensional (2D) RT mixing in the Boussinesq limit ($A = 0.05$). In that work, the Macroscopic Forcing Method (MFM) [18] was used to measure moments of the generalized eddy diffusivity kernel, which describes the nonlocal dependence of the turbulent flux on mean gradients. MFM is similar to the Green's function approach described by Hamba [19] for determining the exact nonlocal eddy diffusivity but also allows for polynomial forcings that enable measurement of eddy diffusivity moments. Measuring the moments is more efficient than computing the full kernel, which becomes expensive for unsteady problems with large macroscopic spaces, like RT mixing. Lavacot et al. [1] found through MFM measurements of eddy diffusivity moments that nonlocality is important for modeling in the low-Atwood, 2D problem.

The goal of the present work is to extend MFM analysis to turbulent three-dimensional (3D) RT mixing at multiple higher Atwood numbers. The extension to 3D is certainly necessary for investigation of truly turbulent RT. Additionally, simulations of higher Atwood numbers allow for the investigation of variable density effects on nonlocality. It is known that the behavior of the instability differs between the variable density regime and the Boussinesq limit. Particularly, asymmetry in the mixing layer arises at higher Atwood numbers, which also leads to asymmetries in turbulent statistics, as shown by Livescu et al. [20]. Thus, one purpose of this study is to investigate the strength of the dependence of nonlocality in RT mixing on Atwood number. Ultimately, findings from this study will inform development of more accurate turbulence models for variable density RT mixing that incorporate nonlocality and its dependence on Atwood number.

This work is organized as follows. Methods of this work are presented in §2, in which we describe the governing equations, a brief overview of RT physics, our method of numerical solution, and the generalized eddy diffusivity, MFM, and matched moment inverse for analysis of nonlocality. Results

are presented in §3, in which we show and analyze the eddy diffusivity moments measured using MFM. Finally, we discuss the results and implications for modeling in the Conclusion in §4.

2. Methods

2.1. Governing equations

RT mixing is governed by the compressible Navier-Stokes equations:

$$\frac{\partial \rho}{\partial t} = -u_j \frac{\partial \rho}{\partial x_j}, \tag{1}$$

$$\frac{\partial \rho Y_\alpha}{\partial t} = -\frac{\partial}{\partial x_j}\left(\rho u_j Y_\alpha - \rho D_\alpha \frac{\partial Y_\alpha}{\partial x_j}\right), \tag{2}$$

$$\frac{\partial \rho u_j}{\partial t} = -\frac{\partial}{\partial x_i}\left(\rho u_i u_j + p\delta_{ij} - \tau_{ij}\right) + \rho g_i, \tag{3}$$

$$\frac{\partial E}{\partial t} = -\left(\rho u_i \left(E + p\right) - u_j \tau_{ij} - q_i\right) + \rho g_j u_j. \tag{4}$$

Here, ρ is density, u_i is velocity, Y_α is the mass fraction of species α, D_α is the diffusivity of species α, p is pressure, δ_{ij} is the Kronecker delta, $\tau_{ij} =$ is the viscous stress, g_i is gravitational acceleration (in this work, $\mathbf{g} = (0, -g, 0)^T$), $E = \rho\left(e + \frac{1}{2}u_j u_j\right)$ is the total energy, and q_i is the energy flux. The viscous stress is

$$\tau_{ij} = \mu\left(\frac{\partial u_i}{\partial x_j} + \frac{\partial u_j}{\partial x_i}\right) + \left(\beta - \frac{2}{3}\mu\right) u_j u_j, \tag{5}$$

where μ is the molecular viscosity and β is the bulk viscosity. The energy flux is

$$q_i = -\kappa \frac{\partial T}{\partial x_i}, \tag{6}$$

where T is temperature. Pressure and temperature are determined using the ideal gas law:

$$p = \rho\left(\gamma - 1\right)e, \quad T = \left(\gamma - 1\right)\frac{e}{R}, \tag{7}$$

where γ is the ratio of specific heats $\frac{c_p}{c_v}$ and R is the specific constant.

In the problem studied here, two miscible species are considered. The heavy species is subscripted H, and the light species is subscripted L.

2.2. RT mixing and self-similarity

A density difference is required between two fluids for RT mixing to occur. This density difference can be expressed nondimensionally as the Atwood number:

$$A = \frac{\rho_H - \rho_L}{\rho_H + \rho_L}, \tag{8}$$

where ρ_H is the density of the heavy fluid, and ρ_L is the density of the light fluid.

As the instability develops, bubbles rise into the heavy fluid, and spikes sink into the light fluid. Over time, secondary Kelvin-Helmholtz instabilities are triggered, and the flow transitions into

turbulence. In this turbulent state, RT instability becomes self-similar, and the growth of the bubbles and spikes are quadratic in time:

$$h_b \approx \alpha_b A g t^2, \quad h_s \approx -\alpha_s A g t^2, \tag{9}$$

where h_b and h_s are the bubble and spike heights, respectively, and α_b and α_s are the bubble and spike growth rates, respectively. Based on the bubble height, we define a self-similar variable in space $\eta \equiv (y - \frac{1}{2})/h_b$, for y defined between 0 and 1. The sum of h_b and h_s give the total mixing layer width, which can be expressed as

$$h \approx \alpha A g t^2, \tag{10}$$

where $\alpha = \alpha_b + \alpha_s$. At low A, $h_b \approx h_s$. Increasing A increases the asymmetry of the mixing layer [20, 21] as the spikes sink faster than the bubbles rise. Thus, for finite A, $h > h_b$. In this work, the growth of the bubbles is used for self-similar analysis rather than the total mixing layer growth rate α, since the latter varies significantly across Atwood numbers [22].

Using the analytical derivation of the mixing width from Ristorcelli and Clark [16], Cabot and Cook [4] defines the bubble growth rate as

$$\alpha_b = \frac{\dot{h_b}^2}{4 A g h_b}, \tag{11}$$

where $\dot{h_b}$ is the rate of change of h_b in time. We use this definition to observe the growth rate over time and assess convergence to self-similarity. In the self-similar regime, α_b should converge to a constant value over time.

For self-similar analysis, we use the definition of α_b by Livescu et al. [20]:

$$\alpha_b = \left(\frac{h_b(t)^{1/2} - h_b(t_0)^{1/2}}{(Ag)^{1/2}(t - t_0)} \right)^2 \tag{12}$$

where t_0 is an arbitrary time during the self-similar growth of the mixing layer. This definition is preferable for self-similar fits and normalizations, since it avoids temporal derivatives of the mixing width, which is not smooth in time due to statistical error.

The bubble height can be computed from mass fraction profiles by taking it as the distance from the centerline of the domain to where the mean mass fraction of the light fluid is 0.999. The RT instability can be considered self-similar when this $h_{b,99}$ becomes quadratic in time.

Another metric for self-similarity is the mixedness parameter, defined as

$$\phi \equiv 1 - 4 \frac{\int \widetilde{Y_H'' Y_H''} dy}{\int \widetilde{Y_H} \widetilde{Y_L} dy}, \tag{13}$$

where Y_H is the mass fraction of the heavy fluid, and $Y_L = 1 - Y_H$ is the mass fraction of the light fluid. For self-similar RT mixing, ϕ is expected to converge to a steady-state value.

Additionally, transition to self-similar turbulence can be assessed by examining the Reynolds number. The Taylor microscale Reynolds number is defined as

$$Re_T = \frac{k^{1/2}\lambda}{\nu}, \tag{14}$$

where $k = \frac{1}{2}\widetilde{u_i'' u_i''}$, and

$$\lambda = \sqrt{\frac{10\nu L}{k^{1/2}}}. \tag{15}$$

L is a turbulent length scale, which can be approximated as $\frac{1}{5}$ of the mixing width [9]. The large scale Reynolds number [4] is defined as

$$Re_L = \frac{h_{99}\dot{h}_{99}}{\nu}, \tag{16}$$

where h_{99} is the total mixing width defined as the distance between the locations of mass fractions 0.001 and 0.999. The RT mixing is considered turbulent and self-similar when $Re_T > 100$ and $Re_L > 10,000$ [23].

2.3. Modeling the mean scalar transport operator

To obtain the mean scalar transport equation, the Reynolds ($\langle q \rangle$) and Favre ($\widetilde{q}$) averages of quantity q are defined:

$$\langle q \rangle = \frac{1}{N}\sum_i^N q_i, \tag{17}$$

$$\widetilde{q} = \frac{\langle \rho q \rangle}{\langle \rho \rangle}, \tag{18}$$

where N is the number of ensembles. In the case where the flow is homogeneous (in space and/or time), the homogeneous directions may be included in these ensembles. For the RT mixing problem studied here, the homogeneous directions are x and z, so averages are performed over x, z, and realizations. Fluctuations from the Reynolds and Favre means are denoted as q' and q'', respectively, so

$$q = \langle q \rangle + q' = \widetilde{q} + q''. \tag{19}$$

Substituting the Favre decomposition for velocity and mass fraction into Equation 2 and taking its Reynolds average results in the mean scalar transort equation for compressible flow:

$$\frac{\partial \langle \rho \rangle \widetilde{Y_H}}{\partial t} = -\frac{\partial}{\partial y}\left(\langle \rho \rangle \widetilde{v}\widetilde{Y_H} + \widetilde{\rho v'' Y_H''} - \langle \rho \rangle D_H \frac{\partial \widetilde{Y_H}}{\partial y} \right). \tag{20}$$

The turbulent species flux $\langle -\rho v'' Y_H'' \rangle$ is unclosed and needs to be modeled.

The turbulent species flux can be exactly modeled as

$$\langle -\rho v'' Y_H'' \rangle (y,t) = \langle \rho \rangle \int D\left(y, y', t, t'\right) \left. \frac{\partial \widetilde{Y_H}}{\partial y} \right|_{y',t'} dy' dt', \tag{21}$$

where D is the eddy diffusivity kernel. This is an extension of the formulation for incompressible flow described in Kraichnan [24], Hamba [19], and Mani and Park [18] . This is a nonlocal formulation, in that it expresses the TSF based not only on mean scalar gradients at the points in space and time (y and t) it is measured at, but also all other points in space and time (y' and t').

An exact model for the turbulent species flux requires full characterization of the eddy diffusivity kernel. This has been done for simpler flows in the works of Hamba [25], Hamba [19], and Park and Mani [26]. However, computation of the kernel is computationally expensive, since it requires simulations on the order of the number of points in macroscopic space. On top of this, chaotic flows, like RT mixing, require many realizations for statistical convergence.

The eddy diffusivity kernel can instead be approximated by its moments. This can be done by employing a Taylor series expansion of the mean scalar gradient about y and t, which results in the Kramers-Moyal-like expansion:

$$\langle -\rho v'' Y_H'' \rangle (y,t) = \langle \rho \rangle D^{00}(y,t) \frac{\partial \widetilde{Y_H}}{\partial y} + \langle \rho \rangle D^{10}(y,t) \frac{\partial^2 \widetilde{Y_H}}{\partial y^2} + \langle \rho \rangle D^{01}(y,t) \frac{\partial^2 \widetilde{Y_H}}{\partial t \, \partial y} \tag{22}$$

$$+ \langle \rho \rangle D^{20}(y,t) \frac{\partial^3 \widetilde{Y_H}}{\partial y^3} + \langle \rho \rangle D^{11}(y,t) \frac{\partial^2 \widetilde{Y_H}}{\partial t y^2} + \langle \rho \rangle D^{02}(y,t) \frac{\partial^2 \widetilde{Y_H}}{\partial t^2 y} + \dots \tag{23}$$

where D^{mn} are the eddy diffusivity moments. The first index m indicates space and the second index n is time. The moments are defined as

$$D^{00}(y,t) = \int \int D(y, y', t, t') dy' dt', \tag{24}$$

$$D^{10}(y,t) = \int \int (y' - y) D(y, y', t, t') dy' dt', \tag{25}$$

$$D^{01}(y,t) = \int \int (t' - t) D(y, y', t, t') dy' dt', \tag{26}$$

$$D^{20}(y,t) = \int \int \frac{(y' - y)^2}{2} D(y, y', t, t') dy' dt', \tag{27}$$

$$\vdots \tag{28}$$

These moments are more computationally feasible to compute than the full kernel. To compute the moments, the process for which will be described shortly, one equation per moment needs to be added to the suite of equations being solved in a simulation. Though the number of operations increases as more moments are computed, only one simulation needs to be run to compute all moments. Statistically converged moments require multiple simulations; in this work, it is found

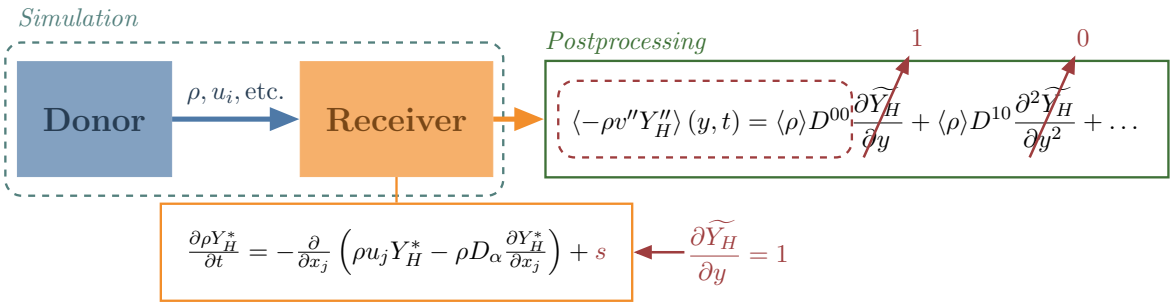

Figure 1: MFM pipeline illustrating measurement of D^{00} for the mean scalar transport problem. Asterisks indicate receiver variables that are macroscopically forced in the receiver simulation and are not necessarily equivalent to the donor variables.

Moment	$\frac{\partial \widetilde{Y_H}}{\partial y}$
D^{00}	1
D^{01}	t
D^{10}	$y - \frac{1}{2}$
D^{02}	$\frac{1}{2}t^2$
D^{11}	$(y - \frac{1}{2})t$
D^{20}	$\frac{1}{2}(y - \frac{1}{2})^2$

Table 1: Mean mass fraction gradients forced for each eddy diffusivity moment D^{mn}.

that $\mathcal{O}(10)$ simulations are needed for statistical convergence sufficient for analysis, which is much lower than what is needed to compute the full kernel.

While the eddy diffusivity moments are locally defined (they are functions of y and t only), higher-order moments contain information about the nonlocality of the full kernel. The leading-order moment D^{00} is purely local, and truncation to the leading-order term is the gradient-diffusion or Boussinesq approximation. The goal of this work is to determine the importance of the higher-order terms and, therefore, the nonlocality of the mean scalar transport operator for the RT mixing cases studied here. In this way, measuring the eddy diffusivity moments is a more computationally efficient but still insightful way to assess the nonlocality of the closure operator.

2.4. Measuring the eddy diffusivity moments using the Macroscopic Forcing Method

In this work, MFM is used to measure the eddy diffusivity moments. The MFM pipeline is conceptually illustrated in Figure 1. The method involves two sets of equations, called the *donor* and the *receiver*, which are solved simultaneously in a simulation. The donor contains the full set of model equations (in this case, the Navier-Stokes equations) and gives quantities necessary for solution of the receiver, which has the forced equations. The forcings for each receiver equation are chosen to achieve certain mean scalar gradients that allow for the probing of each eddy diffusivity

moment. For example, to compute D^{00}, $\frac{\partial \widetilde{Y_H}}{\partial y} = 1$ can be chosen in a numerical simulation. In Equation 23, this choice causes the higher-order terms to drop, and measurement of $\langle -\rho v'' Y_H'' \rangle$ gives D^{00}. The MFM pipeline illustrating this example is in Figure 1. Similarly, higher-order moments can be determined by choosing different polynomials for $\frac{\partial \widetilde{Y_H}}{\partial y}$. Table 1 lists the mean scalar gradients chosen to obtain each moment.

In Figure 1, the standard MFM is shown, in which forcings are directly applied to the full scalar field. In this work, the Decomposition MFM [] is used instead, in which fluctuations of the mass fraction field are simulated and the forcings are semi-analytically applied. To formulate the forced equations, Y_H'' is first written as a Kramers-Moyal expansion analagous to Equation 23:

$$Y_H'' = c^{00}\frac{\partial \widetilde{Y_H}}{\partial y} + c^{10}\frac{\partial^2 \widetilde{Y_H}}{\partial y^2} + c^{01}\frac{\partial^2 \widetilde{Y_H}}{\partial t\,\partial y} + c^{20}\frac{\partial^3 \widetilde{Y_H}}{\partial y^3} + c^{11}\frac{\partial^2 \widetilde{Y_H}}{\partial t y^2} + c^{02}\frac{\partial^2 \widetilde{Y_H}}{\partial t^2 y} + \dots \tag{29}$$

Substituting this expansion and the forced mean mass fractions derived from Table 1 into Equation 2 gives the following equations for each c^{mn}:

$$\frac{D\rho c^{00}}{Dt} = \frac{\partial}{\partial x_j}\rho D_H \frac{\partial}{\partial x_j} c^{00} - \rho u_2 + \frac{\partial}{\partial y}\rho D_H + s^{00}, \tag{30}$$

$$\frac{D\rho c^{10}}{Dt} = \frac{\partial}{\partial x_j}\rho D_H \frac{\partial}{\partial x_j} c^{10} - \rho u_2 c^{00} + \rho D_H + \rho D_H \frac{\partial}{\partial y} c^{00} + \frac{\partial}{\partial y}\rho D_H c^{00} + s^{10}, \tag{31}$$

$$\frac{D\rho c^{01}}{Dt} = \frac{\partial}{\partial x_j}\rho D_H \frac{\partial}{\partial x_j} c^{01} - \rho c^{00} - \rho y + s^{01}, \tag{32}$$

$$\frac{D\rho c^{20}}{Dt} = \frac{\partial}{\partial x_j}\rho D_H \frac{\partial}{\partial x_j} c^{20} + \rho D_H c^{00} + \rho D_H \frac{\partial}{\partial y} c^{10} + \frac{\partial}{\partial y}\rho D_H c^{10} + s^{20}, \tag{33}$$

$$\frac{D\rho c^{11}}{Dt} = \frac{\partial}{\partial x_j}\rho D_H \frac{\partial}{\partial x_j} c^{11} - \rho c^{10} - \rho v c^{01} + \rho D_H \frac{\partial}{\partial y} c^{01} + \frac{\partial}{\partial y}\rho D_H c^{01} + \rho\left(\frac{1}{2}y^2 - \frac{1}{8}\right) + s^{11}, \tag{34}$$

$$\frac{D\rho c^{02}}{Dt} = \frac{\partial}{\partial x_j}\rho D_H \frac{\partial}{\partial x_j} c^{02} - \rho c^{01} + s^{02}, \tag{35}$$

where each forcing s^{mn} enforces the x-z mean of c^{mn} to be zero. To obtain the eddy diffusivity moments, the turbulent species flux based on the Y_H'' from each equation is computed in postprocessing:

$$\langle -\rho v'' c^{mn} \rangle = \langle \rho \rangle D^{mn}. \tag{36}$$

In the numerical simulation, solutions to the donors (Equations 1-4) are given to these receiver equations, which are solved alongside the donors. Thus, if the cost to solve the suite of donor equations is N, the cost of MFM for one realization of the eddy diffusivity moments examined in this work is approximately $2N$. Of course, this cost increases as more moments are measured, but it has been found that not many moments are required to characterize the nonlocality of the eddy diffusivity kernel [1, 27], making the MFM measurement of moments relatively efficient and useful.

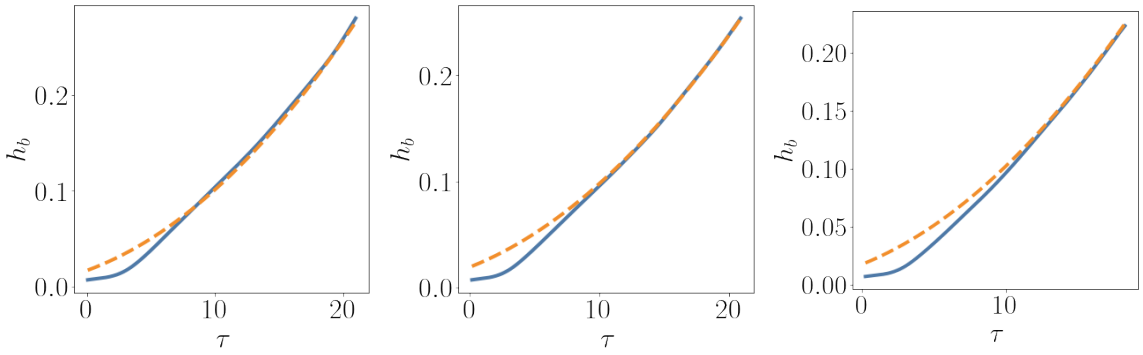

(a) $A = 0.05$ **(b)** $A = 0.5$ **(c)** $A = 0.8$

Figure 2: h_b from simulations (solid blue) and fitted h_b (dashed orange).

2.5. Self-similar normalization

Lavacot et al. [1] presents a self-similar analysis that results in normalizations for the turbulent species flux and eddy diffusivity moments. This analysis can be applied directly to the variable density RT mixing studied here and is extended to D^{11} and D^{02}, which have not been studied previously:

$$\widehat{F} = \frac{F}{\alpha^* Ag(t - t_0^*)}, \tag{37}$$

$$\widehat{D^{00}} = \frac{D^{00}}{(\alpha^* Ag)^2 (t - t_0^*)^3}, \tag{38}$$

$$\widehat{D^{01}} = \frac{D^{01}}{(\alpha^* Ag)^2 (t - t_0^*)^4}, \tag{39}$$

$$\widehat{D^{10}} = \frac{D^{10}}{(\alpha^* Ag)^3 (t - t_0^*)^5}, \tag{40}$$

$$\widehat{D^{02}} = \frac{D^{02}}{(\alpha^* Ag)^2 (t - t_0^*)^5}, \tag{41}$$

$$\widehat{D^{11}} = \frac{D^{11}}{(\alpha^* Ag)^3 (t - t_0^*)^6}, \tag{42}$$

$$\widehat{D^{20}} = \frac{D^{20}}{(\alpha^* Ag)^4 (t - t_0^*)^7}, \tag{43}$$

where α^* is the growth rate defined in Equation 12, and t_0^* is a fitted time origin based on the measured bubble height. Figure 2 shows the bubble height measured from the simulations and the determined fits.

2.6. Matched Moment Inverse

Truncation of Equation 23 represents an approximate model for the turbulent species flux. However, a property of the Kramers-Moyal expansion is that it does not converge with finite terms.

Instead, a systematic method for constructing a model using eddy diffusivity moments is presented here. With the Matched Moment Inverse (MMI), the goal is to match the shape of the eddy

diffusivity kernel using its moments. This is achieved by determining coefficients $a^{mn}(y,t)$ for the implicit model form:

$$\left[1 + a^{10}\frac{\partial}{\partial y} + a^{01}\frac{\partial}{\partial t} + a^{20}\frac{\partial^2}{\partial y^2} + ...\right]\langle -\rho v'' Y_H''\rangle = a^{00}\langle\rho\rangle\frac{\partial\widetilde{Y_H}}{\partial y}. \tag{44}$$

The operator on the left hand side can be expanded based on which moments are used; a^{mn} corresponds to using D^{mn}. The model coefficients are determined numerically using MFM simulation data. For example, if D^{00}, D^{01}, D^{10}, and D^{20} are used, the following system is solved for a^{00}, a^{01}, a^{10}, and a^{20}:

$$\left[1 + a^{10}\frac{\partial}{\partial y} + a^{01}\frac{\partial}{\partial t} + a^{20}\frac{\partial^2}{\partial y^2}\right]F^{00} = a^{00}, \tag{45}$$

$$\left[1 + a^{10}\frac{\partial}{\partial y} + a^{01}\frac{\partial}{\partial t} + a^{20}\frac{\partial^2}{\partial y^2}\right]F^{10} = a^{00}\left(y - \frac{1}{2}\right), \tag{46}$$

$$\left[1 + a^{10}\frac{\partial}{\partial y} + a^{01}\frac{\partial}{\partial t} + a^{20}\frac{\partial^2}{\partial y^2}\right]F^{01} = a^{00}t, \tag{47}$$

$$\left[1 + a^{10}\frac{\partial}{\partial y} + a^{01}\frac{\partial}{\partial t} + a^{20}\frac{\partial^2}{\partial y^2}\right]F^{20} = a^{00}\frac{1}{2}\left(y - \frac{1}{2}\right)^2. \tag{48}$$

The above is demonstrated for spatio-temporal variables for simplicity, but the analysis presented here is done in self-similar space. The self-similar implicit model form is

$$\left[1 + \widehat{a^{10}}\frac{\partial}{\partial\eta} + \widehat{a^{01}}\left(1 - 2\eta\frac{\partial}{\partial\eta}\right) + \widehat{a^{20}}\frac{\partial^2}{\partial\eta^2} + ...\right]\widehat{F} = \widehat{a^{00}}\langle\rho\rangle\frac{\partial\widetilde{Y_H}}{\partial\eta}, \tag{49}$$

where the self-similar coefficients are

$$\widehat{a^{00}} = \frac{1}{\alpha^{*2}A^2g^2(t-t^*)^3}a^{00}, \tag{50}$$

$$\widehat{a^{01}} = \frac{1}{t-t^*}a^{01}, \tag{51}$$

$$\widehat{a^{10}} = \frac{1}{\alpha^*Ag(t-t^*)^2}a^{10}, \tag{52}$$

$$\widehat{a^{20}} = \frac{1}{\alpha^{*2}A^2g^2(t-t^*)^4}a^{20}. \tag{53}$$

2.7. Numerical solution to the donor equations

Pyranda, a Python wrapper for *Miranda*, is used to solve Equations 1-4. *Miranda* is a hydrodynamics code developed at Lawrence Livermore National Laboratory [28, 29]. It uses fourth-order Runge-Kutta in time and a tenth-order compact differencing scheme in space. Due to this high-order spatial scheme, Pyranda uses artificial fluid properties for stability. Particularly, artificial molecular viscosity, bulk viscosity, thermal conductivity, and species diffusivity are computed and added to the physical fluid properties to dampen numerical instabilities that may arise due to the high-order numerics. Details on the artificial fluid method can be found in Cook [30].

Nondimensional number	$A = 0.05$	$A = 0.5$	$A = 0.8$
$Ma_{\max}$	0.05	0.2	0.4
Re_T, Pe_T	126	124	138
Re_L, Pe_L	1.46×10^4	1.40×10^4	1.57×10^4

Table 2: Values of nondimensional numbers at the end of the simulation for each A case. $Ma_{\max}$ is reported from one realization. The Reynolds and Peclet numbers are computed from averaged realizations.

To prevent the numerical diffusion from dominating the physical turbulent diffusion, the numerical Grashof number is kept small. This Grashof number is defined as

$$Gr = \frac{-2gA\Delta^3}{\nu^2}. \tag{54}$$

where $\Delta = \Delta_x = \Delta_y = \Delta_z$ is the grid spacing. In line with the findings of Morgan and Black [31], $Gr = 12$ is used to keep numerical diffusion small but still allow turbulence to develop before the edges of the mixing layer reach the domain boundaries.

The other relevant nondimensional numbers of the RT mixing problem are the Mach number (Ma), Peclet number (Pe), and Schmidt number (Sc):

$$Ma = \frac{u}{c}, \tag{55}$$

$$Pe_T = Re_T Sc, \tag{56}$$

$$Pe_L = Re_L Sc, \tag{57}$$

$$Sc = \frac{\nu}{D_M}. \tag{58}$$

Here, c is the speed of sound and is set by the heat capacity ratio γ, which is 5/3 in the simulations presented here. The Schmidt is chosen to be unity. The Peclet numbers are determined by the Reynolds and Schmidt numbers, and the Reynolds numbers are set through the numerical Grashof number, which fixes ν through choice of g, A, and Δ. Values of these nondimensional numbers at the final timesteps of the simulations are listed in Table 2.

The plots of Re in Figure 3 show that the flows in all the A cases studied here develop past the critical Reynolds numbers from Dimotakis [23]. These plots are given in nondimensional time $\tau = t/\tau_0$, where $\tau_0 = \sqrt{h_0/Ag}$, and h_0 is the dominant length scale determined by the peak of the initial perturbation spectrum. The critical Re are reached at approximately $\tau = 19$, $\tau = 19$, and $\tau = 16$ for $A = 0.05$, $A = 0.5$, and $A = 0.8$, respectively.

The simulation domain is $0.5 \times 1.0 \times 0.5$ cm, so the length in y is twice the lengths in x and z, and the grid is $512 \times 1024 \times 512$ cells. The domain is periodic in x and z, and no slip and no penetration conditions are applied in y. Sponge layers are applied to the velocity and density fields at the boundaries in y to prevent growth of acoustic waves that arise from the high-order numerics. Specifically, a smoothing filter described in Cook [30] is applied across the profile shown in Figure 5.

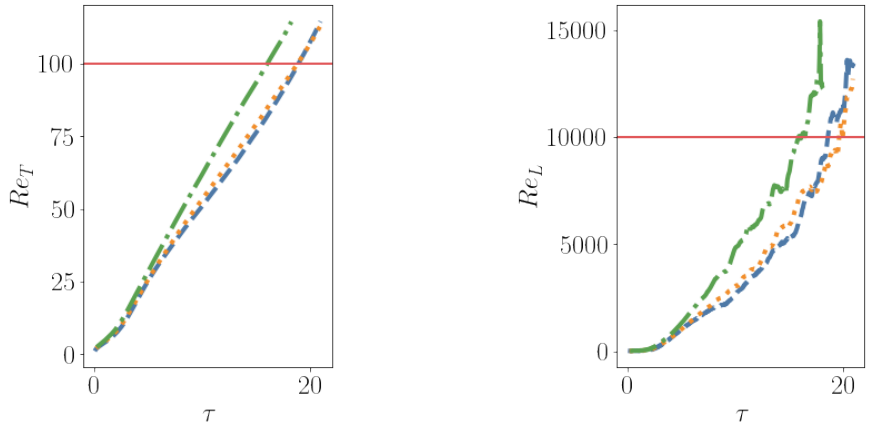

(a) **(b)**

Figure 3: Reynolds numbers over time for each of the A cases.

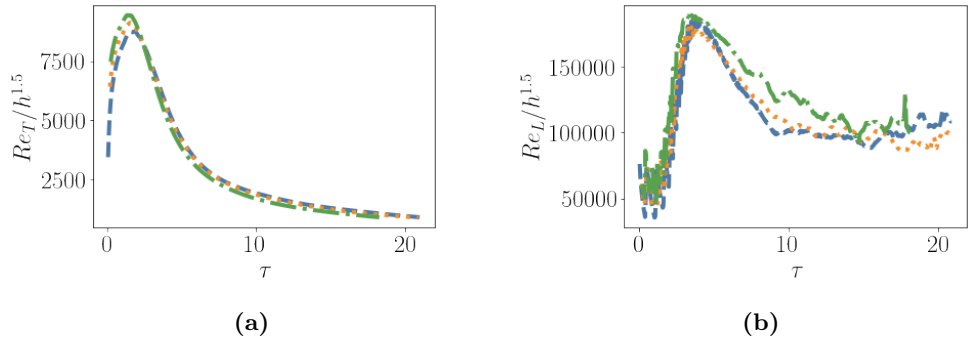

(a) **(b)**

Figure 4: Reynolds numbers over time for each of the A cases, scaled by $h^{1.5}$.

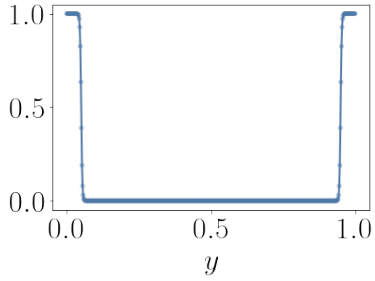

Figure 5: Sponge layer profile for boundaries in y in 3D RT simulation.

The mass fraction profile is initialized as a tanh profile with approximately ten cells across the interface. A multi-mode perturbation is added at the interface:

$$E_0 = \frac{\Delta/2}{\kappa_{\max} - \kappa_{\min} + 1}, \tag{59}$$

$$\xi(x,z) = E_0 \sum_{k=\kappa_{\min}}^{\kappa_{\max}} \left(\cos\left(2\pi k_x x + \phi_{1,k}\right) + \sin\left(4\pi k_x x + \phi_{2,k}\right)\right)\left(\cos\left(2\pi k_z z + \phi_{3,k}\right) + \sin\left(4\pi k_z z + \phi_{4,k}\right)\right), \tag{60}$$

$$Y_H(x,y,z) = \frac{1}{2}\left(1 + \tanh\left(\frac{y - L_y/2 - \xi}{2\Delta}\right)\right), \tag{61}$$

where $\phi_{1,k}$, $\phi_{2,k}$, $\phi_{3,k}$, and $\phi_{4,k}$ are phase shift vectors randomly taken from a uniform distribution. The minimum and maximum wavenumbers are set to $\kappa_{\min} = 8$ and $\kappa_{\max} = 64$, respectively. Density is computed from this initial mass fraction profile as $\rho_H Y_H + \rho_L Y_L$. The light fluid density is set to unity for all simulations, and the heavy fluid density is determined from this and the Atwood number. Pressure is initialized as a hydrostatic pressure based on the initial density field, $p = \rho g\left(y - \frac{1}{2}\right) + 1$. The velocity field and receiver fields are initially zero.

The simulation is stopped when h_{99} reaches 0.5. This allows the mixing layer to evolve sufficiently and become self-similar and turbulent while avoiding interference from the top and bottom walls.

For statistical convergence, nine realizations are run for each A case. Different realizations are achieved by setting different random seeds, resulting in different random perturbations at the interface of the two fluids. Example contours of density and mach number from one realization of each Atwood number case are shown in Figures 6 and 7, respectively.

Figure 8 shows self-similar metrics for the donor simulations, averaged over all realizations for each A case. The $A = 0.05$ case appears to be safely in the self-similar regime, as its ϕ seems converged to approximately 0.8. Its α_b is also somewhat converged to approximately 0.03, which is within the range reported in the literature [4, 20]—it is not perfectly flat, but this is likely due to statistical error in h and its time derivative. The $A = 0.5$ case also appears to be in the self-similar regime, having converged to similar values of α_b and ϕ as the $A = 0.05$ case, but the former does not appear to be as far into the self-similar state as the latter. The $A = 0.8$ case gives α_b and ϕ that are only beginning to converge, indicating that this case is just barely in the self-similar regime. Nevertheless, this case gives an α_b close to the other cases and can be used to make quadratic fits for h_b needed for self-similar analysis.

3. Results

3.1. Eddy diffusivity moments

Figure 9 shows the eddy diffusivity moments for each Atwood number. First, we observe some expected behavior at the lowest Atwood number:

1. D^{00} is the largest in magnitude. It is also symmetric and positive.

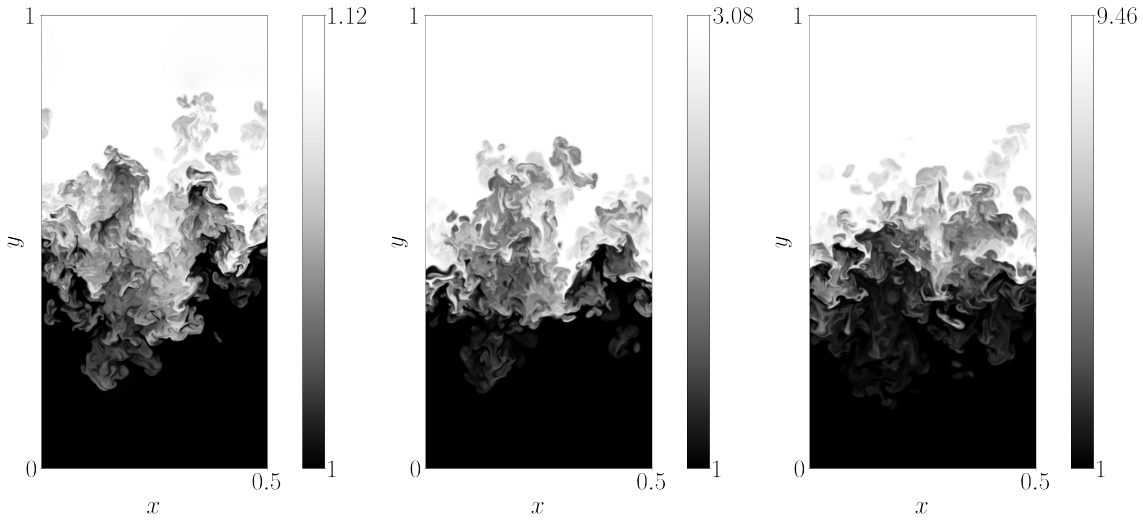

(a) $A = 0.05$ **(b)** $A = 0.5$ **(c)** $A = 0.8$

Figure 6: Contours of density for each A case.

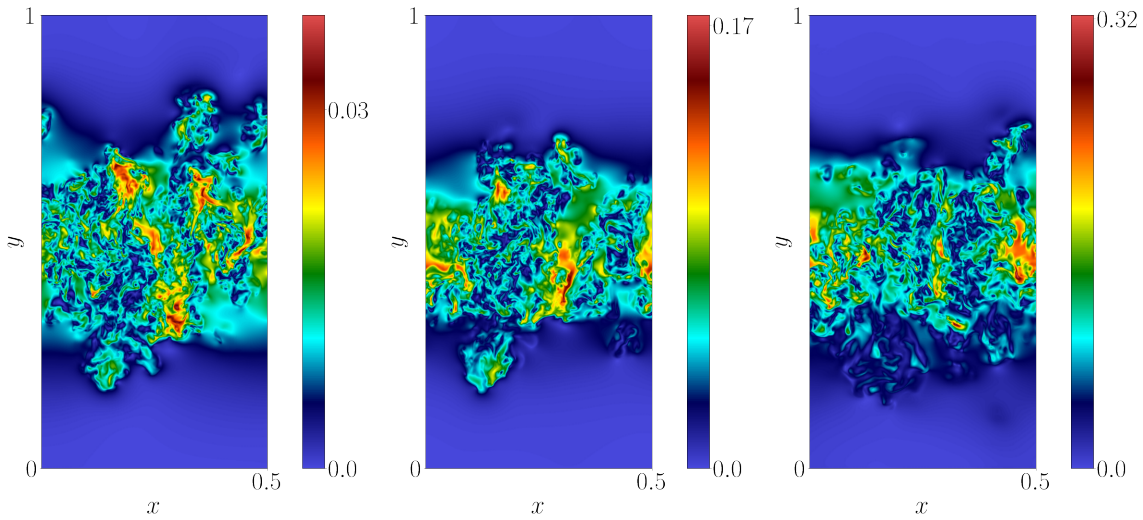

(a) $A = 0.05$ **(b)** $A = 0.5$ **(c)** $A = 0.8$

Figure 7: Contours of mach number for each A case.

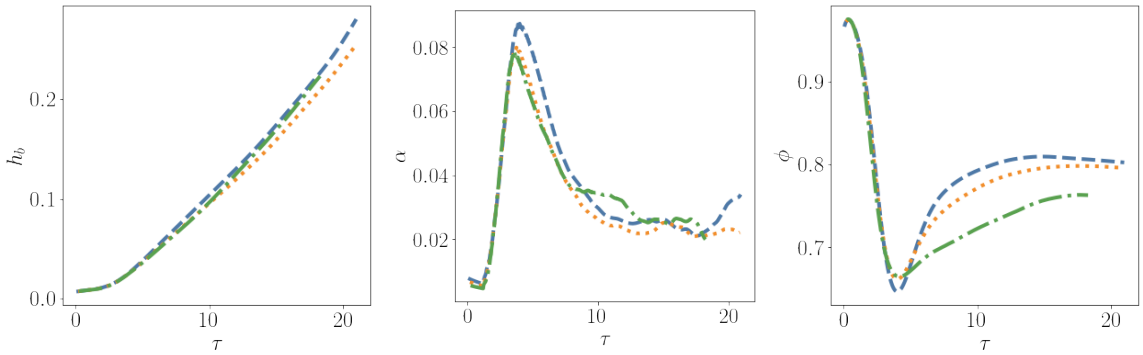

(a) Mixing width **(b)** Mixing width growth rate **(c)** Mixedness

Figure 8: Self-similarity metrics for each A case. Dashed blue: $A = 0.05$, dotted orange: $A = 0.5$, dash-dotted green: $A = 0.8$.

2. D^{10} is antisymmetric. Above the centerline, it is negative, indicating that mixing in those locations depends more on gradients towards the centerline (rather than towards the edge of the mixing layer), which is a negative distance away. Similar logic explains the positive behavior below the centerline.
3. D^{01} is symmetric always negative to satisfy causality.
4. D^{11} is antisymmetric.
5. D^{02} and D^{20} are symmetric and always positive, which is characteristic of the moment of inertia of a positive kernel.

We also observe that the moments become asymmetric at higher Atwood numbers. This is expected for A $\mathcal{O}(0.1)$ and above, since at these higher density differences, the heavy fluid falls faster than the light fluid rises, moving the mixing layer center line downward. The asymmetry of RT instability with finite Atwood numbers is well known, and it has also been found that quantities in turbulence budgets (e.g., mass flux and turbulent kinetic energy) are skewed in these regimes [20]. Thus, peak magnitudes for symmetric moments move further below the domain center line as Atwood increases. Similarly, the magnitudes of antisymmetric moments below the centerline become larger than the magnitudes above the centerline.

We can perform a preliminary assessment of nonlocality by examining the relative magnitudes of the measured moments, which is shown in Figure 10. Maximum relative magnitude values are also provided in Table 3. We first observe that for all Atwood numbers, the magnitudes of the higher order moments are not far off from the leading order moment. This was also on observation noted by Lavacot et al. [1] for 2D RT instability at $A = 0.05$. More notable is the increase in relative magnitude of the higher-order moments as Atwood increases. That is, the higher-order moments become closer in magnitude to the leading-order moment with higher Atwood numbers. This suggests that nonlocality becomes more important with increasing Atwood number—this will be examined more closely later sections.

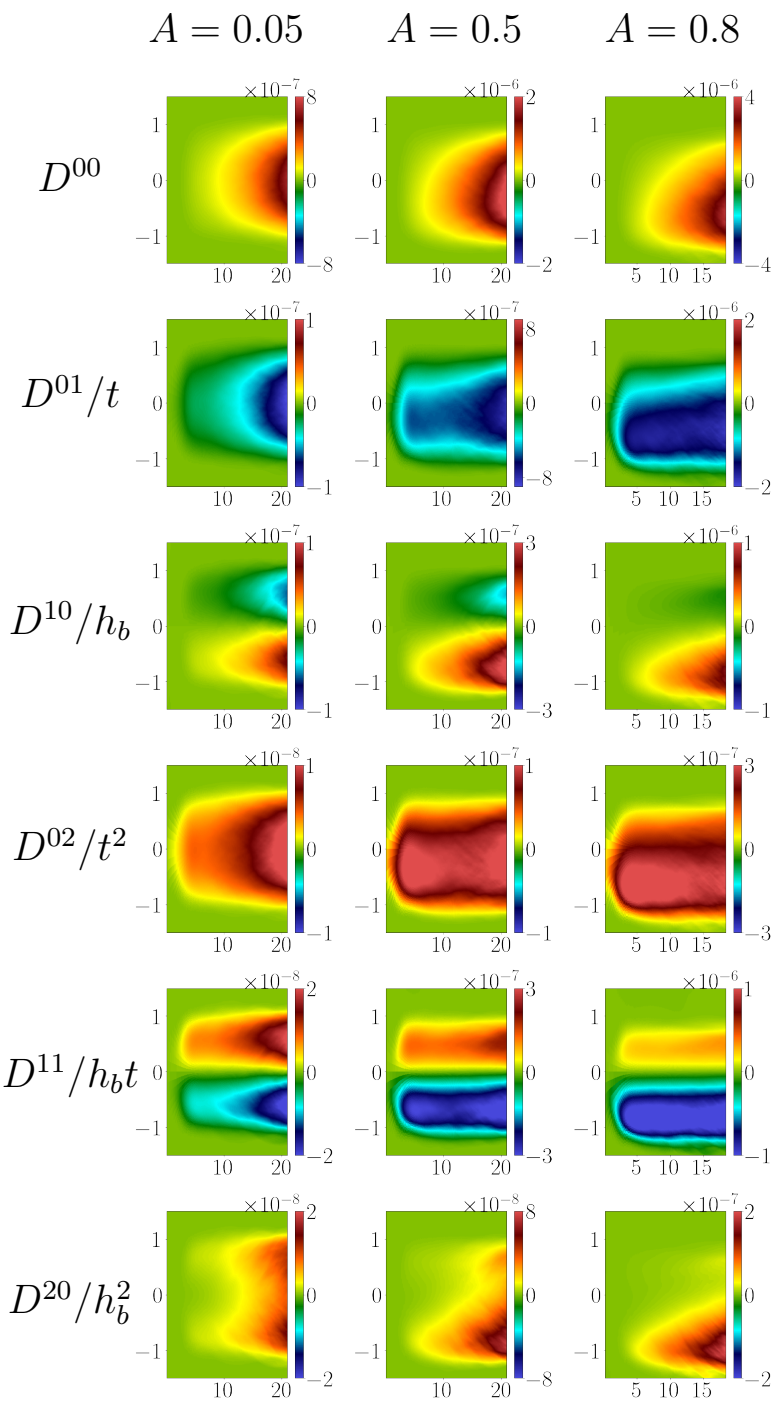

Figure 9: Eddy diffusivity moments of RT instability at different Atwood numbers. Moments are normalized by appropriate length and timescales so that all dimensions match.

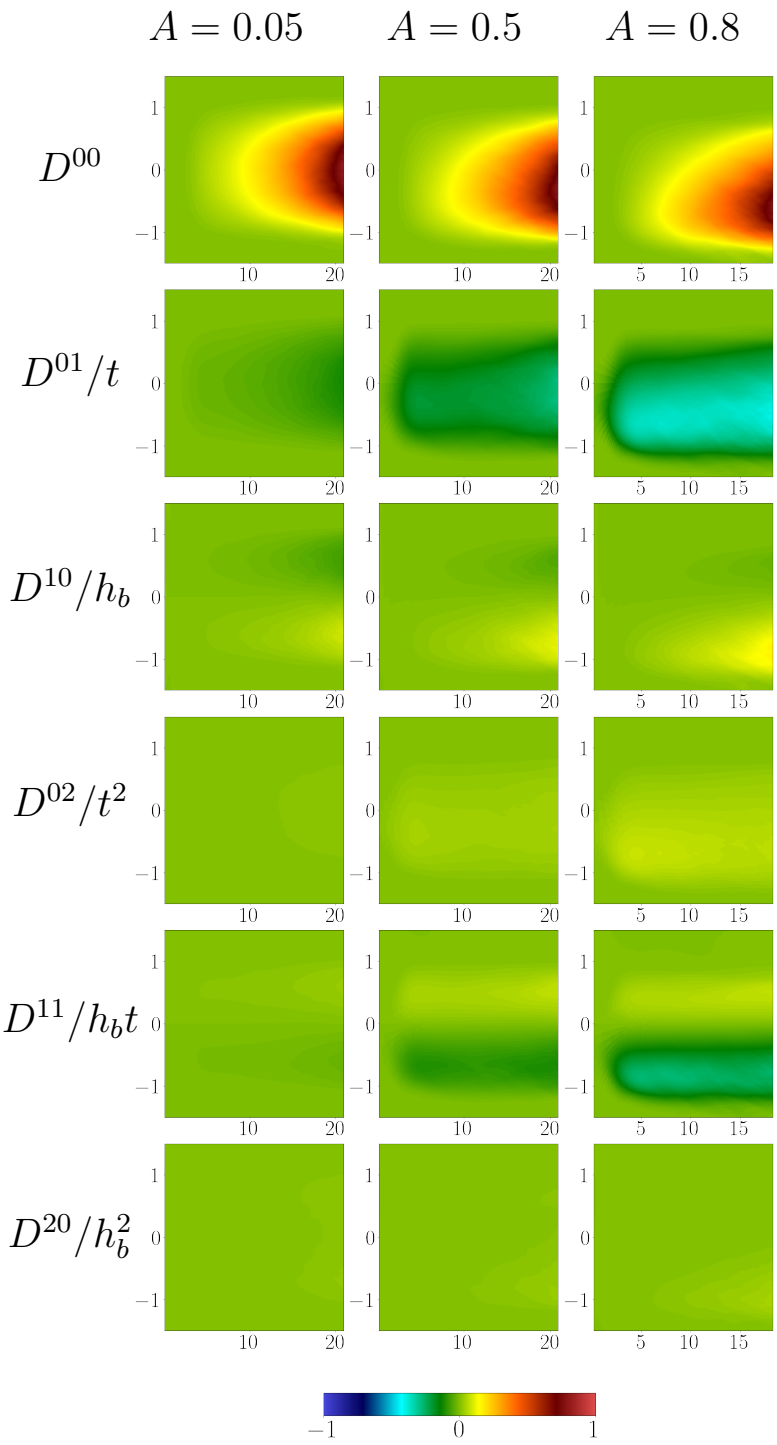

Figure 10: Eddy diffusivity moments normalized with respect to leading order moment at each Atwood number.

Ratio	$A = 0.05$	$A = 0.5$	$A = 0.8$
D^{10}/D^{00}	0.15	0.34	0.44
D^{01}/D^{00}	0.12	0.14	0.22
D^{20}/D^{00}	0.02	0.05	0.08
D^{11}/D^{00}	0.03	0.12	0.27
D^{02}/D^{00}	0.02	0.03	0.06

Table 3: Ratios of maximum magnitudes of higher-order moments to leading-order moments for each A case.

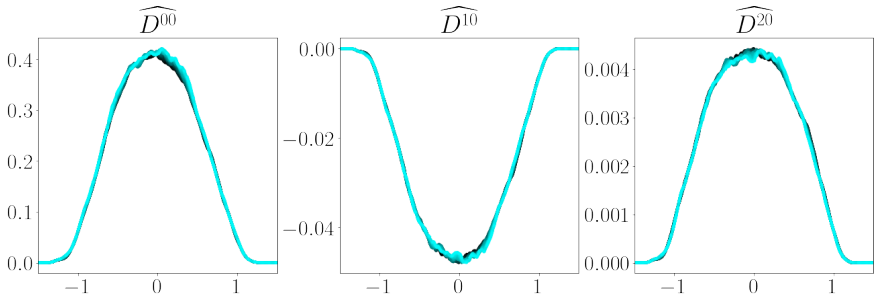

(a) $A = 0.05$

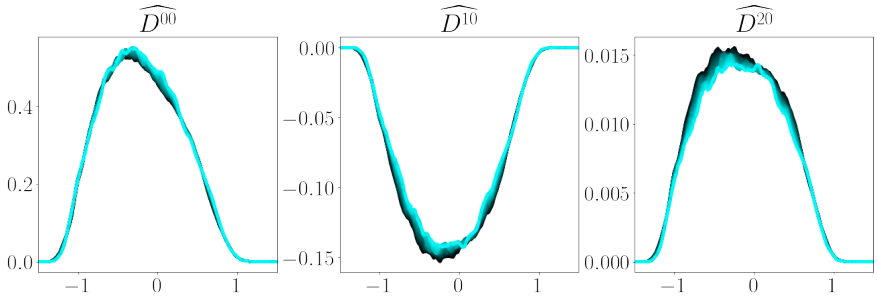

(b) $A = 0.5$

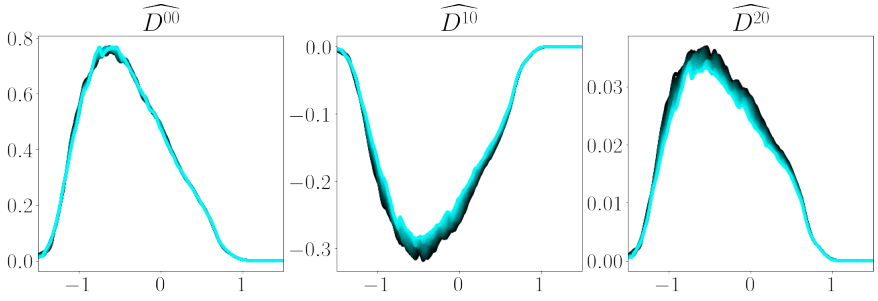

(c) $A = 0.8$

Figure 11: Self-similar collapse of leading-order and higher-order spatial eddy diffusivity moments of RT instability at different Atwood numbers.

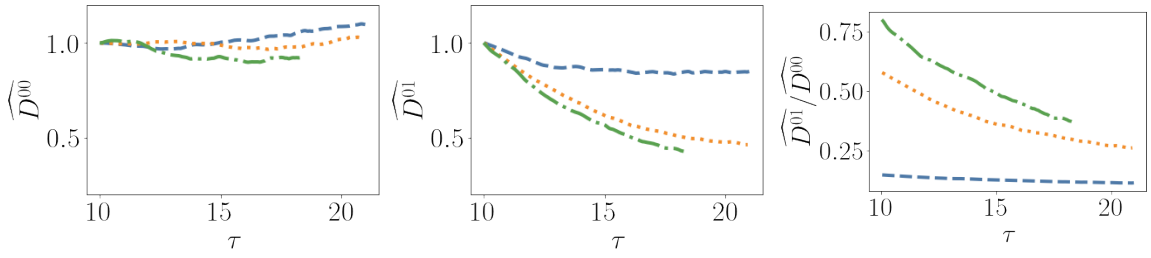

Figure 12: Maximum magnitudes of normalized eddy diffusivity moments over time. Plotting starts after the time the critical Re_T and Re_L for turbulence are reached. In (a) and (b), data are also normalized by the values at the beginning of plotting for each Atwood case so that the initial values on the plots are all unity.

Here, we also examine the self-similarity of the eddy diffusivity moments. Figure 11 shows the spatial eddy diffusivity moments at each Atwood number normalized according to self-similarity as in the Equations 38-43; the self-similar collapse of all moments are in the Appendix in Figures A.18-A.20. Qualitatively, we observe that the higher-order moments do not collapse as well as lower-order moments. Additionally, the self-similar collapse worsens with increasing Atwood number.

We can further evaluate the self-similarity of the moments by examining the maximum magnitudes of the normalized eddy diffusivity moments. Figure 12 shows $\widehat{D^{00}}$ and $\widehat{D^{01}}$ over the time period after the critical Reynolds numbers for turbulence are reached in each Atwood case. If these criteria are sufficient for self-similarity of the eddy diffusivity moments, we would expect that the plots of the normalized moments be constant with time. This appears to be the case for the lowest Atwood number simulation ($A = 0.05$). The higher Atwood number simulations ($A = 0.5$ and $A = 0.8$), however, give $\widehat{D^{00}}$ and $\widehat{D^{01}}$ that still vary in time.

Altogether, these observations suggest that the higher order the eddy diffusivity moment, the longer it takes to converge to a self-similar state. Particularly, higher-order moments take longer to reach self-similarity than lower-order quantities like the mixing width and the turbulent species flux. Thus, even if the flow in the MFM donor simulation fulfills criteria for self-similarity, such as reaching the critical Reynolds numbers or achieving a convergent α, the eddy diffusivity moments, especially the higher-order moments, may not necessarily be self-similar. When performing analysis on eddy diffusivity moments, one must be careful then to not only check the traditional self-similarity metrics of RT but also the self-similarity of the moments themselves.

3.2. Nonlocal length and time scales

Measurement of the eddy diffusivity moments using MFM allows for the quantification of nonlocal length and time scales. These are defined nondimensionally as

$$\eta_{NL} = \frac{1}{h_b}\sqrt{\frac{D^{20}}{D^{00}}}, \quad \tau_{NL} = -\frac{1}{\tau_0}\frac{D^{01}}{D^{00}}. \tag{62}$$

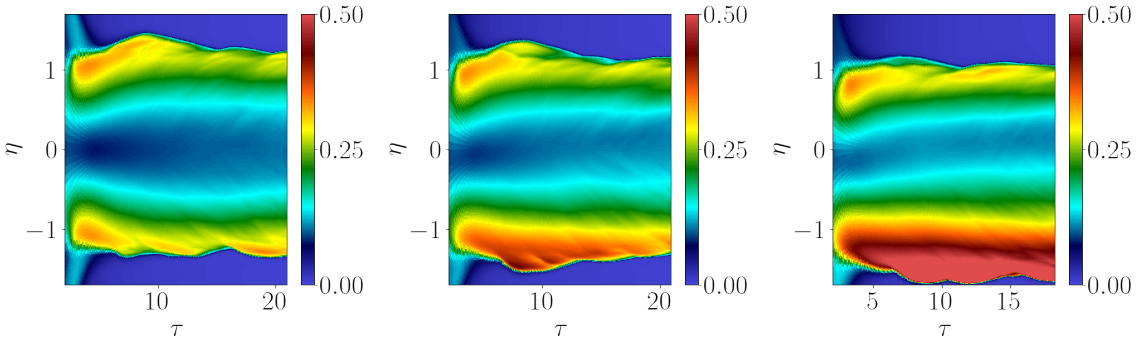

(a) $A = 0.05$ **(b)** $A = 0.5$ **(c)** $A = 0.8$

Figure 13: Contours of nonlocal length scales for each A case.

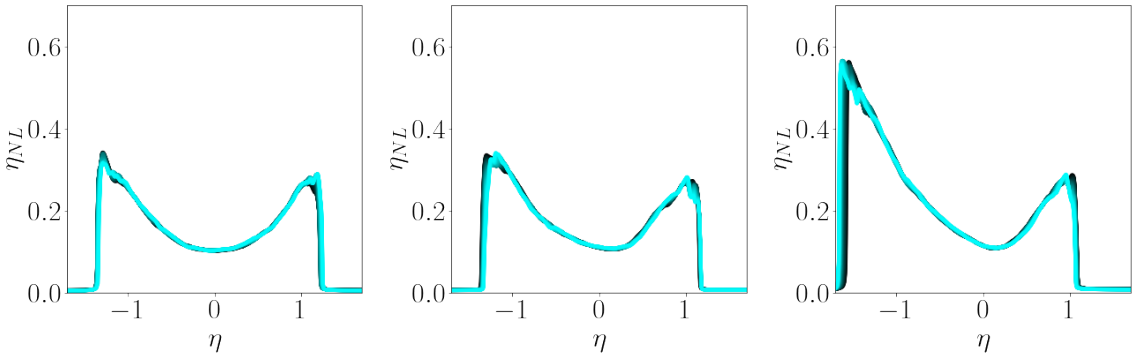

(a) $A = 0.05$ **(b)** $A = 0.5$ **(c)** $A = 0.8$

Figure 14: Profiles of nonlocal length scales for each A case. Darker lines are earlier times; lighter lines are later times.

Figure 13 shows the nonlocal length scale contours for each of the A cases. Qualitatively, they look similar across A, with minimum values at the centerline and maximum values at the edges of the mixing layer. Unsurprisingly, there is increased asymmetry at higher A, with mixing layer edge values below the centerline greater than those above the centerline. In the self-similar regime, profiles of the nonlocal length scales in Figure 14 show maximum values of approximately $\eta_{NL} = 0.35$, $\eta_{NL} = 0.35$, and $\eta_{NL} = 0.57$ for $A = 0.05$, $A = 0.5$, and $A = 0.8$, respectively. The minimum η_{NL} for all A is around 0.1. Based on these observations, we can make some general statements about spatial nonlocality for late-time RT for these A:

- The turbulent species flux at a location near the mixing layer edge depends on gradients further away from that location than does the flux at the centerline.
- For η at the mixing layer edges, the turbulent species flux depends on gradients approximately $0.3 - 0.6$ mixing half-widths away, and this value increases with A.
- For η at the centerline, the turbulent species flux depends on gradients approximately 0.1 mixing half-widths away, and this appears to be A-independent.

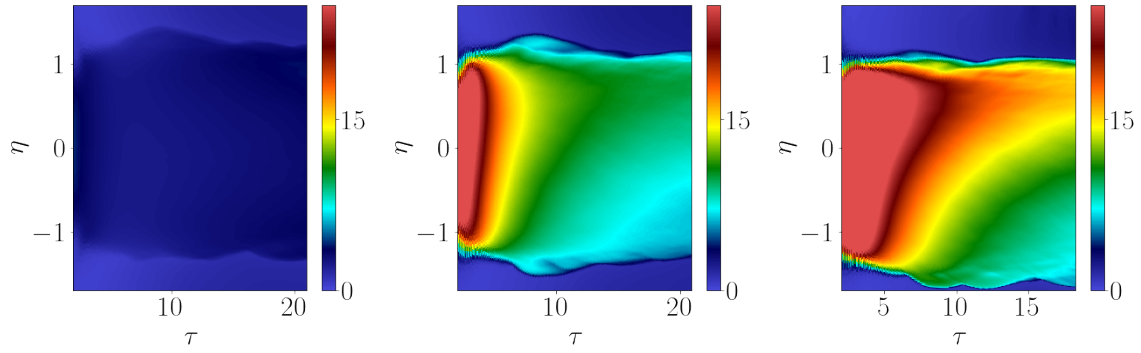

(a) $A = 0.05$ **(b)** $A = 0.5$ **(c)** $A = 0.8$

Figure 15: Contours of nonlocal time scales for each A case.

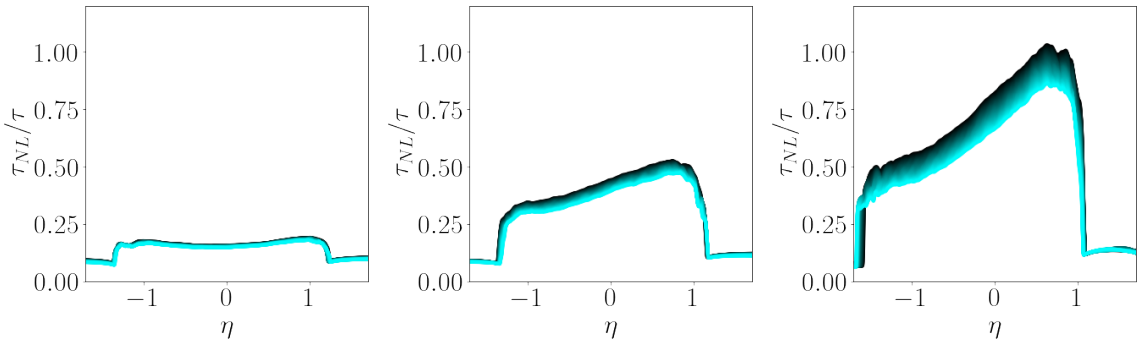

(a) $A = 0.05$ **(b)** $A = 0.5$ **(c)** $A = 0.8$

Figure 16: Profiles of nonlocal time scales scaled by τ for each A case. Darker lines are earlier times; lighter lines are later times.

We also examine the nonlocal time scale in Figure 15. In contrast to the nonlocal length scale, the nonlocal time scale differs greatly over the A studied here. Particularly, the max values of τ_{NL} increase with A, indicating that turbulent species fluxes depend more on earlier times for higher A. Additionally, the contours for τ_{NL} become more asymmetric with increasing A—max τ_{NL} shifts towards the edge of the mixing layer above the centerline as A increases. In the self-similar regime, it is expected that τ_{NL} scales as τ, so τ_{NL}/τ is plotted for each A case in Figure 16. We note that the quality of the collapse worsens as A increases, indicating that our highest A cases may not be far into the self-similar regime. Nevertheless, the profiles there show maximum values of approximately $\tau_{NL} = 0.25\tau$, $\tau_{NL} = 0.5\tau$, and $\tau_{NL} = 1.0\tau$ for $A = 0.05$, $A = 0.5$, and $A = 0.8$, respectively. Based on these observations, we can make some general statements about temporal nonlocality for late-time RT for these A:

- As A increases, across the mixing layer, the turbulent species flux depends more on the flux at earlier times.
- At low A, the dependence of the turbulent species flux on earlier times is relatively uniform across the mixing layer.

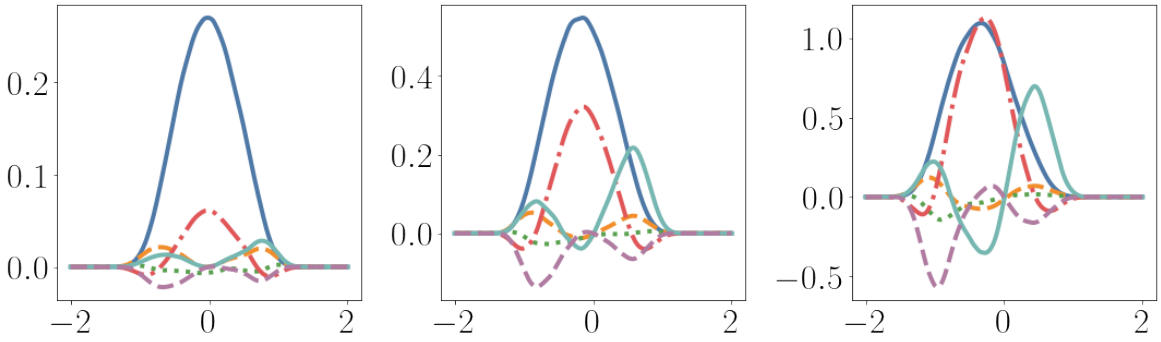

(a) $A = 0.05$ **(b)** $A = 0.5$ **(c)** $A = 0.8$

Figure 17: Terms of the Kramers-Moyal expansion for turbulent species flux at different Atwood numbers. Each line corresponds to terms with contributions from: D^{00} (solid blue), D^{10} (dashed orange), D^{01} (dash-dotted red), D^{20} (dotted green), D^{11} (solid teal), and D^{02} (dashed lilac).

- As A increases, the turbulent species flux near the upper edge of the mixing layer depends on earlier times than does the flux at the lower edge.

The MFM measurements also reveal large τ_{NL} at early times across A. These high τ_{NL} zones appear to be higher in magnitude and last longer as A increases. This suggests that as A increases, the RT instability retains memory of the initial conditions for a longer period of time.

3.3. Kramers-Moyal terms

To further assess the importance of nonlocality, we can examine the terms in the Kramers-Moyal expansion for the turbulent species flux, as shown in Figure 17. These terms are calculated a priori: the donor simulation $\widetilde{Y_H}$ is used for the mean mass fraction gradients, and the measured eddy diffusivity moments are substituted directly. Already at the lowest Atwood case of $A = 0.05$, we observe that the higher-order terms appear non-negligible compared to the leading-order term; at least some of the higher-order terms will need to be retained for complete characterization of the eddy diffusivity. This was also shown in the 2D case at the same Atwood number studied in Lavacot et al. [1].. We further observe that as Atwood number increases, the higher-order terms become closer in magnitude to the leading-order term, indicating that nonlocality becomes more important with increasing Atwood. This also suggests that at higher Atwood numbers, more higher-order moments may be required for modeling that at lower Atwood numbers. It is notable that the temporal moments are particularly large at high Atwood numbers, indicating that temporal nonlocality may be especially important in those regimes.

4. Conclusion

In this work, MFM is used to measure the eddy diffusivity moments associated with mean scalar transport in turbulent RT mixing for different Atwood numbers. Similarly to a past work studying 2D, low-Atwood RT [1], we find here that nonlocality is important for modeling 3D RT mixing.

Through MFM measurements at multiple Atwood numbers ($A = 0.05$, $A = 0.5$, and $A = 0.8$), we observe that the importance of nonlocality increases as A increases. Temporal nonlocality appears to be the most important, which we observe through examination of the Kramers-Moyal terms and nonlocal timescale. That is, as A increases, the importance of history effects increases, suggesting that RT mixing at higher A has a longer "memory" than lower A cases.

We also find that the higher-order eddy diffusivity moments take longer to reach self-similarity than lower-order moments, and this effect is greater with increasing A. This means that even if certain metrics for self-similarity (e.g., convergence of α or ϕ) are met, higher-order eddy diffusivity moments may not yet be self-similar. Thus, it is important to carefully examine the self-similarity of the higher-order moments themselves when making conclusions about the self-similarity of the turbulent mixing.

Overall, this work gives a first look into the Atwood dependence of nonlocality by examining three Atwood numbers. To get a better understanding of the Atwood dependence, future work should perform these analyses at more Atwood numbers. Particularly, it would be helpful to study intermediate A between 0.05 and 0.5 to identify trends or transitions in behavior from low to high Atwood numbers. This would give better insight into the Atwood dependence of nonlocality and potentially allow for quantification of this dependence.

While the goal of this work is to assess nonlocality at different A, future work should explore incorporation of the Atwood-dependence of nonlocality into turbulence models. This would involve identifying precisely which higher-order moments are needed for convergence of a model for higher Atwood numbers. It has been found that at low A, only D^{00}, D^{01}, and D^{10} are needed for accurate predictions, but the observation here that nonlocality increases with A suggests that more moments may be needed for higher A, particularly temporal moments. To make this assessment, high Atwood simulations that go further into the self-similar regime than those presented here are needed for analysis.

Acknowledgements. This work was performed under the auspices of the US Department of Energy by Lawrence Livermore National Laboratory under Contract No. DE-AC52-07NA27344.

Appendix A. Self-similar collapse of eddy diffusivity moments

Figures A.18 - A.20 show the self-similar collapse of the eddy diffusivity moments. Normalization is applied according to Equations 38 - 43.

References

[1] D.-L. Lavacot, J. Liu, H. Williams, B. E. Morgan, A. Mani, Non-locality of mean scalar transport in two-dimensional rayleigh–taylor instability using the macroscopic forcing method, Journal of Fluid Mechanics **985** (2024) A47.

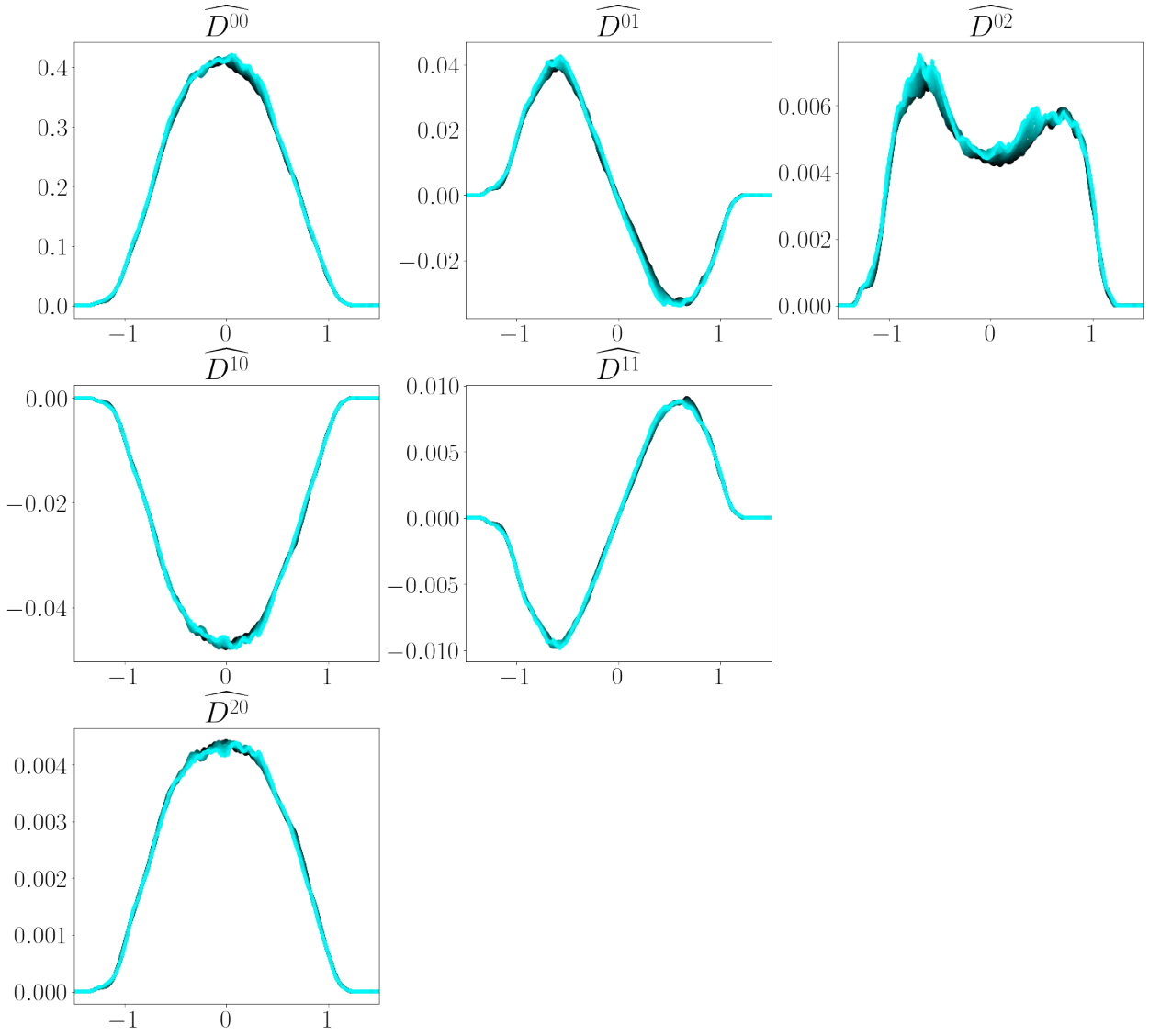

Figure A.18: Self-similar collapse of eddy diffusivity moments at $A = 0.05$. Dark lines are earlier times, and light lines are later times.

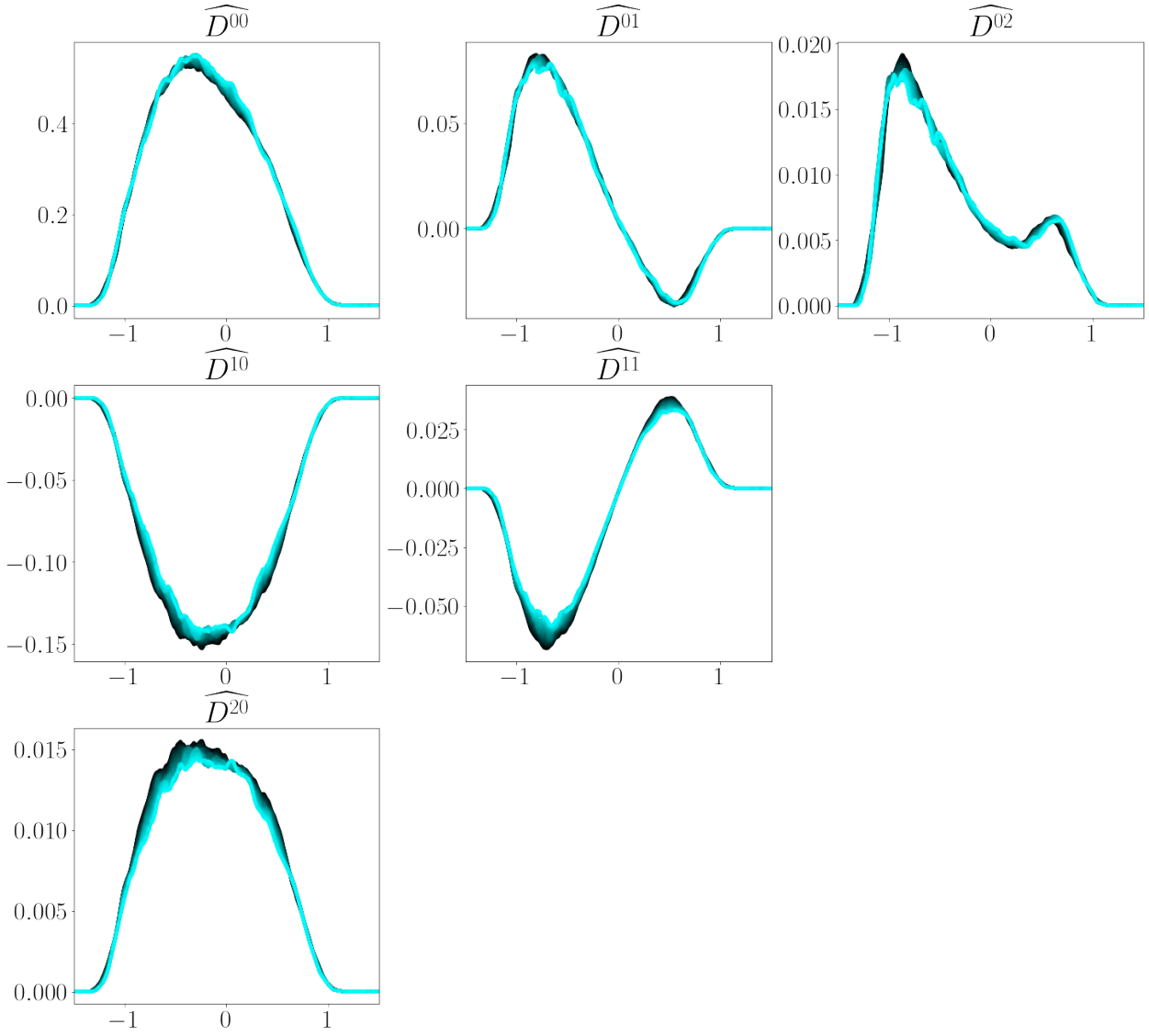

Figure A.19: Self-similar collapse of eddy diffusivity moments at $A = 0.5$. Dark lines are earlier times, and light lines are later times.

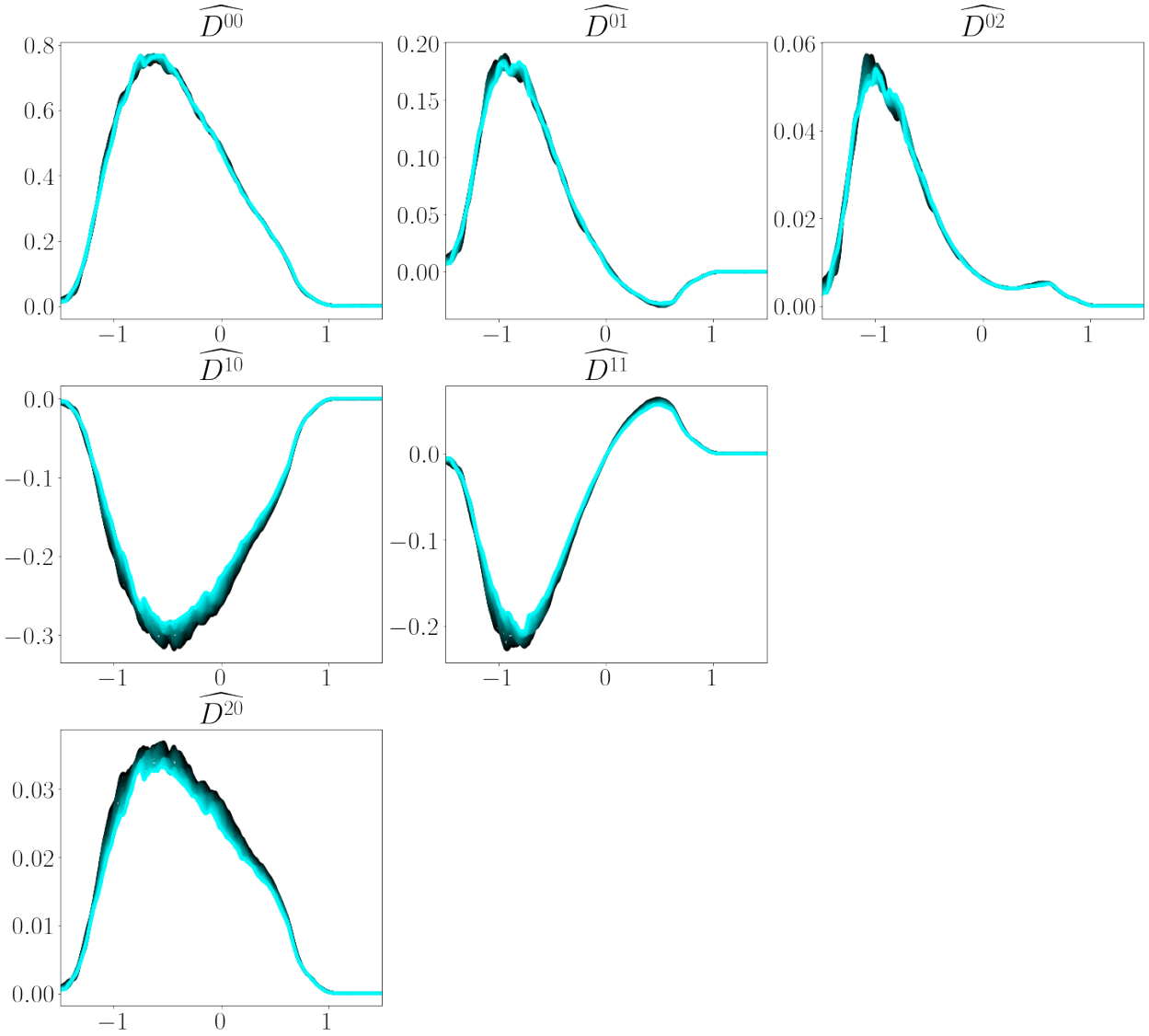

Figure A.20: Self-similar collapse of eddy diffusivity moments at $A = 0.8$. Dark lines are earlier times, and light lines are later times.

[2] A. Pak, L. Divol, C. Weber, L. B. Hopkins, D. Clark, E. Dewald, D. Fittinghoff, V. Geppert-Kleinrath, M. Hohenberger, S. Le Pape, et al., Impact of localized radiative loss on inertial confinement fusion implosions, Physical review letters **124** (2020) 145001.

[3] D. L. Youngs, Numerical simulation of mixing by Rayleigh-Taylor and Richtmyer–Meshkov instabilities, Laser and Particle Beams **12** (1994) 725–750.

[4] W. H. Cabot, A. W. Cook, Reynolds number effects on Rayleigh-Taylor instability with possible implications for type Ia supernovae, Nature Physics **2** (2006) 562–568.

[5] N. J. Mueschke, O. Schilling, Investigation of Rayleigh-Taylor turbulence and mixing using direct numerical simulation with experimentally measured initial conditions. I. Comparison to experimental data, Physics of Fluids **21** (2009) 014106.

[6] B. E. Launder, D. B. Spalding, The numerical computation of turbulent flows, Computer Methods in Applied Mechanics and Engineering **3** (1974) 269–289.

[7] S. Gauthier, M. Bonnet, A k-ε model for turbulent mixing in shock-tube flows induced by Rayleigh-Taylor instability, Physics of Fluids A: Fluid Dynamics **2** (1990) 1685–1694.

[8] G. Dimonte, R. Tipton, K-L turbulence model for the self-similar growth of the Rayleigh-Taylor and Richtmyer-Meshkov instabilities, Physics of Fluids **18** (2006) 085101.

[9] B. E. Morgan, B. J. Olson, J. E. White, J. A. McFarland, Self-similarity of a Rayleigh-Taylor mixing layer at low Atwood number with a multimode initial perturbation, Journal of Turbulence **18** (2017) 973–999.

[10] N. A. Denissen, B. Rollin, J. M. Reisner, M. J. Andrews, The Tilted Rocket Rig: A Rayleigh-Taylor Test Case for RANS Models, Journal of Fluids Engineering **136** (2014). 091301.

[11] N. O. Braun, R. A. Gore, A multispecies turbulence model for the mixing and de-mixing of miscible fluids, Journal of Turbulence **22** (2021) 784–813.

[12] T. T. Clark, P. B. Spitz, Two-point correlation equations for variable density turbulence, Technical Report, Los Alamos National Lab.(LANL), Los Alamos, NM (United States), 1995.

[13] M. J. Steinkamp, T. T. Clark, F. H. Harlow, Two-point description of two-fluid turbulent mixing—I. Model formulation, International Journal of Multiphase Flow **25** (1999) 599–637.

[14] N. Pal, S. Kurien, T. T. Clark, D. Aslangil, D. Livescu, Two-point spectral model for variable-density homogeneous turbulence, Phys. Rev. Fluids **3** (2018) 124608.

[15] T. T. Clark, F. H. Harlow, R. W. Moses, Comparison of a spectral turbulence model with experimental data of Rayleigh-Taylor mixing, Technical Report, Los Alamos National Lab.(LANL), Los Alamos, NM (United States), 1997.

[16] J. R. Ristorcelli, T. T. Clark, Rayleigh-Taylor turbulence: self-similar analysis and direct numerical simulations, Journal of Fluid Mechanics **507** (2004) 213–253.

[17] N. J. Mueschke, M. J. Andrews, O. Schilling, Experimental characterization of initial conditions and spatio-temporal evolution of a small-Atwood-number Rayleigh-Taylor mixing layer, Journal of Fluid Mechanics **567** (2006) 27–63.

[18] A. Mani, D. Park, Macroscopic forcing method: A tool for turbulence modeling and analysis of closures, Phys. Rev. Fluids **6** (2021) 054607.

[19] F. Hamba, Nonlocal analysis of the Reynolds stress in turbulent shear flow, Physics of Fluids **17** (2005).

[20] D. Livescu, J. Ristorcelli, M. R. Petersen, R. A. Gore, New phenomena in variable-density rayleigh–taylor turbulence, Physica Scripta **2010** (2010) 014015.

[21] D. L. Youngs, The density ratio dependence of self-similar rayleigh–taylor mixing, Philosophical Transactions of the Royal Society A: Mathematical, Physical and Engineering Sciences **371** (2013) 20120173.

[22] Y. Zhou, Rayleigh–taylor and richtmyer–meshkov instability induced flow, turbulence, and mixing. ii, Physics Reports **723** (2017) 1–160.

[23] P. E. Dimotakis, The mixing transition in turbulent flows, Journal of Fluid Mechanics **409** (2000) 69–98.

[24] R. H. Kraichnan, Eddy viscosity and diffusivity: exact formulas and approximations, Complex Systems **1** (1987) 805–820.

[25] F. Hamba, An analysis of nonlocal scalar transport in the convective boundary layer using the Green's function, Journal of Atmospheric Sciences **52** (1995) 1084–1095.

[26] D. Park, A. Mani, Direct calculation of the eddy viscosity operator in turbulent channel flow at reτ= 180, Journal of Fluid Mechanics **998** (2024) A33.

[27] J. Liu, H. Williams, A. Mani, Systematic approach for modeling a nonlocal eddy diffusivity, Physical Review Fluids **8** (2023) 124501.

[28] M. Schulz, A. W. Cook, W. H. Cabot, B. R. de Supinski, W. D. Krauss, On the performance of the Miranda CFD code on multicore architectures, Parallel Computational Fluid Dynamics: Recent Advances and Future Directions (2010) 132.

[29] T. J. Rehagen, J. A. Greenough, B. J. Olson, A validation study of the compressible rayleigh–taylor instability comparing the ares and miranda codes, Journal of Fluids Engineering **139** (2017) 061204.

[30] A. W. Cook, Artificial fluid properties for large-eddy simulation of compressible turbulent mixing, Physics of fluids **19** (2007).

[31] B. E. Morgan, W. J. Black, Parametric investigation of the transition to turbulence in Rayleigh-Taylor mixing, Physica D: Nonlinear Phenomena **402** (2020) 132223.